

Electronic Thesis and Dissertation Repository

5-29-2017 12:00 AM

Study on the mechanical behavior of directly compounded long glass fiber reinforced polyamide 6 composites

Yuchao Liu, *The University of Western Ontario*

Supervisor: Jeffrey T. Wood, *The University of Western Ontario*

A thesis submitted in partial fulfillment of the requirements for the Master of Engineering Science degree in Mechanical and Materials Engineering

© Yuchao Liu 2017

Follow this and additional works at: <https://ir.lib.uwo.ca/etd>



Part of the [Mechanics of Materials Commons](#)

Recommended Citation

Liu, Yuchao, "Study on the mechanical behavior of directly compounded long glass fiber reinforced polyamide 6 composites" (2017). *Electronic Thesis and Dissertation Repository*. 4576.
<https://ir.lib.uwo.ca/etd/4576>

This Dissertation/Thesis is brought to you for free and open access by Scholarship@Western. It has been accepted for inclusion in Electronic Thesis and Dissertation Repository by an authorized administrator of Scholarship@Western. For more information, please contact wlsadmin@uwo.ca.

Abstract

With great lightweight potential, high performance-to-cost ratio and mass productivity, direct-compounded long fiber thermoplastics (D-LFT) have drawn great attention from the automotive industry. With better mechanical properties and higher service temperature, polyamide 6 (PA6) was used to replace polypropylene (PP) which is almost the exclusively used matrix for the D-LFT process currently. The investigation was performed on this new material with a focus on the effect of fiber content, processing parameters, temperature and tailored reinforcement on mechanical behavior. The results show that the mechanical properties of this new material are sensitive to the variation of fiber content and service temperature but insensitive to the varied processing parameters. Tailored reinforcement technique is a feasible and predictable approach to adjust the mechanical properties of this new material.

Keywords

D-LFT, glass fiber, thermoplastic, polyamide 6, mechanical property, fiber content, processing parameter, temperature, tailored reinforcement

Acknowledgments

Firstly, I would like to thank Dr. Jeff Wood for giving me the opportunity to enter this amazing composite world. During the past two years, it was your gentle guidance and positive encouragement that helped me to step forward. I had not anticipated to be able to take so many valuable scientific events such as the internship in Fraunhofer Project Center of Composite Research (FPC@Western) in my first term, the summer school in Germany and ACCE conference in the US. I was so lucky to have someone like you as my supervisor.

I also would like to say thanks to Dr. Ying Fan. I appreciate that you put me on your back to adapt to this new environment. Thank you for providing me the suggestions almost in every aspect of my life here. To be honest, as sometimes being a little frivolous on my research work, I appreciate that you can always bring me back on the right way. I just feel lucky here to have someone like you who supervises me so carefully.

Then I would like to thank all the staffs from the FPC@Western, including Vanja Ugresic, Marcel Holzner, Louis Kaptur and Rob Cosh for your kind help with the preparation of this project as well as my internship there. Thank all the industrial partners including General Motors, BASF, Johns Manville, Dieffenbacher, Elringklinger, NSERC for offering the valuable financial and technical supports.

Additionally, I would like to say thanks to my previous supervisors, Hongwei Li and Dunbo Yu. Without your kind support, I might not be able to come to Canada to pursue my goals.

At last, I want to say thanks to my families. You are all the reasons I step forward. Thank my wife, Fei, for giving me all her love and making me be the luckiest man in the world. Thank my parents for understanding and supporting me to extend my career in Canada. I would try my best to give you a better life in the future.

Table of Contents

Abstract.....	iii
Acknowledgments.....	iv
Table of Contents	v
List of Tables	viii
List of Figures.....	ix
Chapter 1.....	1
1 Introduction.....	1
1.1 Motivation.....	1
1.2 Task description	2
Chapter 2.....	4
2 Literature review	4
2.1 Fiber reinforced plastics.....	4
2.1.1 Matrix materials	4
2.1.2 Fiber products	8
2.2 Long fiber reinforced thermoplastics.....	13
2.2.1 Processing techniques for long fiber reinforced thermoplastics	13
2.2.2 Influence of fiber content on the mechanical properties of LFT composites.....	16
2.2.3 Influence of processing parameters on the mechanical properties of LFT composites	18
2.2.4 Environmental effect on the mechanical properties of LFT composites ..	22
2.2.5 UD tape reinforcement on D-LFT composite.....	24
2.3 Prediction of mechanical properties of long fiber thermoplastic.....	26
2.4 Summary.....	30

Chapter 3.....	31
3 Experimental	31
3.1 Materials	31
3.2 Preparation	31
3.2.1 Dieffenbacher D-LFT-ILC line.....	31
3.2.2 D-LFTs with different fiber contents	33
3.2.3 D-LFTs with different processing parameters	39
3.2.4 Reinforcing D-LFT with UD tapes	40
3.3 Methodology	43
3.3.1 Mechanical testing	43
3.3.2 Characterization of microstructure	48
3.3.3 Measurement of fiber volume fraction	49
3.3.4 Measurement of fiber length distribution	49
3.3.5 Measurement of fiber orientation distribution	49
Chapter 4.....	52
4 Result and discussion	52
4.1 Mechanical behavior of D-LFTs with different fiber contents.....	52
4.1.1 Spatial variations of thickness and fiber content within individual plaque.....	52
4.1.2 Mechanical testing results.....	54
4.1.3 Prediction of Young’s modulus of D-LFT.....	61
4.1.4 Effect of fiber content on fiber length distribution and fiber orientation distribution	66
4.2 Effect of the processing parameters on the mechanical properties of glass fiber/PA6 D-LFTs.....	68
4.2.1 Tested mechanical properties.....	68

4.2.2	Variation of fiber length.....	70
4.2.3	Variation of fiber content.....	72
4.3	Mechanical behavior of glass fiber/PA6 D-LFT at different temperatures	74
4.3.1	Tested mechanical properties.....	74
4.3.2	Analysis of failure mode.....	77
4.4	Characterization of the mechanical behavior of UD tape reinforced D-LFT with different stacking sequence.....	80
4.4.1	Tested mechanical properties.....	82
4.4.2	Prediction of in-plane elastic properties	88
4.4.3	Microstructure.....	91
Chapter 5	94
5	Conclusion	94
5.1	Summary.....	94
5.2	Future work.....	95
6	References	96
	Curriculum Vitae	106

List of Tables

Table 2-1 Properties of some commonly used resins. [1].....	5
Table 2-2 Repeating units of different polyamides.....	7
Table 3-1 Properties of PA6 (Ultramid 8802HS) and glass fiber (JM 886) used in this work.	32
Table 3-2 List of the processing parameters in 8 conditions, room temperature (R.T.) is 23°C.	40

List of Figures

Figure 2-1 Schematic molecular structure of a) semi-crystalline thermoplastics (highlighted in red) and b) amorphous thermoplastics	6
Figure 2-2 Repeating unit of polypropylene.....	7
Figure 2-3 The molecular structure of glass fiber.....	9
Figure 2-4 The layered structure of carbon fiber. [8]	9
Figure 2-5 Shear lag model showing: a) unstressed system, b) axial displacements u introduced on applying tension parallel to the fiber and c) variation with radial location of the shear stress τ and strain in the matrix. [1]	10
Figure 2-6 Distribution of a) tensile stress in the fiber and b) interfacial shear stress along the interface for different fiber length. [1]	12
Figure 2-7 Relationship between fiber length and different mechanical properties (stiffness, strength and toughness) of PP based composites. [11]	12
Figure 2-8 Schematic of the GMT processing technique.	14
Figure 2-9 Schematic of the LFT-G processing technique.....	14
Figure 2-10 Parameters involved in screw design: barrel diameter D_b , centerline distance A , clearance screw-barrel C_b , clearance screw- screw C_s and flight pitch P	20
Figure 2-11 Four types of twin-screw designs with different placements of high mixing elements resulting in different shear flow. [44]	20
Figure 2-12 Local cracks caused by moisture absorbed in composites. [60]	23
Figure 2-13 Comparison between the FRPs based on different fiber products. [100]	25
Figure 2-14 Voigt (iso-strain) model and Reuss (iso-stress) model for composite material elasticity.	28

Figure 3-1 Schematic of Dieffenbacher D-LFT-ILC line.....	32
Figure 3-2 a) Polymer dryer and b) gravimetric dosing unit of Dieffenbacher D-LFT-ILC line.....	35
Figure 3-3 The first extruder (ZSE) of Dieffenbacher D-LFT-ILC line.....	35
Figure 3-4 Fiber feeding system of Dieffenbacher D-LFT-ILC line with a) continuous glass fiber tows b) plastic tube system c) iron bars for fiber preheating d) roving separation apparatus above the second extruder.....	36
Figure 3-5 The second extruder (ZSG) of Dieffenbacher D-LFT-ILC line.....	37
Figure 3-6 Schematic of the second extruder (ZSG) of Dieffenbacher D-LFT-ILC line.	37
Figure 3-7 Conveyor (PAZ) of Dieffenbacher D-LFT-ILC line with a) composites charge and b) the conveyor.....	38
Figure 3-8 Dieffenbacher DCP-U 2500/2200 hydraulic press and b) the compression mold used in this work.....	38
Figure 3-9 Size and charge position of the plaques prepared in this work.	39
Figure 3-10 Unidirectional continuous fiber tape with 60 wt.% fiber provided by BASF.	41
Figure 3-11 Fiberforge Relay@ 1000 at FPC@Western.....	42
Figure 3-12 Layups with stacking sequence of $[0/90]_s$ a) before consolidation and b)after consolidation.	42
Figure 3-13 Detailed structure of the layups and co-molded products with three types of stacking sequence.....	43
Figure 3-14 Setup of the tensile test with a 50mm extensometer.	46
Figure 3-15 Instron 8804 load frame equipped with a VIC-3D™ System.....	46

Figure 3-16 3-point bending test apparatus.	47
Figure 3-17 A speckled shear specimens fixed in a Iosipescu shear fixture.....	47
Figure 3-18 Dynatup Instron 9250 HV drop tower.	48
Figure 3-19 MTS load frame equipped with an environmental chamber and a video extensometer.	50
Figure 3-20 a) Hitachi S-4500 field emission SEM and b) Nikon Eclipse L150 microscope.	50
Figure 3-21 GE eXplore SP "MS" micro-CT.	51
Figure 4-1 Fiber thickness distribution within a D-LFT plaque with 30 wt.% fiber.	53
Figure 4-2 Fiber content distribution within a D-LFT plaque with 30 wt.% fiber.	54
Figure 4-3 Tensile and flexural modulus in both flow and cross-flow directions of glass fiber/PA6 D-LFTs with different fiber contents.	55
Figure 4-4 Tensile and flexural strength in both flow and cross-flow directions of glass fiber/PA6 D-LFTs with different fiber contents.	55
Figure 4-5 Fracture surfaces of tensile specimens tested in 0° and 90°-directions of D-LFT with a) 30 wt.% fiber and b) 50 wt.% fiber.	57
Figure 4-6 SEM images of the fracture surfaces of tensile D-LFT sample with a) 20 wt.% fiber tested in 0°-direction and b) tensile D-LFT sample with 50 wt.% fiber tested in 0°-direction.	57
Figure 4-7 SEM image of the fracture surface of a tensile D-LFT specimen with 50 wt.% fiber tested in 90°-direction.	58
Figure 4-8 Tensile and flexural strain at failure in both flow and cross-flow directions of D-LFTs with different fiber contents.	59

Figure 4-9 Shear modulus and strength in both flow and cross-flow directions of glass fiber/PA6 D-LFTs with different fiber contents.	59
Figure 4-10 Poisson’s ratio in both flow and cross-flow directions of glass fiber/PA6 D-LFTs with different fiber contents.	59
Figure 4-11 Thickness specific impact peak force, impact energy and energy to peak force of D-LFTs with different fiber contents.	60
Figure 4-12 Failed impact D-LFT specimens with fiber contents of a) 30-60 wt.% and b) 20 wt.%.	61
Figure 4-13 a) Position and b) size of the sample cut for micro-CT scan.	62
Figure 4-14 Images of cross sections through the thickness of a D-LFT sample by micro-CT scan with resolution of 6 micrometers.	62
Figure 4-15 Fiber orientation distribution (FOD) measured on 9 layers of a D-LFT sample as shown in Figure 4-14.	64
Figure 4-16 Measured fiber length distribution (FLD) of D-LFT with 30 wt.% fiber.	65
Figure 4-17 Young’s moduli in 0° and 90°-directions of D-LFT with 30 wt.% fiber predicted by MROM and Halpin-Tsai models and determined by tensile tests.	65
Figure 4-18 Relationship between value of k_1k_2 and different fiber content which is measured with tested E_{11} , known material properties and fiber volume fraction through MROM model.	67
Figure 4-19 Fiber length factor k_1 calculated with different fiber length based on shear lag model.	67
Figure 4-20 Tensile modulus and strength in both 0°-direction and 90°-direction of glass fiber/PA6 D-LFTs specimens prepared in different processing parameters (T1: standard condition; T2&T3: lower and higher screw speed; T4&T5: higher and lower filling level; T6&T7: lower and higher melt temperature; T8: fiber preheating).	69

Figure 4-21 Flexural modulus and strength in both 0°-direction and 90°-direction of glass fiber/PA6 D-LFTs specimens prepared with different processing parameters (T1: standard condition; T2&T3: lower and higher screw speed; T4&T5: higher and lower filling level; T6&T7: lower and higher melt temperature; T8: fiber preheating).	70
Figure 4-22 Unnotched impact properties in both 0°-direction and 90°-direction of D-LFTs prepared in different processing parameters (T1: standard condition; T2&T3: lower and higher screw speed; T4&T5: higher and lower filling level; T6&T7: lower and higher melt temperature; T8: fiber preheating).	71
Figure 4-23 Length weighted and numerical average fiber length measured on T4 (the highest filling level) and T5 (the lowest filling level) plaques.	71
Figure 4-24 Fiber length factor k_1 calculated with different average fiber length based on shear lag model.	73
Figure 4-25 Fiber contents measured on D-LFTs prepared in different conditions (T1: standard condition; T2&T3: lower and higher screw speed; T4&T5: higher and lower filling level; T6&T7: lower and higher melt temperature; T8: fiber preheating).	73
Figure 4-26 Fiber content measured on both the 2 nd and the 9 th out of 10 D-LFT plaques for T1, T4 and T5.	74
Figure 4-27 Tensile and flexural stress-strain curves at -40°C, R.T., 85°C and 120°C for the D-LFTs with fiber contents of 20, 30 and 40 wt.%.	75
Figure 4-28 Tensile and flexural moduli tested at -40°C, R.T., 85°C and 120°C of D-LFTs with fiber contents of 20, 30 and 40 wt.%.	76
Figure 4-29 Tensile and flexural strengths tested at -40°C, R.T., 85°C and 120°C of D-LFTs with fiber contents of 20, 30 and 40 wt.%.	76
Figure 4-30 Tensile and flexural strain at failure tested at -40°C, R.T., 85°C and 120°C of D-LFTs with fiber contents of 20, 30 and 40 wt.%.	76

Figure 4-31 Failed tensile specimens tested at -40°C, R.T., 85°C and 120°C of D-LFTs with fiber contents of 20, 30 and 40 wt.%.	78
Figure 4-32 SEM images of fracture surfaces of tensile D-LFT specimens with 20 wt.% fiber tested at -40°C.	79
Figure 4-33 SEM images of fracture surfaces of tensile D-LFT specimens with 20 wt.% fiber tested at R.T.	79
Figure 4-34 SEM images of fracture surface of tensile D-LFT specimens with 20 wt.% fiber tested at 85°C.	79
Figure 4-35 SEM images of fracture surface of tensile D-LFT specimens with 20 wt.% fiber tested at 120°C.	81
Figure 4-36 SEM images of fracture surfaces of tensile D-LFT specimens with 20 wt.% fiber tested a: -40°C, b: R.T., c: 85°C and d: 120°C.	81
Figure 4-37 SEM images of fracture surface of tensile D-LFT specimens with 40 wt.% fiber tested at R.T.	82
Figure 4-38 Thickness specific impact energy and thickness specific peak load tested on pure D-LFT with 30 wt.% fiber, layups and comouldings with 3 types of stacking sequence ([0] _s , [0/90] _s and [0/90/+45/-45] _s).	83
Figure 4-39 Failed puncture specimens: a) D-LFT, b) #1L, c) #2L, d) #3L, e) #1C, f) #2C and g) #3C.	84
Figure 4-40 Tensile stress-strain curves in 0 and 90°-directions for a) D-LFT and layups with 3 stacking sequences and b) comoldings with 3 stacking sequences.	85
Figure 4-41 Tensile moduli and strengths in 0 and 90°-directions for a) D-LFT and layups with 3 stacking sequences and b) comoldings with 3 stacking sequences.	85

Figure 4-42 Failed tensile samples with stacking sequence of UD [0] ₈ : a) #1L tested in 0°-direction, b) #1L tested in 90°-direction, c) #1C tested in 0°-direction and d) #1C tested in 90°-direction.	86
Figure 4-43 Flexural stress-strain curves in both 0° and 90°-directions for a) D-LFT and layups with 3 types of stacking sequence and b) comoldings with 3 types of stacking sequence.	87
Figure 4-44 Flexural modulus and strength in 0°-direction and 90°-direction for pure D-LFT with 30 wt.% fiber, layups with 3 types of stacking sequence and comoldings with 3 types of stacking sequence.	87
Figure 4-45 Failed flexural specimens tested in 0°-direction of layups and comouldings with three types of stacking sequence: a) #1L tested in 90°-direction viewed from bottom and side, b) #2L tested in 90°-direction viewed from bottom and side, c) #3L tested in 90°-direction viewed from bottom and side, d) #1C tested in 0° and 90°-direction, e) #2C tested in 0° and 90°-direction and f) #3C tested in 0° and 90°-direction.	88
Figure 4-46 Shear modulus in both 0° and 90°-directions for pure D-LFT with 30 wt.% fiber, layups with 3 types of stacking sequence and comoldings with 3 types of stacking sequence.	89
Figure 4-47 Comparison between predicted and experimental elastic properties of layups and relevant comoldings with different stacking sequence.	92
Figure 4-48 Micrographs of a) top portion and b) bottom portion of the cross section of a comoulding product with stacking sequence of [0/90/+45/-45] _s	92

Chapter 1

1 Introduction

Direct-compounded long fiber reinforced thermoplastics (D-LFT) are gaining an increasing market share in the automotive industry due to mass productivity and high performance-to-cost ratio. With better mechanical properties and higher service temperature, polyamide (PA6) was selected as the matrix material to replace the most commonly used thermoplastic matrix, polypropylene (PP). As the material system of glass fiber/PA6 used in the D-LFT process has never be reported before, a fundamental investigation was performed on this new material. The aims of this work were to:

- i. build the material card and determine the proper elastic model of this material for the subsequent finite element (FE) simulation,
- ii. evaluate the effect of fiber content, processing parameters and temperature on the mechanical properties of this material,
- iii. determine the proper approach to apply a tailored reinforcement to this material.

1.1 Motivation

The main motivation for this work comes from the great lightweight potential of fiber reinforced polymers (FRPs). Increasing environmental awareness and stricter emission standards around the world give a huge drive to the development of environmentally friendly techniques, among which electric vehicles (EVs) can be the most attractive. One of the main issues that drag the wheels of an EV is the heavy battery, which limits the mileage to 300 km per charge. Replacing the traditional metallic semi-structural components with FRP based ones is considered as a good way to reduce the weight.

The second motivation is the mass productivity and relatively high performance-to-cost ratio of the D-LFT process. Of great importance to the automotive industry, the mass productivity of D-LFT is derived from the short cycle time of the thermoplastic matrix. Due to the long curing procedure, the cycle time for thermoset based FRPs is typically more than 10 minutes which is much longer than around 30 second for thermoplastic based FRPs. The relatively high performance-to-cost ratio is due to the elimination of

semi-finished products. The continuous fibers are directly incorporated with the melt to produce the final products in the D-LFT process, which significantly reduce the cost as compared with glass mat thermoplastics (GMT) and long fiber thermoplastic granulates (LFT-G).

The third motivation is to improve the mechanical properties and service temperature by using PA6 as the matrix material. PPs have been the most commonly used matrix material in the D-LFT process due to their compatibility with many processing techniques, chemical resistance, and moisture & oxygen barrier. However, the relatively low mechanical properties of PP make suppliers eager to replace them with PA6 which is type of engineering polymer. The relatively high elevated-temperature mechanical properties of PA6 may also be able to increase the service temperature of the composite material. However, the concerns about using PA6 as the matrix are its high viscosity, hydrophilicity, and oxidation-sensitivity.

1.2 Task description

As glass fiber/PA6 is a new material system for the D-LFT process, this work will investigate the mechanical behavior of this new material with focus on the effect of some fundamental factors. As an industry scaled composite processing line located at Fraunhofer Project Center for Composite Research in Western University (FPC@Western), the Dieffenbacher direct long fiber thermoplastic in-line compounding (D-LFT-ILC) line will be employed to prepare the materials involved in this work.

As one of the most important factors for the FRPs, fiber content determines the mechanical properties. The first task is to evaluate the effect of fiber content on both mechanical properties and microstructure of this new material. The ladder of fiber content is set to be 20, 30, 40, 50, 55 and 60 wt.%. Tensile, flexural, shear, impact tests will be performed to quantify the effect of fiber content on the mechanical properties. Observations of the fracture surface with a scanning electron microscope (SEM) will be employed to evaluate the effect of fiber content on the microstructure. With the measured fiber length distribution (FLD) and fiber orientation distribution (FOD), the elastic

properties of this new materials will be predicted based on existing models and compared with the experimental result.

As glass fiber/PA6 is a new material system which has never been used in this Dieffenbacher D-LFT-ILC line and the mechanical properties of FRPs are expected to be very sensitive to the processing-dependent microstructure, the second task is to evaluate the effect of the processing parameters on this new material. The focus of this work will be placed on the compounding process parameters, which include screw speed, melt temperature, filling level and fiber preheating.

Since the material will be used in an automotive structural application, it is of great importance for the original equipment manufacturers (OEMs) to have an idea how this material behaves at different temperature. The third task is to characterize the mechanical behavior of this new materials at different service temperatures. Both tensile and flexural tests will be performed in an environmental chamber to characterize the mechanical properties. SEM will be used to observe the fracture surface to analyze the failure mode.

For some parts of the component that have higher mechanical requirements, the capacity of locally adjusting the mechanical properties of this new material need to be achieved. With this task, the unidirectional (UD) tapes, in which all the fibers are continuous and aligned in the same direction, will be used to reinforce this new material. Different stacking sequences will be used to reinforce the D-LFTs in different ways, which are expected to broaden the range of mechanical properties of this material. The elastic properties of the new hybrid materials will be predicted and compared with the experimental result.

Chapter 2

2 Literature review

2.1 Fiber reinforced plastics

Owing to the great lightweight potential as semi-structural materials, fiber reinforced polymers (FRPs) are gaining more and more attention from industry, especially from automotive companies. FRPs consist of a polymer matrix and reinforcing fibers. The mechanical performance of FRPs was proven to strongly depend on the properties of matrix and fiber components as well as the interface quality [1, 2].

2.1.1 Matrix materials

The role of the matrix in FRPs is to transmit the external force to the fibers through the interface shear stress, keeping the part in shape, bond the fibers together, compensate the overloads and protect the fibers from environmental damage. The matrix-related properties such as thermal, physical and chemical properties strongly depend on the choice of matrix. Based on the matrix used, FRPs can be separated into thermosets based FRPs and thermoplastic based FRPs. The properties of some commonly used matrix polymers are listed in **Table 2-1**.

With the cross-linked 3-dimensional (3D) structure formed during the curing process, thermoset based FRPs have many advantages including good mechanical properties, high thermal resistance to creep, low pressure and temperature required for the molding, good fiber impregnating quality and low cost. These make thermosets more competitive than thermoplastics to be used as the matrix material of FRPs until now. But the further growth of thermoset based FRPs is limited by long cycle time and limited shelf life [3].

Unlike thermosets, thermoplastics are not cross-linked, which can be categorized based on the degree of crystallinity into two groups: amorphous thermoplastics and semi-crystalline thermoplastics as shown in **Figure 2-1**. The mechanical properties of thermoplastics are derived from the long molecular chains, the large degree of

Table 2-1 Properties of some commonly used resins. [1]

	Young's modulus (GPa)	Tensile strength (MPa)	Max. strain (%)	Max. operation temperature (°C)
Unsaturated polyester	3.5-4.7	50-70	2-5	100
Epoxy	2.8-3.7	70-90	2-10	200
Phenol	3.7-5.9	15-20	1-2	250
Polypropylene (PP)	1.0-2.0	25-40	100-600	80
Polyamide (PA)	3.0-3.2	80-90	70-300	100
Polyethylenimine (PEI)	3.0-3.3	80-100	60-80	200
Polyether ether ketone (PEEK)	3.6-3.8	100-120	80-100	250

entanglements between them and the high degree of molecular alignment. The reported maximum degree of crystallinity of thermoplastics can go up to 85% [1].

Attributes including high impact resistance, short cycle time, unlimited shelf life and recyclability have enabled thermoplastics to gain remarkable growth in recent years, especially in the automotive industry. However, the issues related to fiber impregnation due to high viscosity, the mechanical property degradation at elevated temperature and the creep behavior are the main drawbacks of thermoplastics, which need to be overcome in the future [4].

Polypropylenes (PPs), with the repeating units shown in **Figure 2-2**, are the most widely used thermoplastic matrix, due to the compatibility with many processing techniques, the relatively low cost, the chemical resistance and the moisture & oxygen barrier [5]. As a

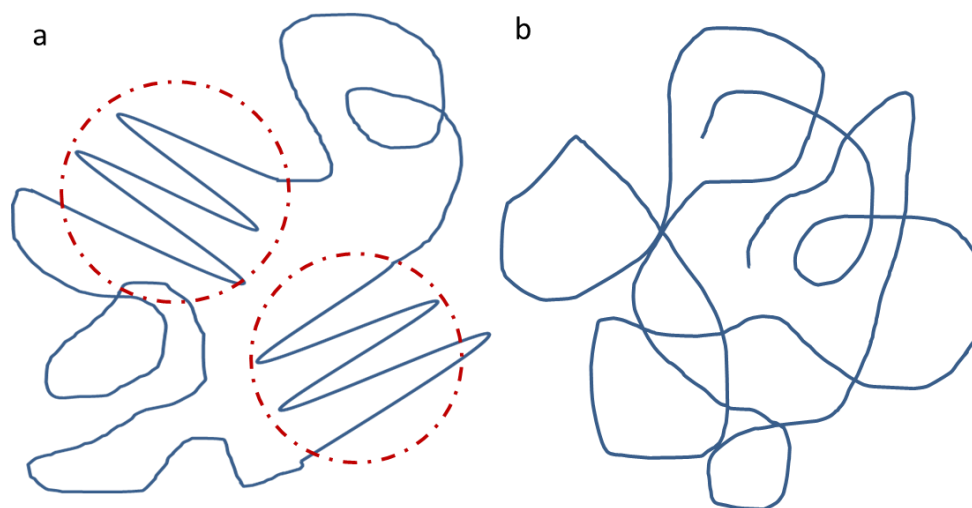


Figure 2-1 Schematic molecular structure of a) semi-crystalline thermoplastics (highlighted in red) and b) amorphous thermoplastics

semi-crystalline thermoplastic, PP can achieve a degree of crystallinity of 30-60%. However, the low mechanical properties and the low service temperature of PPs limit the growth of their application. The Young's modulus and tensile strength of PPs are just half of the typical engineering thermoplastics. With glass transition temperature (T_g) of around 10°C , the mechanical properties of PP drop significantly when temperature rises above 50°C .

Polyamides (PAs) are polymers which contain repeating amide groups ($-\text{CO}-\text{NH}-$). Proteins are an example of polyamides in nature. Artificial polyamides can be divided into two groups: aromatic polyamides and aliphatic polyamides. Benefiting from the aromatic structure and the hydrogen bonds, the aromatic polyamides have such high mechanical properties and good thermal properties that they were always used for reinforcement, such as Kevlar[®][6]. The aliphatic polyamides are very important semi-crystalline engineering polymers. The high degree of crystallinity gives polyamide excellent mechanical properties. Also attractive is their good resistance to many solvents. However, the polar amide groups make PAs vulnerable in a humid environment because the absorbed water can act as a plasticizer to degrade the mechanical properties of PAs. Moreover, the high viscosity of PA melt can create difficulties for fiber impregnation.

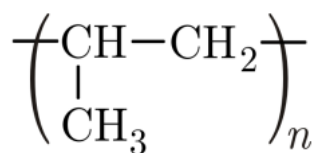
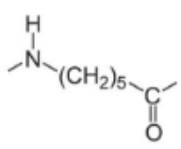
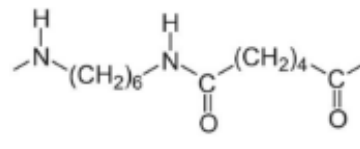
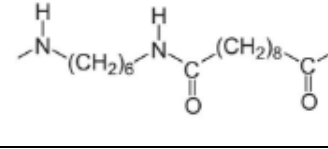
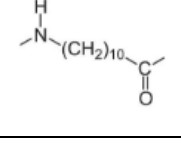
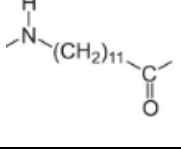


Figure 2-2 Repeating unit of polypropylene.

The nomenclature of polyamides is based on the number of carbon atoms in the repeating unit. Some examples are shown in **Table 2-2**. Among these, PA6 and PA6.6 are the most widely used. With different molecular structures, PA6.6 has better mechanical properties and lower water absorption than PA6. But the differences are very limited [7].

Table 2-2 Repeating units of different polyamides.

Type of polyamide	Repeating unit
Polyamide 6	
Polyamide 6.6	
Polyamide 6.10	
Polyamide 11	
Polyamide 12	

2.1.2 Fiber products

The vast majority of fibers used in FRPs are glass and carbon. Glass fibers are the most widely used reinforcement in industry. As shown in **Figure 2-3**, the primary constituent of glass fibers is silica (SiO_2). Silicon, aluminum, boron and oxygen atoms form the 3D cross-linked network with some modifiers of sodium and potassium. As the structure of glass fiber is amorphous, the properties are isotropic. Glass fibers have many advantages, such as high mechanical properties, good adhesion to the matrix, high service temperature, low thermal expansion, low electrical conductivity and low price.

Carbon fibers consist of small crystallites of turbostratic graphite, as shown in **Figure 2-4**. Basically, carbon fibers have a two-dimensional (2D) layered structure, in which each layer is a covalently bonded graphite single atomic layer. The different layers are connected by van der Waals forces. Carbon fibers are therefore highly anisotropic. With outstanding specific mechanical properties, carbon fibers are usually employed in high-performance applications. The main drawback of carbon fibers is the high price.

Based on the length of fiber products used, FRPs can also be classified into short fiber reinforced polymers, long fiber reinforced polymers and continuous fiber reinforced polymers. In the first two, the fibers are always discontinuous, but may have a random or preferred orientation, whereas, in the latter case, the fibers typically extend the length of the part and are aligned in the same direction.

Generally, the fiber length (aspect ratio) is of great importance to determine the mechanical properties of FRPs. The shear lag model is applied here to clarify the relationship between fiber length and mechanical properties [9]. When a composite is subjected to an external force, the fiber and the matrix are subjected to different elongations due to their different moduli. The external force is transmitted from the matrix to the fiber through the interfacial shear stress. This concept is embodied by the shear lag model as shown in **Figure 2-5**.

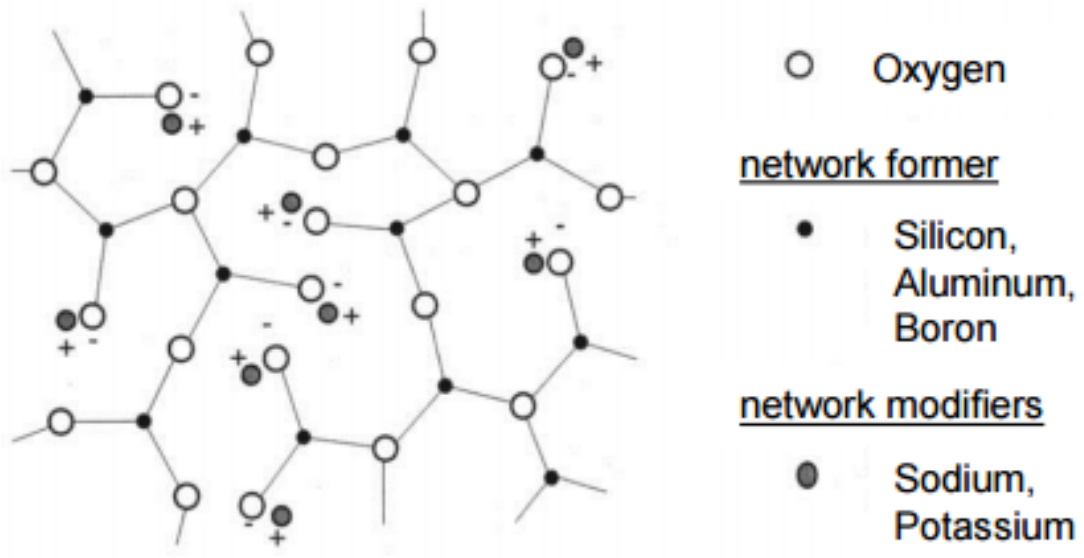


Figure 2-3 The molecular structure of glass fiber.

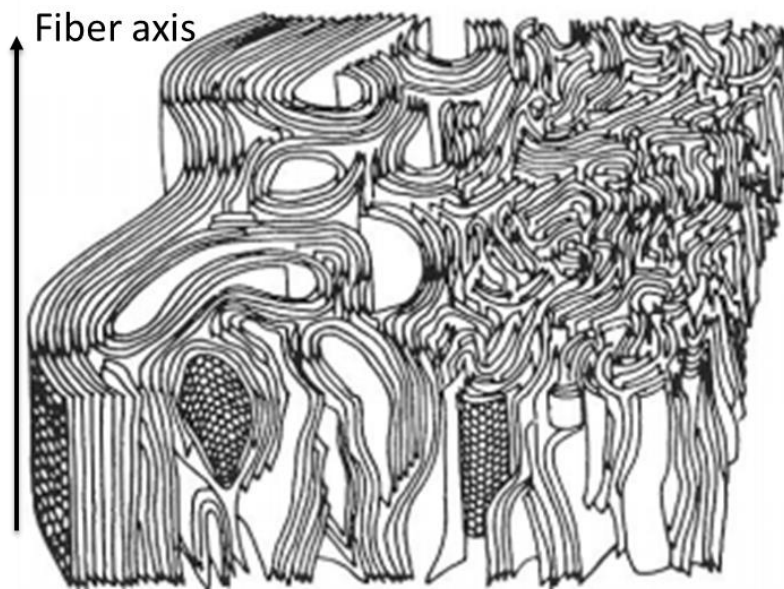


Figure 2-4 The layered structure of carbon fiber. [8]

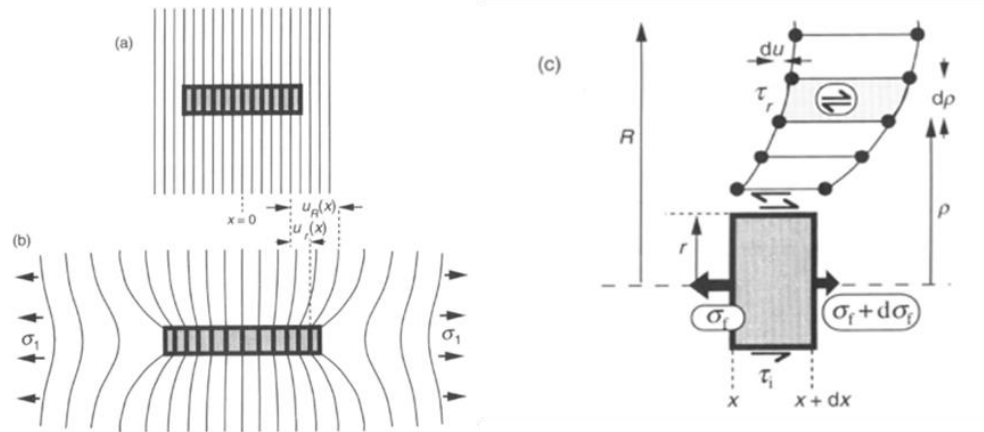


Figure 2-5 Shear lag model showing: a) unstressed system, b) axial displacements u introduced on applying tension parallel to the fiber and c) variation with radial location of the shear stress τ and strain in the matrix. [1]

Under an external force that is parallel to the fiber length, the fiber tensile stress and the interface shear stress along the fiber length can be expressed as follows:

$$\sigma_f = E_f \varepsilon_g \left[1 - \cosh\left(\frac{nx}{r}\right) \operatorname{sech}(ns) \right] \quad (2-1)$$

$$\tau_i = \frac{n \varepsilon_g E_f}{2} \sinh\left(\frac{nx}{r}\right) \operatorname{sech}(ns) \quad (2-2)$$

$$\text{With } n = \left[\frac{2E_m}{E_f(1+v_m) \ln\left(\frac{1}{V_f}\right)} \right] \quad (2-3)$$

Where σ_f is the fiber tensile stress, τ_i is the interface shear stress, x is the distance from the fiber mid-point, r is the fiber diameter, s is the fiber aspect ratio, E_f is the Young's modulus of fiber, E_m is the Young's modulus of matrix, V_f is the fiber volume fraction, v_m is the Poisson's ratio of matrix and ε_g is the global strain. **Figure 2-6** shows the predicted distribution of tensile stress and interface shear stress by **Equation 2-1** and **Equation 2-2** along the length of a glass fiber embedded in a polyester matrix. The tensile stress increases from 0 at the fiber end to a maximum at the midpoint while the interfacial shear stress decreases from a maximum at the fiber end to 0 at the midpoint.

The longer fiber with an aspect ratio of 50 enables the tensile stress to build up until the fiber and matrix have the same strain at the midpoint. For the short fiber with an aspect ratio of 5, the fiber is too short for the tensile stress to build up to the ultimate strength. That means the longer fibers enable the matrix to transfer more stress to the fibers. Therefore, the mechanical properties of FRPs can benefit a lot from the longer fibers. To fully utilize the potential of the fiber strength, the critical fiber length (l_c) is required, which is expressed as below:

$$l_c = \frac{\sigma_{uf}d}{2\tau_{ui}} \quad (2-4)$$

Where σ_{uf} is the ultimate fiber tensile strength (MPa), d is the fiber diameter (mm) and τ_{ui} is the ultimate interfacial shear strength (MPa). Thomason [10] found that the effects of fiber length and fiber diameter on impact properties are different. The fiber length is a dominating factor in notched impact tests which is generally used to determine both the impact energy and notch sensitivity while the fiber diameter has a more obvious effect in unnotched impact tests which is usually used to evaluate the complete impact resistance. Derived by Thomason et al. [11], the relationship between the fiber length and the mechanical properties of FRPs is shown in **Figure 2-7**. Obviously, the fiber length needs to reach certain critical values to fully realize the mechanical potential of FRPs.

In addition, sizing is also very essential for the resulting strength since the sizing can modify the adhesion between fiber and matrix, which normally contains a film-forming polymer, a lubricant and a coupling agent that the fibers are coated with. The functions of sizing are [1]: to protect the surface of the fibers from damage, to lubricate the fibers so that they can withstand abrasion during subsequent processing operations; to bind the fibers together for ease of processing; to impart anti-static properties and to provide a chemical link between the fiber surface and the matrix to increase the interfacial bond strength. As the exact composition of the sizing is often a commercial secret for different fiber manufactures, the fully understanding of the sizing structure is not clear. The chemical composition of sizing is also dependent on the types of fiber and matrix materials.

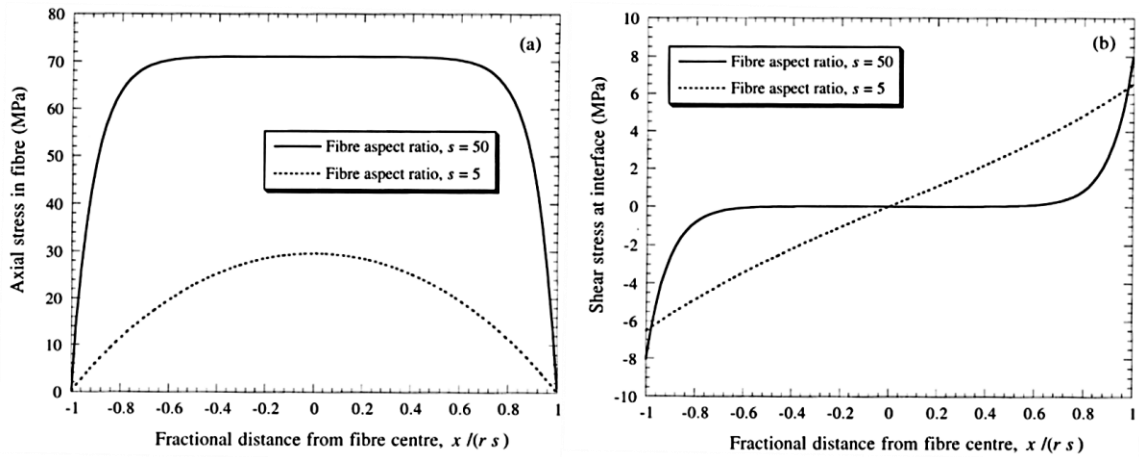


Figure 2-6 Distribution of a) tensile stress in the fiber and b) interfacial shear stress along the interface for different fiber length. [1]

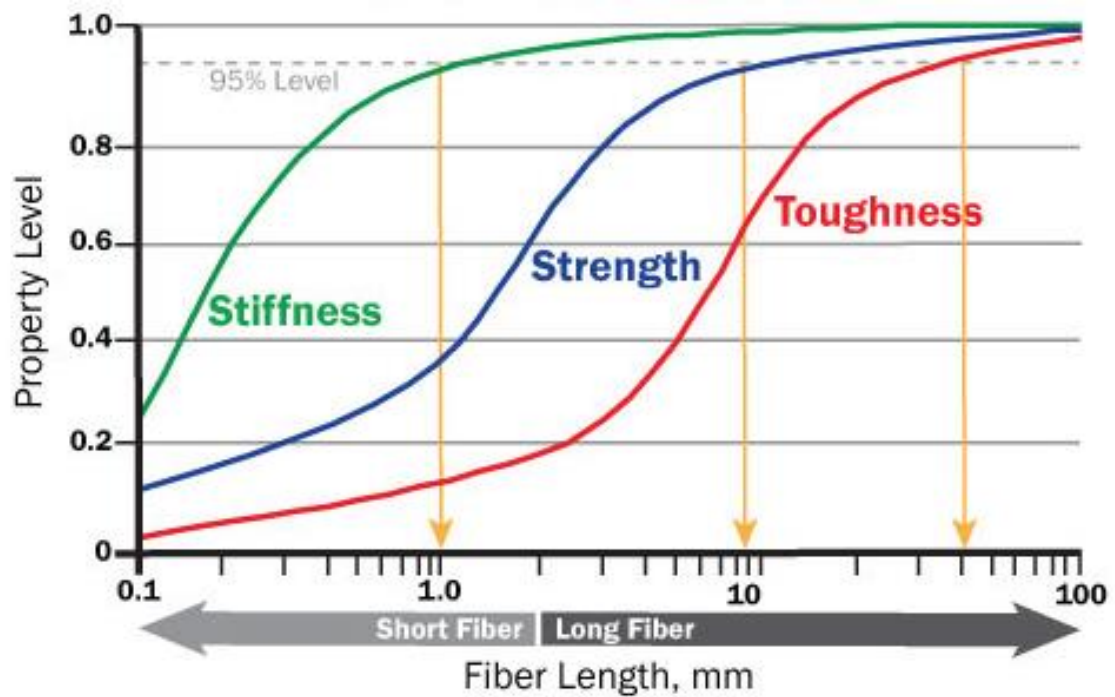


Figure 2-7 Relationship between fiber length and different mechanical properties (stiffness, strength and toughness) of PP based composites. [11]

2.2 Long fiber reinforced thermoplastics

Long fiber reinforced thermoplastics (LFT) have gained a rapid growth in the past 30 years. The main spur for that is the mass productivity of LFT due to the short cycle time of thermoplastic matrix. The contributions also come from the high performance/cost ratio, unlimited shelf life, and recyclability [4, 12-14].

2.2.1 Processing techniques for long fiber reinforced thermoplastics

The processing techniques of LFT can be classified into three categories: glass mat reinforced thermoplastics (GMT), long fiber reinforced thermoplastic granulates (LFT-G) and direct long fiber thermoplastics (D-LFT).

2.2.1.1 GMT

Dating back to 1980s, developed by PPG industries, with the schematic of the processing shown in **Figure 2-8**, GMTs were the best option to provide high mechanical properties with moderate cost, a recyclable matrix, large volume capability and thin cross-section. Initially, the continuous and randomly oriented fiber mats were heated and consolidated with the thermoplastic sheets to produce the final products. Due to the poor mobility of the composite melt, the products with inhomogeneous fiber distribution tended to fail at the resin-rich areas. To fix this issue, semi-finished glass mats with continuous fibers were replaced by glass mats made of discontinuous chopped fibers with a length of 50-100 mm. To meet the requirement of high-performance applications, the sacrificed mechanical properties could be compensated for by co-molding additional unidirectional continuous fiber products. Even though GMTs own the highest mechanical properties, the high cost weakens their competitiveness against other LFT products [15].

2.2.1.2 LFT-G

In the LFT-G processing shown in **Figure 2-9**, the polymers are heated up with additives to form a molten phase and pumped to a die-head. The continuous fiber rovings are pulled through a dispersion die and consolidated with the molten polymer to form a rod.

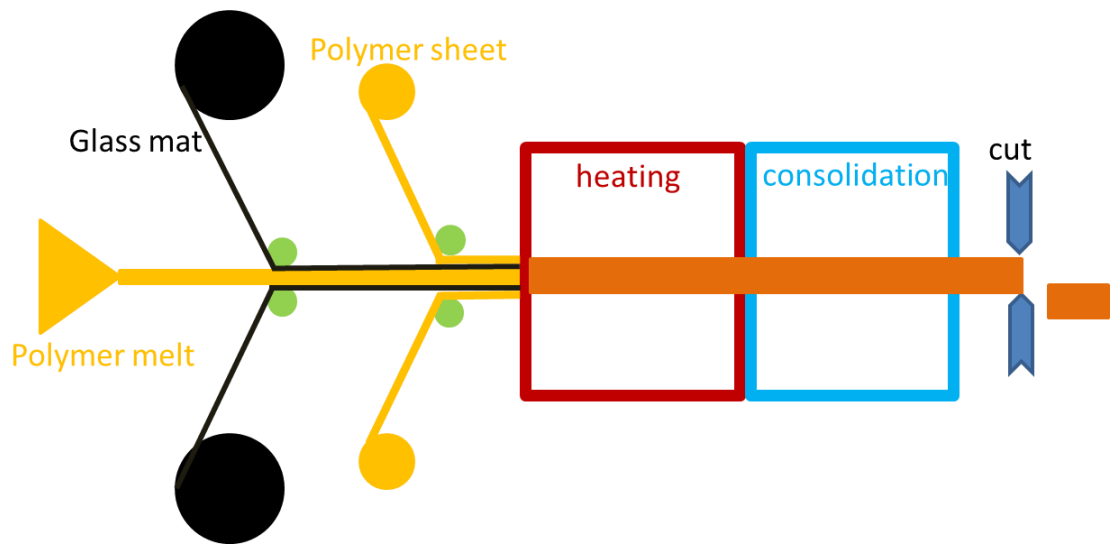


Figure 2-8 Schematic of the GMT processing technique.

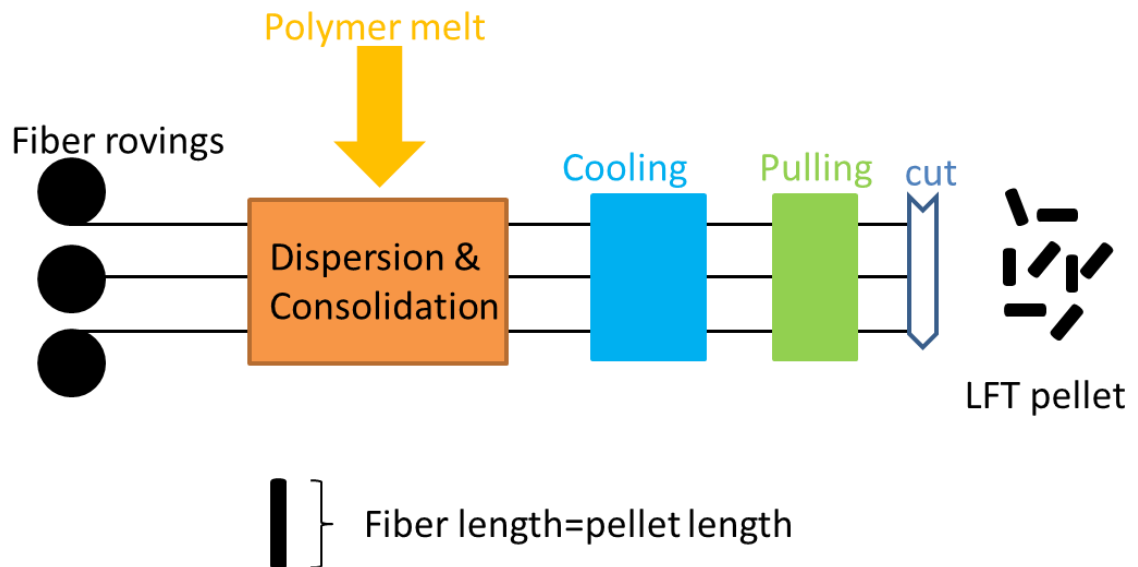


Figure 2-9 Schematic of the LFT-G processing technique.

After cooling down, the rod is chopped into many pellets with a length of 12-25mm which can be used for classic injection molding (IM), injection compression molding (ICM) or extrusion compression molding (ECM) to produce the final products. With the fiber length in glass-resin pellets increasing up to 13 mm, LFT-Gs started to compete with the traditional GMTs in structural applications [16]. With the attributes such as high

processing speed, good surface finish, and high geometrical complexity, IM is the most widely used molding process. The sacrificed mechanical properties can be improved by increasing the fiber length and fiber fraction. However, the fiber length of the pellets cannot extend 13mm because the longer fibers tend to break or clog the injection nozzle.

2.2.1.3 D-LFT

Both GMTs and LFT-Gs are making tradeoffs between the mechanical properties and the processability by using the chopped fiber mats and maximizing the fiber length of pellets, respectively. In the late 1990s, in line compounding technique (ILC), developed by molding machinery OEMs, enabled an innovative direct long fiber reinforced thermoplastics (D-LFT) process. In D-LFT processing, the continuous fiber rovings are directly incorporated and impregnated with the molten polymers during the composites compounding process and directly transferred into the mold to form the final parts [16-22].

The most important characteristic of D-LFTs is removing the requirement of the semi-finish products, like the chopped fiber mats for GMTs and the composite pellets for LFT-Gs, which significantly reduce the cost. Additionally, as the polymers undergo just one single thermal history from the raw materials to the final parts, the thermal stress and the degradation of mechanical properties can be minimized. Without the limitation of the processing efficiency of the semi-finished products, the formulations of the matrix blend including the polymers, the stabilizers, the antioxidants and the colorants can be adjusted on the site based on different applications. The type and concentration of the fiber can also be tailored through the controlled gravimetric feeder, the screw speed and the amount of fiber rovings fed into the extruder. Those benefits give the designers a high degree of freedom to control the range of performance of the final product.

2.2.1.4 Compression molding and injection molding

The biggest advantage of compression molding over injection molding is the short cycle time. Additionally, the shear stress during the compression molding is moderate, which leads to less degradation of the fiber length. The longer fibers can improve the

mechanical properties and reduce the warpage. The freedom of charge placement in the mold enables the optimization of the flow for products with different geometry, which aids in minimizing the component thickness [13].

2.2.2 Influence of fiber content on the mechanical properties of LFT composites

Generally, raising the fiber content is the simplest way to improve the mechanical properties of LFTs. Fiber volume fraction (FVF) is also a very important parameter for the prediction of the mechanical properties of LFTs. Though difficult to be measured experimentally, FVF can be calculated by the fiber weight fraction (FWF) based on the density of the matrix and the fiber as follows:

$$V_f = \frac{W_f \rho_f}{W_f \rho_f + W_m \rho_m} \quad (2-5)$$

Where V , W and ρ are the volume fraction, weight fraction and density, respectively. The subscript f and m represent the fiber and the matrix, respectively. The mechanical properties can be improved by increasing the fiber volume fraction because there are more fibers bearing the load. However, when the fiber volume fraction is too low (<10 wt.%), the fibers may serve as stress concentration points and do harm to the mechanical properties. The effective fiber volume fraction is often limited to a certain range of values based on different processing techniques and material systems.

According to the previous works on the effect of fiber content on mechanical properties of LFTs [23-37], it was observed that increasing the fiber content improves the mechanical properties at low fiber content range, whereas the efficiency of the improvement drops significantly at high fiber content range. The effect of fiber content also varies for different mechanical properties, which will depend on the fiber length.

Thomason et al. [29, 30] conducted an experiment to investigate the mechanical performance of injection molded long glass fiber reinforced PP over a fiber content range of 0-73 wt.%. It was found that the Young's modulus increases linearly over the whole range while the strength and the impact properties show maximum values at the fiber

content of around 40 wt.% and approach to the properties of unreinforced PP at 73 wt.%. The elongation of the composite sample decreases with the increasing fiber content. The higher fiber content is found to degrade the average fiber length, reduce the preference of fiber alignment and reduce the interfacial shear strength at the same time, which might serve as the interpretation of the variation of the strength and impact properties.

Lee et al. [23] studied the effect of fiber content on the mechanical properties of glass fiber mat/polypropylene composites. As the fiber content increases, both tensile and flexural modulus show a linear increase. But the reinforcing effect at high fiber content is reduced by the higher void content. Both the impact properties and the strength go down when the fiber content is increased beyond 20 wt.%. This is explained by the degraded interface bonding and the severe stress concentration around the fiber ends.

Bowland [32] evaluated the effect of coupling agent, fiber content and resin properties on the mechanical properties of long glass fiber reinforced PP. Within the whole fiber content range of 30-50 wt.%, the tensile and flexural properties were found to increase as fiber content went up.

According to Han et al.'s work [34] on injection molded long fiber reinforced PA6. The tensile and flexural properties were improved by increasing fiber content up to 50 wt.%. The notched impact strength hit the peak at the fiber content of 40 wt.%. The reason for that is referred to the degradation of fiber length caused by more fiber-fiber frictions during the injection molding.

However, most researches focusing on effect of fiber content on mechanical properties of LFTs were performed on LFT-Gs which have much short fiber than D-LFT. The findings in LFT-Gs may not be directly applicable to D-LFT since the effect of fiber content on mechanical properties is dependent on the length of fiber products used. The maximum effective glass fiber content of short fiber reinforced thermoplastics (typically 30 wt.%) is also smaller than that of long fiber reinforced thermoplastic (typically 50-60 wt.%).

2.2.3 Influence of processing parameters on the mechanical properties of LFT composites

Generally, the mechanical properties of LFTs are very sensitive to the microstructure, which is controlled through the compounding and molding process. Normally, the compounding process has more influence on the quality of impregnation and the distribution of fiber length [38-49] while the molding process dominates the distribution and orientation of fibers [50-58].

In the molding process, the melt flow is the key to be controlled. As affected by many parameters including geometry of the mold, material viscosity, fiber length, mold temperature, mold pressure, location of injection point (injection molding) and charge position (compression molding), the melt flow during the molding process is very complex even for a simple specimen, which make it very difficult to model the whole process and predict the resulting fiber alignment.

The compounding process is also of crucial importance due to its significant effect on resulting fiber length through the shear flow. Since most of the compounding equipment is based on the single or twin screw extruder system, the parameters including screw configuration, melt temperature, screw speed, filling level and dimension of the extruder need to be examined. A contradiction exists in adjusting the parameters of the second extruder to achieve good mixing quality and high fiber length. The high shear effect which improves the mixing quality is not preferred if large average fiber length is needed. Therefore, adjustment of the compounding processing parameters requires making a tradeoff.

Much efforts were made to optimize the screw design. As shown in **Figure 2-10**, many geometric parameters of the screw including the barrel diameter D_b , the centerline distance A , the clearance screw-barrel C_b , the clearance screw-screw C_s , the flight pitch p , the number of flights j , the inner screw diameter D_i , the outer screw diameter D_o and the free volume B can be adjusted to modify the shear effect [44, 47].

Huembert [44] experimented with the effect of screw design on the fiber length and the mechanical properties of glass fiber reinforced PA6 D-LFT composites, which is based on the same processing line with this work. As shown in **Figure 2-11**, four types of screws with different shear effect were used to produce the plaques with 30 wt.% fiber. The standard screw design is the one used in this work. It is found that the average fiber length decreases linearly as the shear effect of the screw increases. But the variation of the mechanical properties is very limited.

Shimizu et al. [41] analyzed the fracture process of glass fibers contained in a glass fiber reinforced PP composites, which occurs in the kneading zone of a twin-screw extruder. It was found that the fiber length distribution depends upon the shear stress and the total number of rotations.

Stade's work [59] on two stage production-scale continuous kneaders help defining the major processing factors on the fiber length of the finished products. Stade derived the relationship between different processing parameters and fiber length empirically as

$$k = \frac{(L_2)(\rho)(f)(N)(A_f)}{F} \quad (2-6)$$

where k is the key factor for the average glass fiber length in composites, L_2 is the length of the mixing section of extruders, ρ is the average density of the melt, f is the filling ratio, N is the screw speed, A_f is the free cross section of the extruder, and F is the feeding rate of the composites. The relationship indicates that melt with higher density, higher filling level, and higher screw speed can reduce the degradation of fiber length during the compounding.

Fisa [39] performed an experiment to study the effect of viscosity, total work, concentration on the fiber length and dispersion of glass fiber reinforced PP. The degradation of fiber length was reported to be derived from both fiber-fiber and fiber-melt interaction. The matrix viscosity has a more significant effect on the average fiber length than does the incorporation process of the fiber.

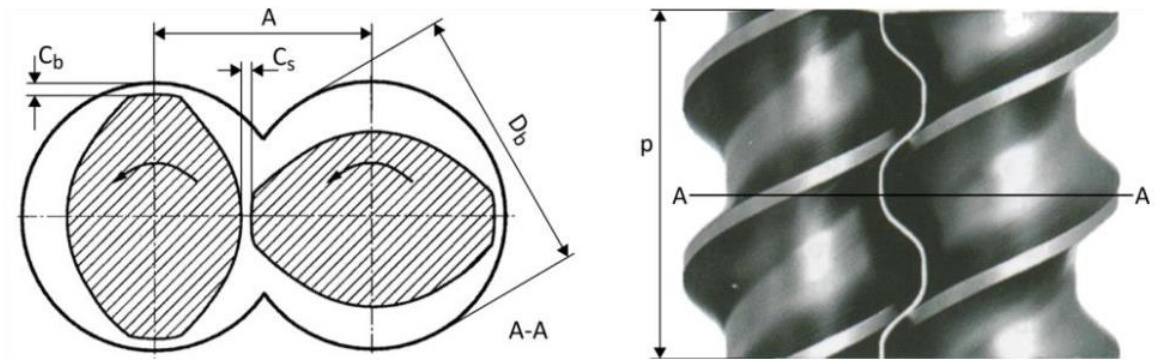


Figure 2-10 Parameters involved in screw design: barrel diameter D_b , centerline distance A , clearance screw-barrel C_b , clearance screw- screw C_s and flight pitch P .

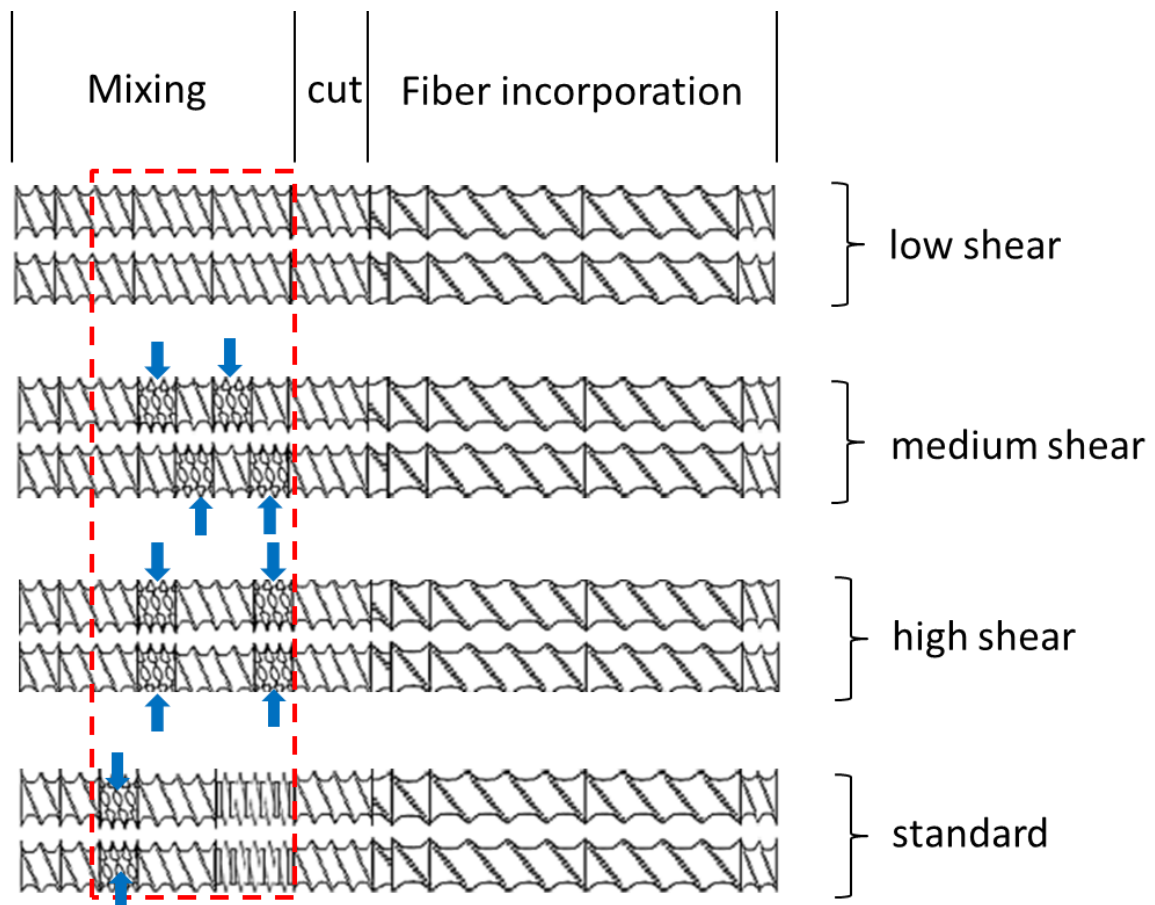


Figure 2-11 Four types of twin-screw designs with different placements of high mixing elements resulting in different shear flow. [44]

Czarnecki and White [40] proposed a mechanism for fiber breakage based on the buckling during rotation in the shear flow. They also found the viscosity increasing is only due to the enhanced viscous dissipation.

Yilmazer and Cansever [45] prepared glass fiber reinforced PA6 through injection molding with different screw speed and feed rate. It is found that the increasing shear rate through the alteration of screw speed and feed rate significantly reduce the fiber length. Accordingly, the impact strength, the tensile modulus, and the tensile strength increase while the global elongation decreases with the increasing shear rate.

Priebe and Schledjewski [46] studied the effect of processing parameters in a twin-screw extruder on the fiber length of the materials extruded. It is found that utilizing the PP products with higher viscosity led to higher fiber length but lower mechanical properties which might be caused by some other effect of processing parameters on the material. The high screw speed significantly degrades the fiber length as expected. But the effect of screw configuration and fiber content were limited.

Ozkoc et al. [35] reported that the increasing screw speed reduced the fiber length and had some negative effect on the mechanical properties. An increased extrusion temperature had a positive effect on the fiber length and, therefore, improved the mechanical properties.

These findings illustrate that the key factor to be controlled in the compounding process in a twin-screw extruder is the shear flow of the melt. The adjustment of many parameters can result in the variation of mechanical properties. However, the rule derived from each work was based on a specific processing line and a specific material system, which might not be directly applicable to other work that is based on a different processing line and material system.

2.2.4 Environmental effect on the mechanical properties of LFT composites

In service, the LFT components will be exposed to different environments, such as varied temperature, water, sunshine and acid rain. If the LFT parts are exposed to these environments for a long time or cyclically, the mechanical properties are likely to be degraded. It is very important to quantify the extent of the degradation to ensure safety. A great deal of research has been conducted to investigate the effect of these environmental factors on both the microstructure and properties of LFTs.

Moisture can affect LFTs through attacking fiber, matrix, and interface (**Figure 2-12**). The absorbed water can promote creep and stress relaxation, generate residual stress and osmotic pressure, and cause hydrolysis and chemical reaction. Fatigue degradation can be accelerated by moisture as well, which can provide new paths for the moisture ingress.

Moisture damage starts near the surface with the growth of some local cracks [60]. The degradation of LFTs is also related to the absorption of moisture through capillary action and diffusion, which can be accelerated by voids and delaminations [61-63].

Hydrothermal aging has a significant effect on LFTs. Both strength and toughness were shown to decrease as the immersion time increases [64]. Dry-wet cycling increased the rate but hardly affected the maximum content of the water absorption [65]. Aggressive temperature variation will also promote moisture absorption [64, 66]. It has been observed that glass fiber degrades more than carbon fiber under the same condition [67].

Matrices are the main victim of moisture attack, resulting in plasticization, swelling, hydrolysis and fiber-matrix debonding [68]. Plasticization can decrease the glass transition temperature (T_g), soften the polymer and increase creep deformation, although these effects are reversible on drying [60, 51, 67]. However, hydrolysis is irreversible, which can degrade both stiffness and strength [64, 67]. Swelling can deteriorate the bonding between fiber and matrix, which tends to form a continuous crack after cycling [60, 64, 67].

At the fiber level, glass fiber is the most vulnerable to moisture attack. Moisture can degrade glass fiber chemically, resulting in reduction of strength, fiber pitting and stress-corrosion cracking [62-71].

Beg and Pickering [72] studied the hydrothermal aging behavior of virgin and reprocessed wood fiber reinforced PP. After immersion in distilled water at 50°C over 9 months, the tensile strength, the Young's modulus, and the hardness of samples

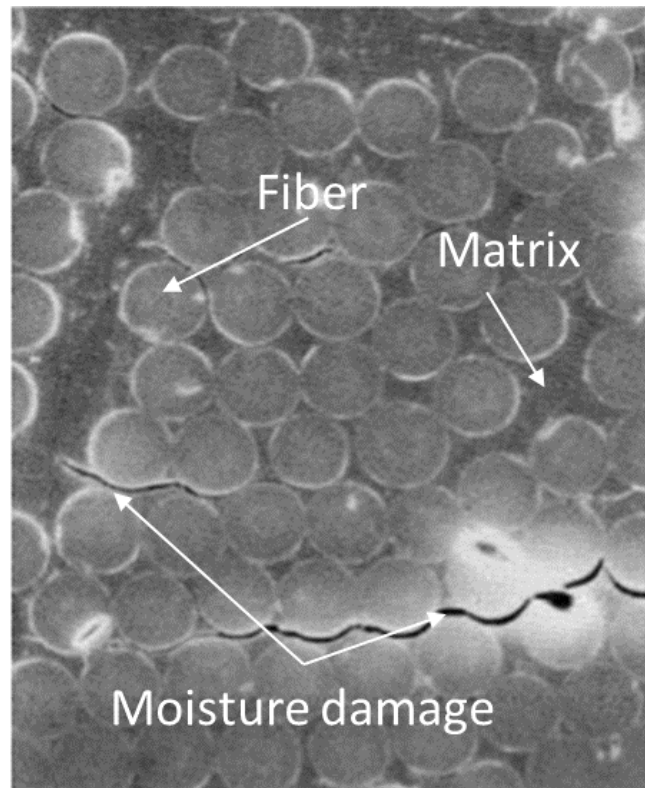


Figure 2-12 Local cracks caused by moisture absorbed in composites. [60]

decreased while the impact strength and the failure strain increased. The water uptake was shown to decrease after reprocessing.

Valentin [73] investigated the hydrothermal behavior of glass fiber reinforced PA6.6 composites. When the temperature is lower than the T_g , Fick's law can be employed to model the water absorption process. When the temperature is higher than T_g , thermal aging, oxidation, and leaching may disturb the behavior. The water uptake also leads to

the shift of T_g. The same water uptake tends to have a greater effect on the mechanical properties of short fiber composites than long fiber counterparts.

Compared with fibers, polymers are more susceptible to thermal effects. Lower temperatures make the polymer more brittle to easily crack whereas the higher temperature softens the polymer resulting in lower stiffness, chalking, and flaking of the polymers [27, 74-91]. The softened matrix becomes deformable and less able to transfer the stress to the fibers [63].

Thermal effects on the interface between fiber and matrix are the primary cause of the mechanical degradation. Due to the distinct thermal expansion coefficients of fiber and matrix, the shrinkage after cooling can generate a large stress concentration and residual compressive stress. The former may serve as the crack initiating spot while the latter can contribute to the interfacial shear strength [92-97]. The variation of temperature alters the distribution of stress along the interface, which can have a complex effect on the mechanical properties.

Thomason [27] researched the temperature dependence of the interfacial properties of glass fiber reinforced PP composites at the temperature range of -40-100°C. The result indicated that around 70% of the interfacial shear strength is derived from the residual radial compressive stress which can be released by increasing temperature [78]. He also reported that the heat deflection temperature (HDT) depends on both fiber length and fiber concentration. Both longer fiber and higher fiber content can raise the HDT close to the melting point of PP. That means the thermal effect on the mechanical properties of LFT is correlated to the fiber length and the fiber concentration.

2.2.5 UD tape reinforcement on D-LFT composite

For a real part with complex geometry, the requirement of mechanical properties for certain area, like one with stress concentration, might be higher than the rest. To efficiently make use of the material, some local reinforcements may be required. With respect to the design of geometry, some strengthening ribs can be added to the part.

However, this method may cause filling issues, especially for thermoplastic based composites.

Another approach is to tailor the material properties locally. As mentioned above, once the fiber content is determined for D-LFTs, the mechanical properties just depend on the fiber orientation distribution within the whole product. Since the flow effect is difficult to adjust, the mechanical properties of LFT product are also hard to locally improve.

As shown in **Figure 2-13**, the continuous fiber products with higher fiber fraction and more consistent fiber alignment have better performance but less freedom of design than

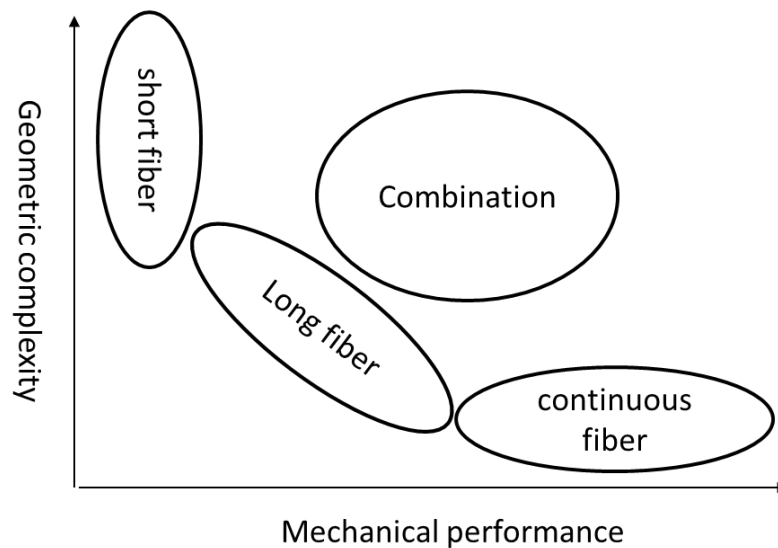


Figure 2-13 Comparison between the FRPs based on different fiber products. [100]

LFT, while LFTs have more freedom of design but lower performance. Borrowed from GMT processing, tailored D-LFT is an innovative technique using the continuous fiber tapes, in which all the fibers were continuous and aligned in the same direction, to locally co-mold with D-LFT to take the benefits of both [98-108]. Additionally, the configuration of the tapes including the type of materials, the fiber fraction, the stacking sequence and the thickness can offer more freedom of design to the engineer.

Thattai parthasarthy [107] compared the damage tolerance of LFT reinforced with ribs and unidirectional tapes, respectively. Without changes in the processing, the co-molded UD tapes enhance the flexural properties for equivalent rigidity compared to rib reinforcement. The failure of LFTs got more ductile with tape reinforcement. The tape reinforcement improves both flexural strength and failure displacement.

Grauel et al. [100, 101] co-molded a D-LFT automotive underbody shield with UD tapes to improve the mechanical performance. The result clarified that tailored D-LFT technique has a great potential to reduce both cost and mass with improved mechanical properties. The co-molded tapes yield the parts with improved impact strength.

In Fang's work [104], the effect of thickness of co-molded UD tapes on the mechanical properties of the whole hybrid composite was studied. It was discovered that the UD tapes could improve toughness significantly with little effect on modulus and strength.

Ruegg et al. [98] used different studies of structural components, implicit and explicit finite element calculation with validation in a sled-test-front-crash with luggage retention to derive the advantages of the combination of UD tapes and LFT over other current solutions.

2.3 Prediction of mechanical properties of long fiber thermoplastic

To predict the mechanical behavior of LFTs, many factors such as constituent material properties, fiber volume fraction, fiber length distribution and fiber orientation distribution need to be measured. It is crucial to understand the correlation between the mechanical properties and these factors.

The elastic properties of UD composites are the best option to start with, in which materials properties and fiber volume fraction are the only two variables. With an assumption that the mechanical properties of UD are transversely isotropic, the compliance matrix of UD $[S]$ can be determined by 5 independent constants: axial Young's modulus (E_{11}), transverse Young's modulus (E_{22}), axial shear modulus (G_{12}),

transverse shear modulus (G_{23}) and major Poisson's ratio (ν_{12}). The compliance is expressed as below:

$$[S] = \begin{bmatrix} 1/E_{11} & -\nu_{12}/E_{11} & -\nu_{12}/E_{11} & 0 & 0 & 0 \\ -\nu_{12}/E_{11} & 1/E_{22} & -\nu_{23}/E_{22} & 0 & 0 & 0 \\ -\nu_{12}/E_{11} & -\nu_{23}/E_{22} & 1/E_{22} & 0 & 0 & 0 \\ 0 & 0 & 0 & 1/G_{23} & 0 & 0 \\ 0 & 0 & 0 & 0 & 1/G_{12} & 0 \\ 0 & 0 & 0 & 0 & 0 & 1/G_{12} \end{bmatrix} \quad (2-7)$$

The rule of mixture (ROM) is the most basic approach being used to calculate these 5 constants. It is based on two types of slab model as shown in **Figure 2-14**: iso-strain model (Voigt model) and iso-stress model (Reuss model) [109, 110].

Two types of slabs represent the fiber and matrix with an assumption of perfect bonding. In the iso-strain model, fiber and matrix have the same strain in the load direction. Then the axial Young's modulus and major Poisson's ratio can be derived as follows:

$$E_{11} = V_f \cdot E_f + V_m \cdot E_m \quad (2-8)$$

$$\nu_{12} = V_f \cdot \nu_f + V_m \cdot \nu_m \quad (2-9)$$

Where, 1 is the axial direction, 2 is the transverse direction, V is the volume fraction, E is the Young's modulus, ν is Poisson's ratio, subscript f represents the fiber and subscript m represents the matrix. In the iso-stress model, fiber and matrix bear the same stress in the load direction, from which the shear modulus and transverse Young's modulus can be derived as follows:

$$E_{22} = \frac{E_f \cdot E_m}{E_m \cdot V_f + E_f \cdot V_m} \quad (2-10)$$

$$G_{12} = \frac{G_f \cdot G_m}{G_m \cdot V_f + G_f \cdot V_m} \quad (2-11)$$

The prediction for E_{11} and ν_{12} using ROM matches well with experimental result while that for E_{22} and G_{12} is often lower than the experimental results. That is caused by the inhomogeneous stress distribution within the matrix. To fix this problem, several models were developed to predict E_{22} and G_{12} with different assumptions, such as Modified Rule of Mixture, Halpin-Tsai model [111], Chamis model [112], composite cylinder

assemblage method (CCS) [113], Mori-Tanaka model [114], Bridging model [115, 116] and Eshelby method. Among these, as taking account of the enhanced fiber load bearing, the Halpin-Tsai model is the most successful and widely employed. The empirical expression is shown as follows:

$$E_{udi} = E_m \cdot \left(\frac{1 + \zeta_i \eta_i V_f}{1 - \eta_i V_f} \right) \quad (2-12)$$

$$\text{with } \eta_i = \left(\frac{\frac{E_f}{E_m} - 1}{\frac{E_f}{E_m} + \zeta} \right) \quad (2-13)$$

Where $\zeta_1 = 2L/d$ and $\zeta_2 = 2$, E_m is the Young's modulus of matrix, V_f is the fiber volume fraction. L is the fiber length and d is the fiber diameter.

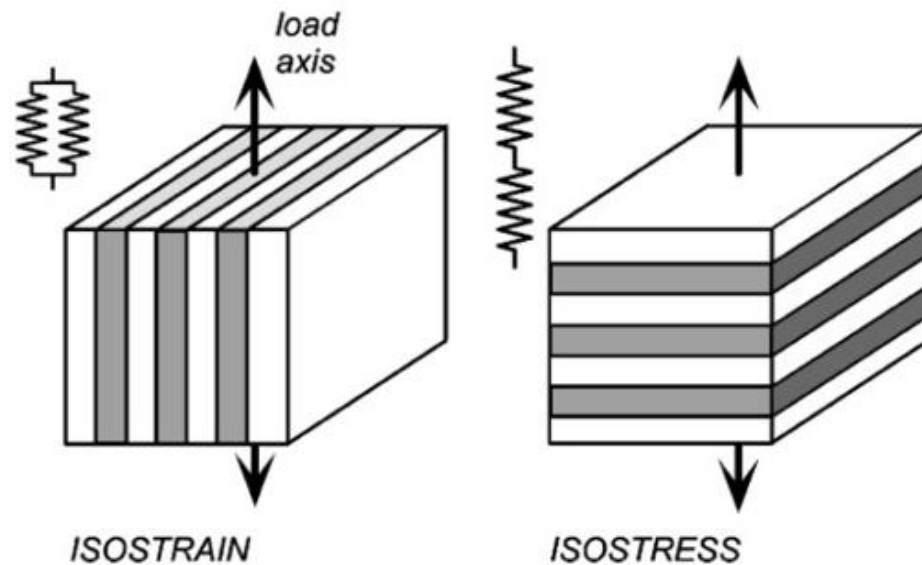


Figure 2-14 Voigt (iso-strain) model and Reuss (iso-stress) model for composite material elasticity.

Since the fibers in LFTs are discontinuous and partially aligned in the flow direction, the prediction of the mechanical properties needs to take both fiber length distribution (FLD) and fiber orientation distribution (FOD) into account. Currently, three approaches are often employed to predict Young's modulus. The first one is based on the shear lag

model developed by Cox [117] and improved by Krenchel [118]. The expressions are shown as follows:

$$E_{11} = k_1 k_2 E_f V_f + E_m (1 - V_f) \quad (2-14)$$

$$\text{with } k_1 = \left[1 - \frac{\tanh\left(\frac{\beta L}{2}\right)}{\frac{\beta L}{2}} \right] \quad (2-15)$$

$$\beta = \frac{2}{d} \left[\frac{2G_m}{E_f \ln \sqrt{\frac{\pi}{X_i V_f}}} \right] \quad (2-16)$$

$$k_2 = \sum_i a_i \cos^4 \theta_i \quad (2-17)$$

Where E_f and E_m are the Young's moduli of fibers and matrix, respectively. The effect of FLD and FOD were involved by inducing fiber length factor k_1 and fiber orientation factor k_2 . L and d are the length and diameter of fibers, respectively. X_i depends on the geometrical packing arrangement of fibers and can be set as 4 [24]. V_f is fiber volume fraction. a_i represents the fiber proportion making an angle θ_i with the load direction.

The second method is based on the Halpin-Tsai model [29]. As mentioned before, Halpin-Tsai has already involved the effect of fiber length. Young's modulus in longitudinal E_{UD1} and Young's modulus in transverse directions E_{UD2} of unidirectional discontinuous fiber can be predicted based on equations (2-11) and (2-12). With the fiber orientation factor k_2 calculated by equation (2-16), the Young's modulus of partly aligned discontinuous fiber composites can be predicted as:

$$E_c = k_2 E_{UD1} + E_{UD2} (1 - k_2) \quad (2-18)$$

The third approach is based on laminate analogy approach (LAA) with an assumption that the specimen is shell-like to enable the condition of a planar FOD. Developed by Fu and Lauke [119] with an inspiration from paper physical approach (PPA), the expression of longitudinal and transverse Young's moduli is shown as follows:

$$E_{11} = \frac{Q_{11g} \cdot Q_{22g} - Q_{12g}^2}{Q_{22g}} \quad (2-19)$$

$$E_{22} = \frac{Q_{11g} \cdot Q_{22g} - Q_{12g}^2}{Q_{11g}} \quad (2-20)$$

$$\text{With } Q_{ijg} = \int_{L_{min}}^{L_{max}} \int_{\theta_{min}}^{\theta_{max}} \overline{Q_{ij}} f(L) g(\theta) dL d\theta \quad (2-21)$$

Where Q_{ijg} 's are overall stiffness terms obtained by integrating the transferred stiffness matrix of aligned composite $\overline{Q_{ij}}$ along with fiber length $f(L)$ and orientation $g(\theta)$ density functions.

Fu and Lauke [120] also developed an approach to predict the tensile strength of LFT by accounting for the dependence of the ultimate fiber strength and the critical fiber length on the inclination angle θ , which is based on modified rule of mixture. The expression is shown as follow:

$$\sigma = k_2 V_f \sigma_{uf} \left(\int_0^{L_c} f(L) \left[\frac{L}{2L_{cr}} \right] dL + \int_{L_{cr}}^{\infty} f(L) \left[1 - \frac{L_c}{2L} \right] dL \right) + \sigma_{um} (1 - V_f) \quad (2-22)$$

Where σ_{uf} is the ultimate fiber tensile strength, L_c is the critical fiber length which can be calculated based on **Equation 2-4** and σ_{um} is the tensile strength of the matrix.

2.4 Summary

Fiber content, processing parameter and temperature can all affect the mechanical properties of LFT. But the previous findings about the correlation between these factors and the mechanical properties of LFT are based on different processing lines and different material systems. For the material investigated in this work, the new combination of PA6 with glass fiber for D-LFT and the much long fibers might lead to different rules. Therefore, it is worth to evaluate the effect of fiber content, processing parameter, temperature on the mechanical properties and determine a proper way to apply a tailored reinforcement for the PA6/Glass fiber D-LFT composite material.

Chapter 3

3 Experimental

3.1 Materials

PA6 (Ultramid 8202HS) provided by BASF and glass fiber (JM 886) provided by John Manville (JM) were used in this work. The Ultramid 8202 HS is a heat stabilized, low viscosity, general purpose PA6 which possesses the combination of strength and toughness and has excellent chemical and abrasion resistance. The JM 886 glass fiber is characterized by a pioneering reactive sizing designed for structural thermoplastic composites with polyamide engineering polymers. Physical and mechanical properties of these two products are listed in **Table 3-1**.

3.2 Preparation

3.2.1 Dieffenbacher D-LFT-ILC line

Preparation of all the specimens involved in this work was performed at the FPC@Western. The key equipment was a Dieffenbacher direct long fiber reinforced thermoplastics in-line compounding (D-LFT-ILC) line, of which the schematic is shown in **Figure 3-1**. During processing, polymer granules and additives were dried and fed into the first extruder to undergo a thorough compounding. Then the molten matrix blend was extruded out through a film die into the second extruder. Simultaneously, continuous fibers were integrated from the top of the melt film and continuously pulled into the second extruder by the screw rotation. In the second extruder, the continuous fibers were chopped by a specially designed cutting element of the twin-screw and smoothly dispersed by shear effect of the melt. Mixed compounds were continuously coming out through a servo die and cut into charges by a shear blade. The charges were kept warm on an insulated conveyor and transferred manually into a tool to undergo compression molding. Compared with other competing directly compounded long fiber reinforced thermoplastic (D-LFT) lines, separation of polymer plasticizing and fiber integration is the most attractive characteristic of this D-LFT-ILC line. High screw speed and screws with high shear configuration can be used in the first extruder to guarantee a thorough

Table 3-1 Properties of PA6 (Ultramid 8802HS) and glass fiber (JM 886) used in this work.

	PA6	Glass fiber
Supplier	BASF	Johns Manville
Product	Ultramid 8802HS	JM 886
ρ (g/cm ³)	1.13	2.63
E_{11} (GPa)	2.7	70
E_{22} (GPa)	2.7	70
G_{12} (GPa)	0.93	30
τ (MPa)	45	866
σ_t (MPa)	78	1500
ν_{12}	0.45	0.17

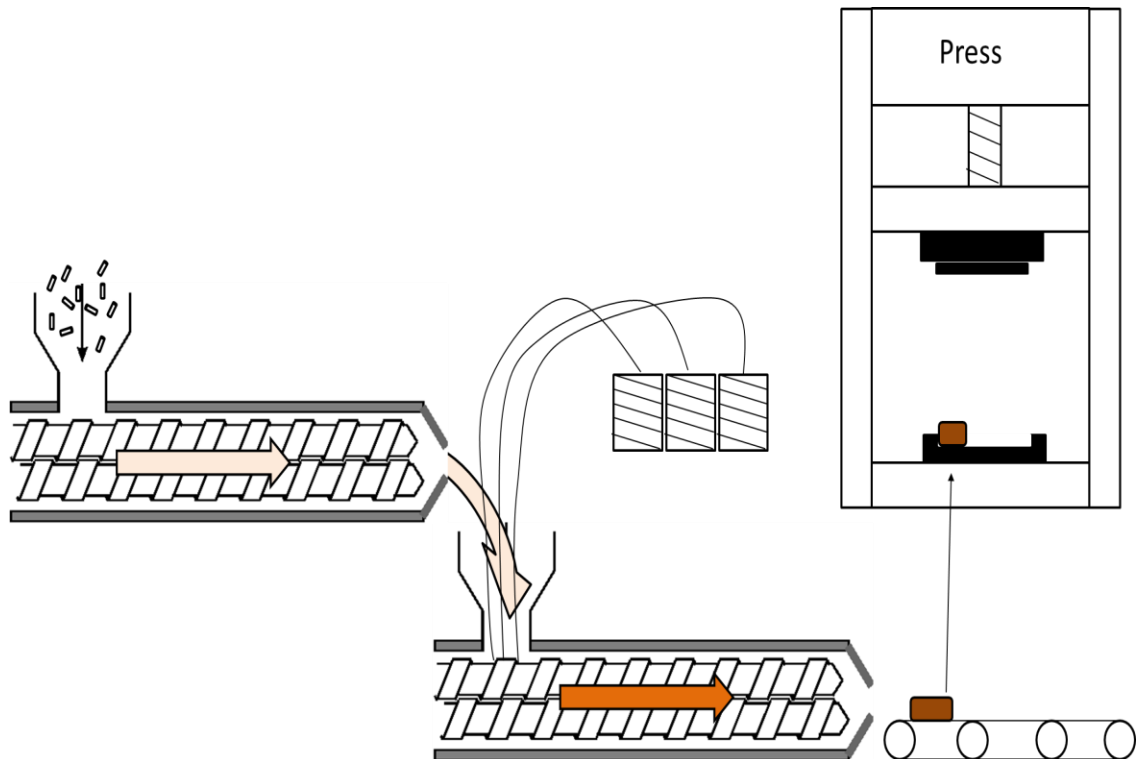


Figure 3-1 Schematic of Dieffenbacher D-LFT-ILC line.

compounding, while moderate screw speed and screws with moderate shear configuration can be used in the second extruder to attain long fibers. Additionally, the separation of two extruders can also reduce the wear of screws in the first extruder due to the absence of fiber during melting process.

3.2.2 D-LFTs with different fiber contents

Glass fiber/PA6 D-LFT plaques with fiber contents of 20, 30, 40, 50, 55, 60 wt.% were prepared. As shown in **Figure 3-2**, PA6 pellets were pumped into the dryer and maintained at 80°C for around 12 hours. Then the dried PA6 pellets were pumped in to a gravimetric dosing system which control the feeding rate during processing. The solid PA6 pellets were automatically fed into the first extruder, as shown in **Figure 3-3**, which is called ZSE. ZSE is a co-rotating, closely intermeshing and self-cleaning Leistritz ZSE 60/GL unit with an L/D ratio of 32. The temperature of ZSE was set to be 260°C which was above the melting point of the PA6. Degassing took place with vacuum assist. The compound melt exited the first extruder through a film die at the end. Simultaneously, the continuous glass fiber rovings were separately fed through a plastic tube system, as shown in **Figure 3-4**, and introduced from the top of the melt film into the second extruder. The separation apparatus above the second extruder and the film die of the first extruder were both used to increase the contact area of fiber and melt to improve the impregnation. Optionally, the fibers can be preheated by going around several hot iron bars to further improve the impregnation.

In the second extruder, as shown in **Figure 3-5**, continuous fibers were chopped into discontinuous fibers with a length range of 20-40 mm by a specially designed cutting element. Complex shear effect generated by the co-rotation of screws dispersed and impregnated the fibers. However, the aggressive shear effect might also result in some damage to the fibers. The screw design of the seconded extruder used in this work has a high shear design, which is shown in **Figure 2-11** and labelled as standard.

To give an idea of how fiber content was adjusted, the schematic of second extruder is shown in **Figure 3-6**. The fiber content of composites is consistent with that of each

revolution. As the filling level, which means the volume of the filled space in each revolution, was stable during the process, the output rate of compound was determined by the filling level and the screw speed. The input of matrix melt and the number of fiber rovings were used to adjust both filling level and fiber content. Therefore, if the filling level is fixed, increasing the fiber content can be achieved only by increasing the number of fiber rovings and reducing the screw speed of ZSE at the same time.

As shown in **Figure 3-7**, the composite compound was coming out through a servo die and automatically cut into charges by a shear blade. The mass for each plaque varies from 800 to 1200 g. Then the charges were kept warm on a heated conveyor which was 240°C and covered with an insulated tunnel.

At last, the charge was transferred manually into the Dieffenbacher DCP-U 2500/2200 hydraulic press which has a parallel motion control system and a closing force of 5000 kN. The mold was heated up to around 100°C by the oil. The press and the mold used in this work are shown in **Figure 3-8**.

The products used in this work were flat plaques with a size of 457×457×3 mm³. As shown in **Figure 3-9**, the charges were put on one side prior to each compression molding to increase the flow distance during compression molding. This was done because subsequent molding of real automotive parts is expected to require long flow lengths. All the other parameters of the line including conveyor temperature, oil temperature, mold temperature, pressure, speed profile of the press and cooling time were set to be consistent.

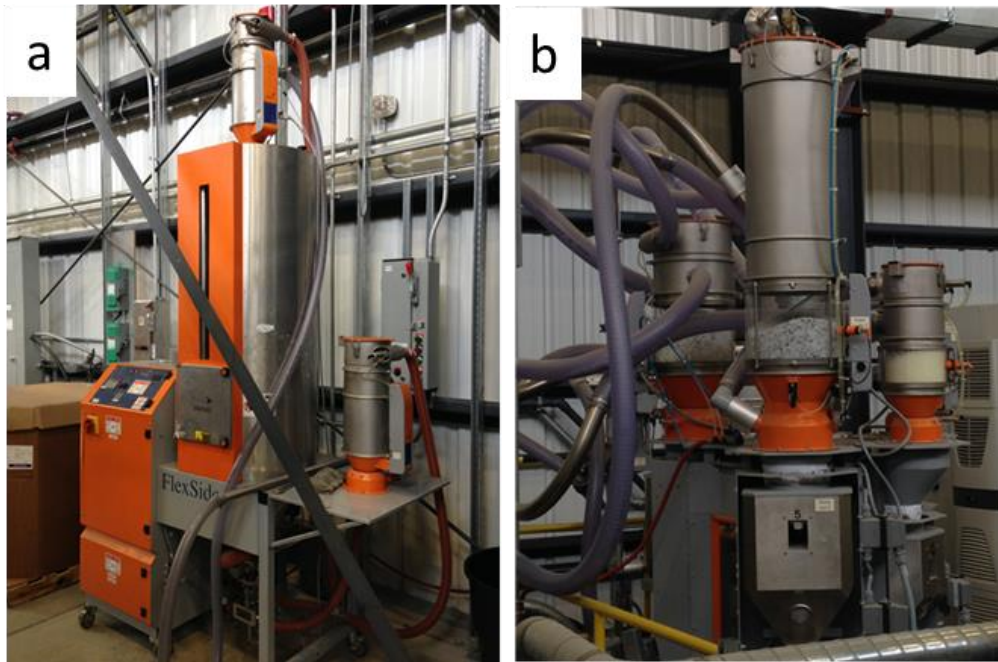


Figure 3-2 a) Polymer dryer and b) gravimetric dosing unit of Dieffenbacher D-LFT-ILC line.



Figure 3-3 The first extruder (ZSE) of Dieffenbacher D-LFT-ILC line.

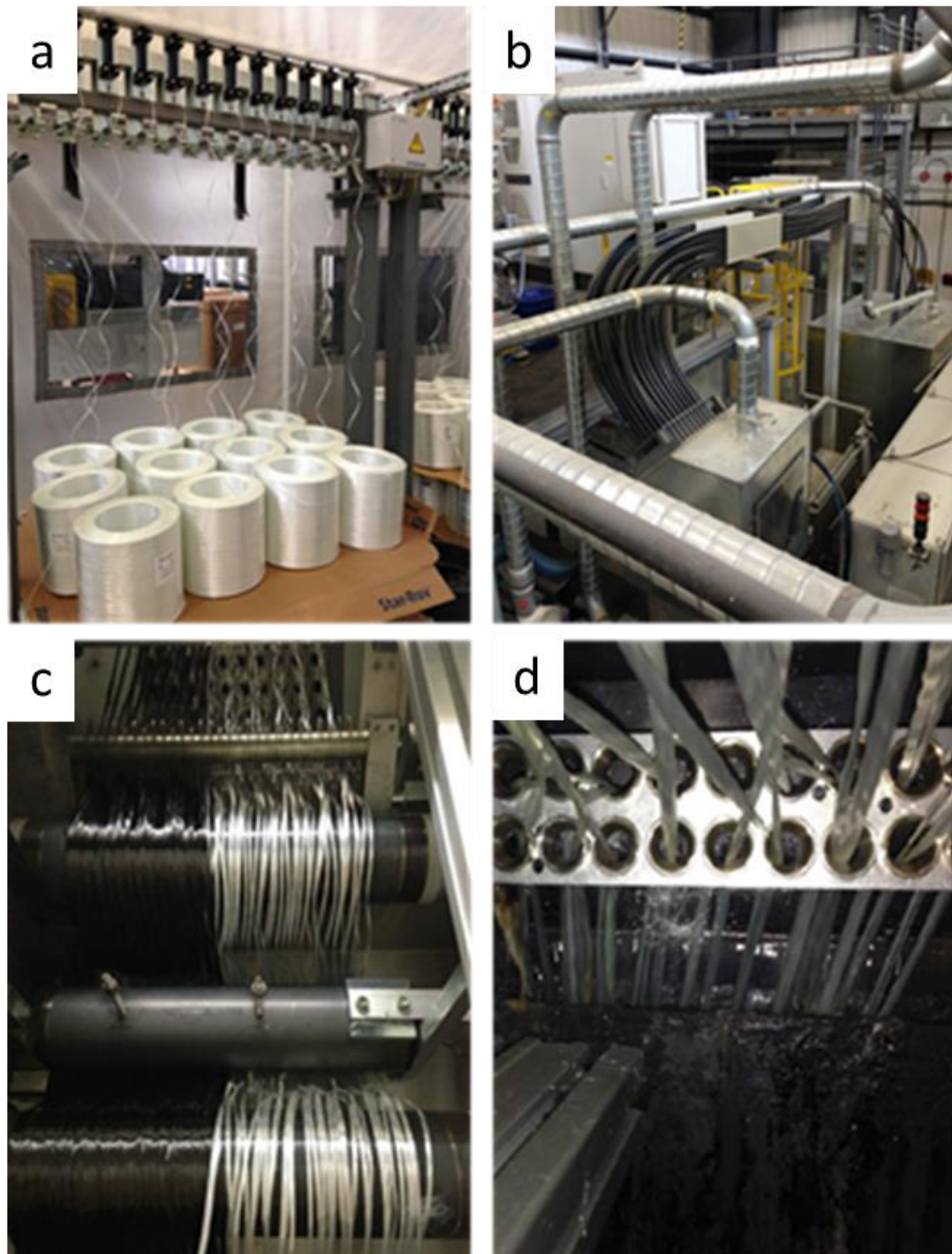


Figure 3-4 Fiber feeding system of Dieffenbacher D-LFT-ILC line with a) continuous glass fiber tows b) plastic tube system c) iron bars for fiber preheating d) roving separation apparatus above the second extruder.



Figure 3-5 The second extruder (ZSG) of Dieffenbacher D-LFT-ILC line.

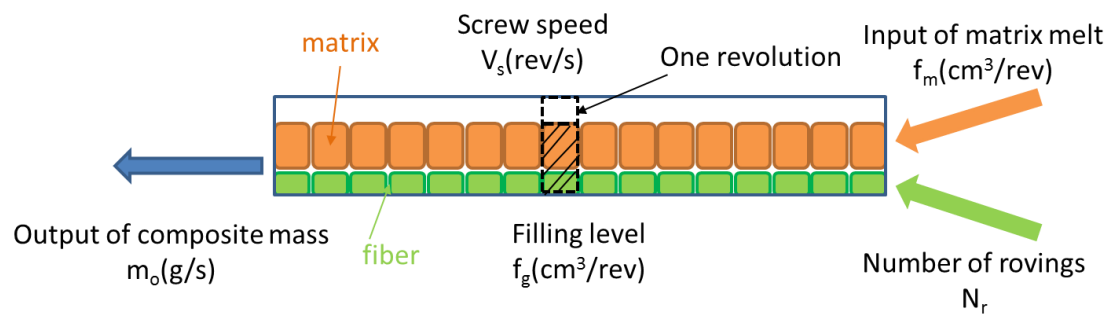


Figure 3-6 Schematic of the second extruder (ZSG) of Dieffenbacher D-LFT-ILC line.

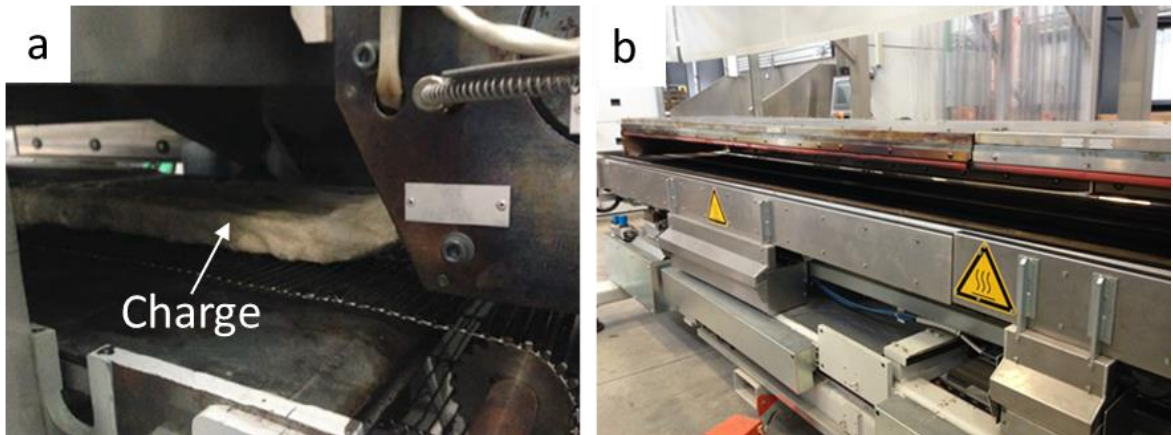


Figure 3-7 Conveyor (PAZ) of Dieffenbacher D-LFT-ILC line with a) composites charge and b) the conveyor.

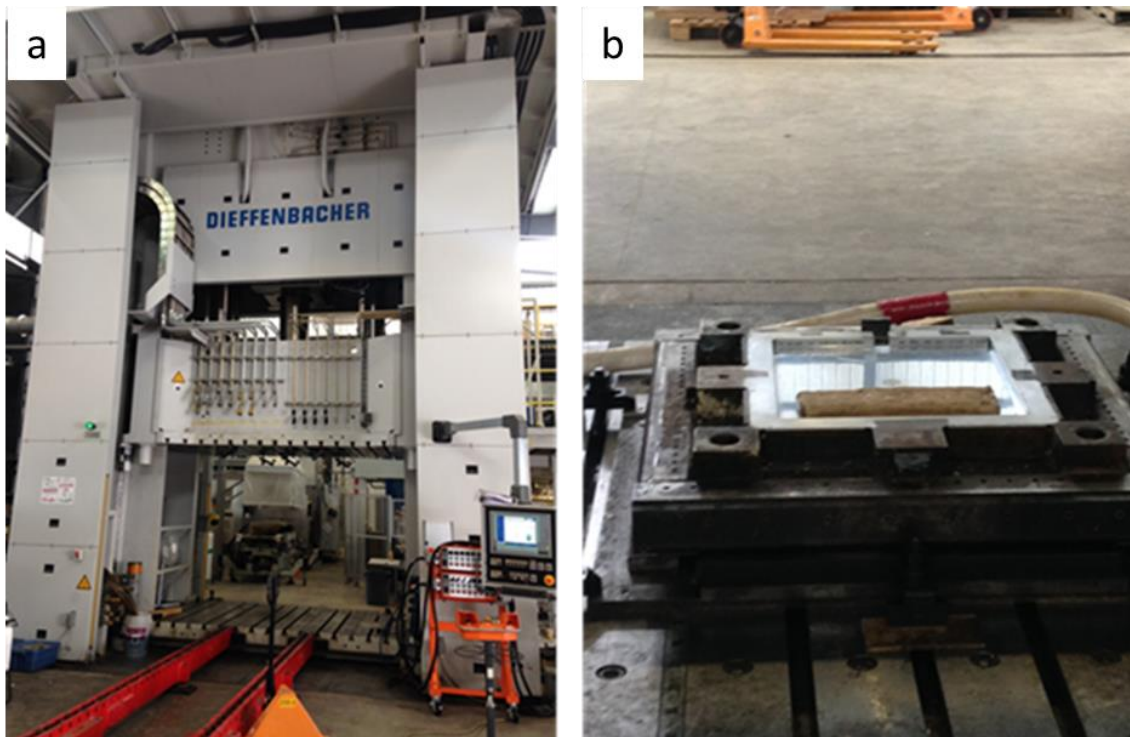


Figure 3-8 Dieffenbacher DCP-U 2500/2200 hydraulic press and b) the compression mold used in this work.

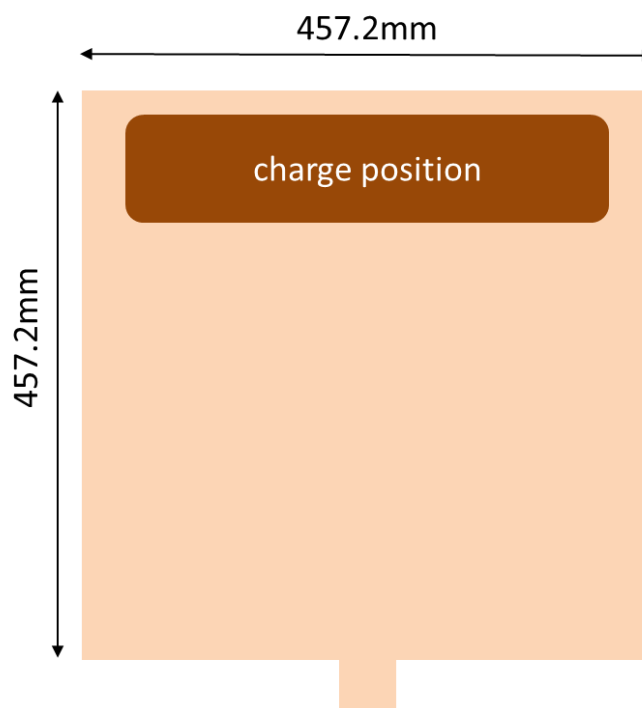


Figure 3-9 Size and charge position of the plaques prepared in this work.

3.2.3 D-LFTs with different processing parameters

With the goal to investigate the effect of parameters related to the compounding process (screw speed, filling level, melt temperature and fiber preheating) on the mechanical properties of this new material, glass fiber/PA6 D-LFT plaques with 30 wt.% were prepared under 8 different conditions (T1, T2, T3, T4, T5, T6, T7, and T8) which are shown in **Table 3-2**. Among these, T1 was the reference condition; T2 and T3 had different screw speeds; T4 and T5 had different filling levels; T6 and T7 had different melt temperatures and T8 had the fibers preheated prior to their incorporation. The room temperature (R.T.) was 23°C.

Based on **Figure 3-6** about the adjustment of fiber content, the adjustment of melt temperature and fiber preheating did not have any effect on the other parameters. When the screw speed of the second extruder increases, that of the first extruder should also increase to keep the fiber content unchanged. The filling level adjustment requires both numbers of rovings and screw speed of the first extruder to change accordingly.

Table 3-2 List of the processing parameters in 8 conditions, room temperature (R.T.) is 23°C.

	Melt Temp. (°C)	Screw Speed (rpm)	Filling level (cm ³ /rev)	Preheating temp. (°C)
T1	280	50	30	R.T.
T2	280	<u>100</u>	30	R.T.
T3	280	<u>25</u>	30	R.T.
T4	280	50	<u>65</u>	R.T.
T5	280	50	<u>10</u>	R.T.
T6	<u>270</u>	50	30	R.T.
T7	<u>290</u>	50	30	R.T.
T8	270	50	30	<u>120</u>

3.2.4 Reinforcing D-LFT with UD tapes

The tailored D-LFT technique was employed to use continuous fiber tapes to reinforce the glass fiber/PA6 D-LFT plaques with a focus on the stacking sequence of the UD tapes. As shown in **Figure 3-10**, the tapes used in this work were provided by BASF, in which the fiber content is 60 wt.% and all the fibers are in the same direction.

Firstly, a Fiberforge Relay@ 1000, as shown in **Figure 3-11**, was employed to fabricate the 3D laminates through trimming, placing and welding the tapes automatically. Then the laminates were heated up to 270°C for 6 min in a HK Präzisionstechnik GmbH hot circulation oven and compressed in the cold mold to achieve consolidation. The products before and after consolidation are shown in **Figure 3-12**. The consolidation can improve the bonding between different laminae and squeeze out the air.

Before co-molding process, the consolidated laminates were preheated again while the PA6 with 30 wt.% glass fiber D-LFT charge was produced through Dieffenbacher D-LFT-ILC line. Finally, the D-LFT charge was put between two pieces of preheated laminates to apply the cold stage press.

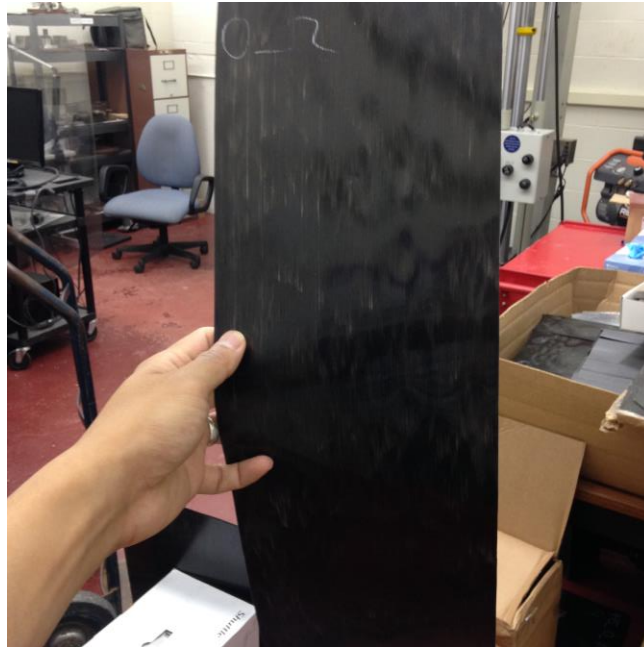


Figure 3-10 Unidirectional continuous fiber tape with 60 wt.% fiber provided by BASF.

The final co-molded material is named as comoulding which has a sandwich structure with two consolidated laminates outside and one D-LFT layer in between. Each laminate has 4 layers of UD lamina in which all the fibers are continuous and aligned in the same direction. With an assumption that the flow direction of the charge is 0° -direction, the UD laminae can be represented by 4 angles (0° , 90° , $+45^\circ$, -45°) between the fibers alignment and 0° -direction. $[0]_8$, $[(0/90)_2]_s$ and $[0/90/+45/-45]_s$ were chosen as the stacking sequences of two outside laminates with unidirectional (UD), orthotropic and quasi-isotropic reinforcing potentials. As a reference, the materials which have the same structure with 3 comouldings but no D-LFT layer were also co-molded and named as layups. Therefore, both the comouldings and the layups are symmetrical, which can avoid significant warpage. For convenience, the pure D-LFT with 30 wt.% fiber is labeled as LFT30. The layups with stacking sequences of UD $[0]_8$, orthotropic $[(0/90)_2]_s$ and quasi-isotropic $[0/90/+45/-45]_s$ are labeled as #1L, #2L and #3L, respectively. The relevant 3 comouldings are labeled as #1C, #2C and #3C, respectively. The detailed structure of layups (#1L, #2L and #3L) and comouldings (#1C, #2C, and #3C) are summarized in **Figure 3-13**.

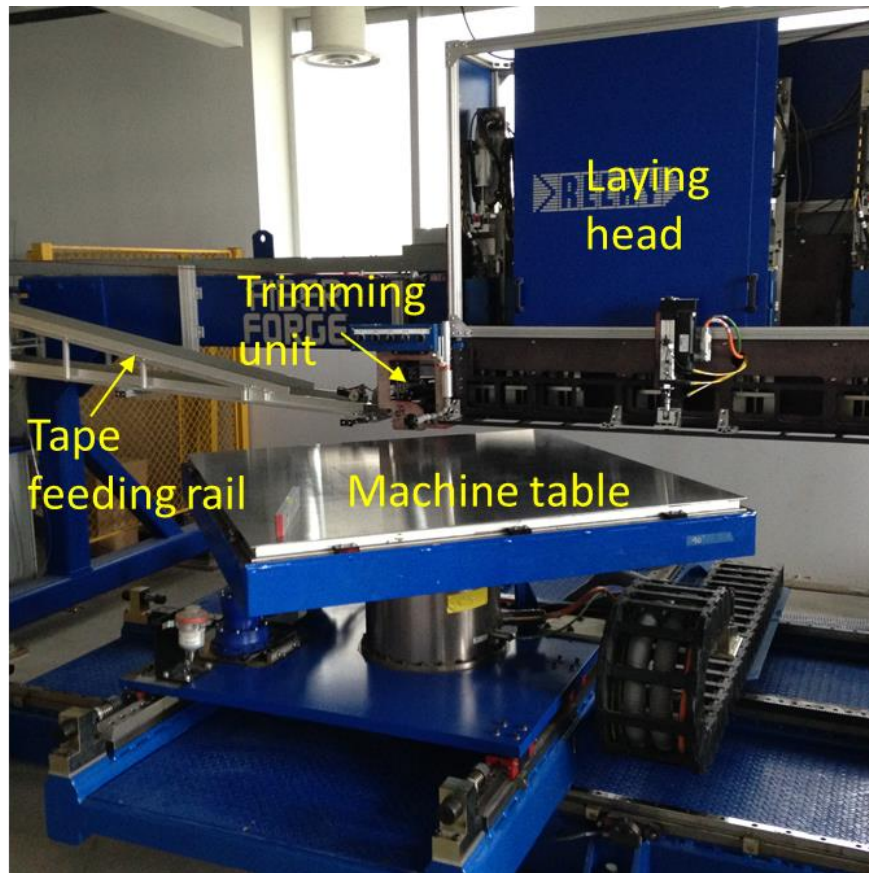


Figure 3-11 Fiberforge Relay@ 1000 at FPC@Western.

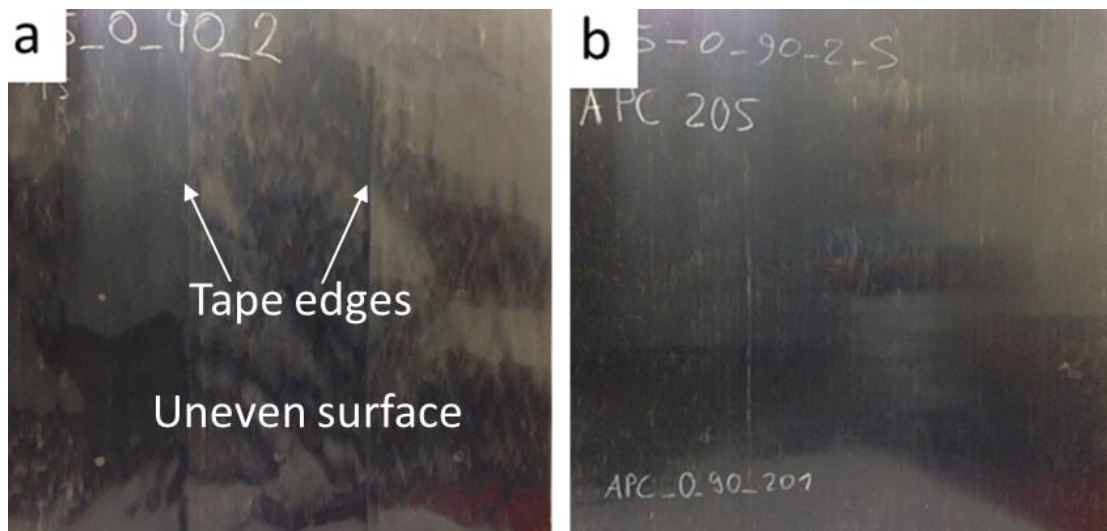


Figure 3-12 Layups with stacking sequence of $[0/90]_s$ a) before consolidation and b) after consolidation.

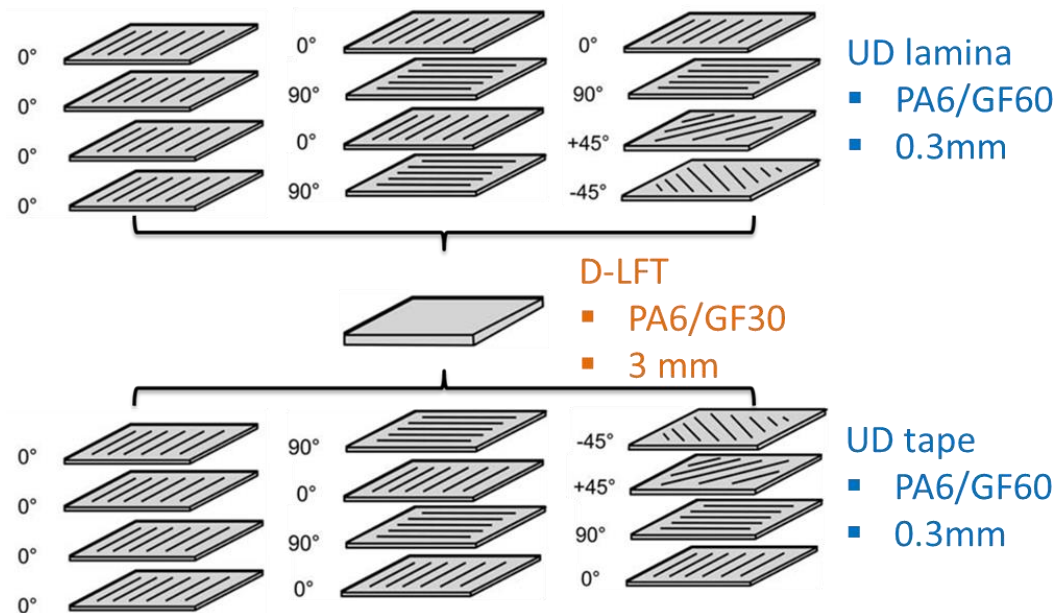


Figure 3-13 Detailed structure of the layups and co-molded products with three types of stacking sequence.

3.3 Methodology

3.3.1 Mechanical testing

All the final products were labeled and stored in the lab in an ambient environment. CNC milling machine was employed to cut the test samples in both flow and cross-flow directions from the plaque based on different layouts. Since the moisture can degrade the mechanical properties of PA6, all the samples were dried in a vacuum assisted oven at 100°C for 48 hours prior to the tests.

3.3.1.1 Tensile test

Quasi-static tensile tests were performed on an Instron 8804 load frame with a 250 kN load cell. The procedure was based on ASTM D638 [121]. The crosshead speed was 2 mm/min. As shown in **Figure 3-14**, an extensometer with a gauge length of 50mm was attached to the specimen to measure the strain. The modulus, strength and strain at failure were determined based on the standard.

Poisson's ratio was measured using a VIC-3D™ digital image correlation (DIC) system, as shown in **Figure 3-15**, to track the strains both in vertical and horizontal directions at the same time. The VIC-3D™ System is a powerful digital image correlation (DIC) system which can measure arbitrary multiaxial displacements and strains from 50 microstrain to 2000% strain and above, for 3D specimen size ranging from 1mm to 10m. The principle of DIC system is measuring the strain through tracking the changes in grey value pattern in small neighborhoods called subsets during deformation. The two cameras equipped give it the capacity to track strains in 3 directions.

Prior to a test, spray paint was used to prepare the region of interest on the specimen with a speckle pattern, which requires to be high-contrast, random and relatively uniform. The accuracy of this system strongly relies on the quality of the speckle pattern. The quality of the pattern can suffer from a rough surface of specimens. The system also needs to be calibrated using a proper grid to determine the necessary variables of the cameras.

3.3.1.2 Bending test

Flexural tests were performed on an Instron 8804 load frame with a 5kN load cell equipped with a 3-point bending apparatus as shown in **Figure 3-16**. The procedure was based on ASTM D790 [122]. It is recommended to use a large span-to-depth ratio of 32:1 for high strength material to ensure the failure is caused by the bending moment. The rate of crosshead, the flexural stress and the flexural strain were calculated by the following equations [122], respectively:

$$R = 0.01L^2/6d \quad (3-1)$$

$$\sigma_f = \left(\frac{3PL}{2bd^2}\right) \left[1 + 6\left(\frac{D}{L}\right)^2 - 4\left(\frac{d}{L}\right)\left(\frac{D}{L}\right)\right] \quad (3-2)$$

$$\varepsilon_f = 6Dd/L^2 \quad (3-3)$$

Where R (mm/min) is the rate of crosshead motion, σ_f is the flexural stress, ε_f is the flexural strain, P (kN) is the load, L (mm) is the span, b (mm) is the width of the

specimens, d (mm) is thickness of the specimens and D (mm) is the deflection of the centerline at the middle of the span.

3.3.1.3 Shear test

Shear tests were performed on an Instron 8804 load frame equipped with an Iosipescu shear fixture and a 5kN load cell. The procedure was based on ASTM D5379 [123]. The rate of crosshead motion was 2 mm/min. The DIC system was also employed to track the shear strain within the area between the two notches. **Figure 3-17** shows the Iosipescu shear fixture and the speckled shear specimens. The region between two notches will go through the post-processing of DIC software to calculate the shear strain.

3.3.1.4 Impact test

Puncture impact tests, based on ISO 6603-2 [124], were performed on Dynatup Instron 9250 HV shock tower with a 22.24kN load cell as shown in **Figure 3-18**. The puncture head with a diameter of 20 mm was lubricated by Finish Line synthetic lubricant prior to each puncture test. The drop height was set to be 1 m, which corresponds to a puncture velocity of 4.4 m/s. The specimens ($60 \times 60 \text{ mm}^2$) were clamped onto a flat steel fixture with a 40 mm-diameter hole in the center.

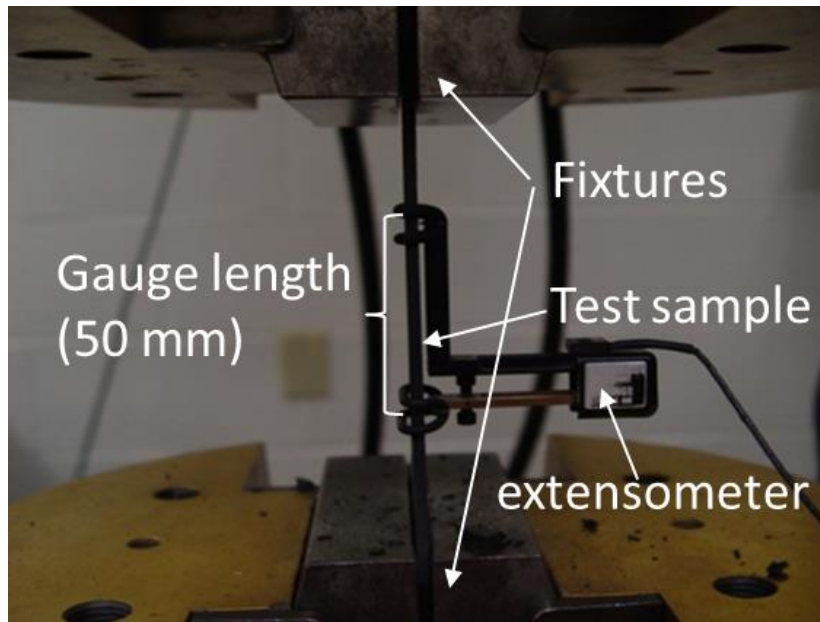


Figure 3-14 Setup of the tensile test with a 50mm extensometer.

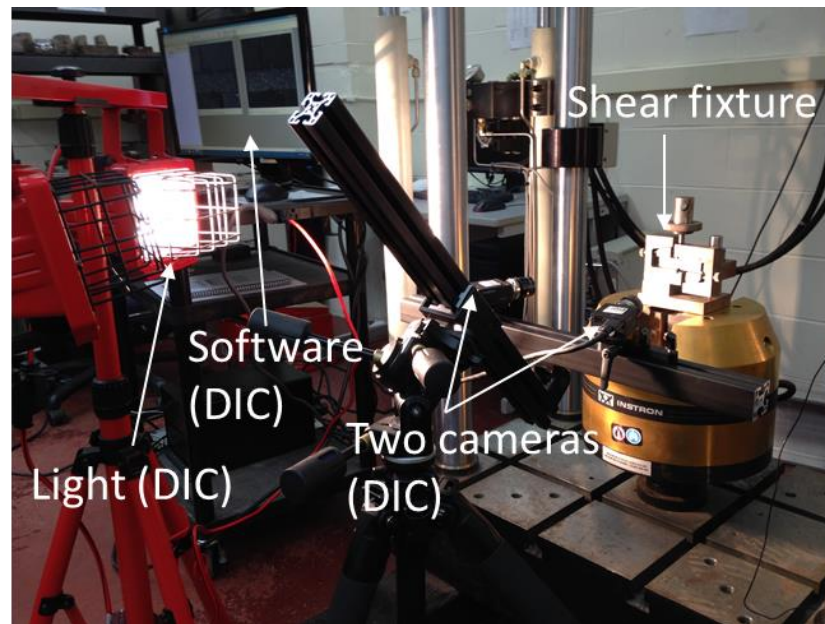


Figure 3-15 Instron 8804 load frame equipped with a VIC-3D™ System.

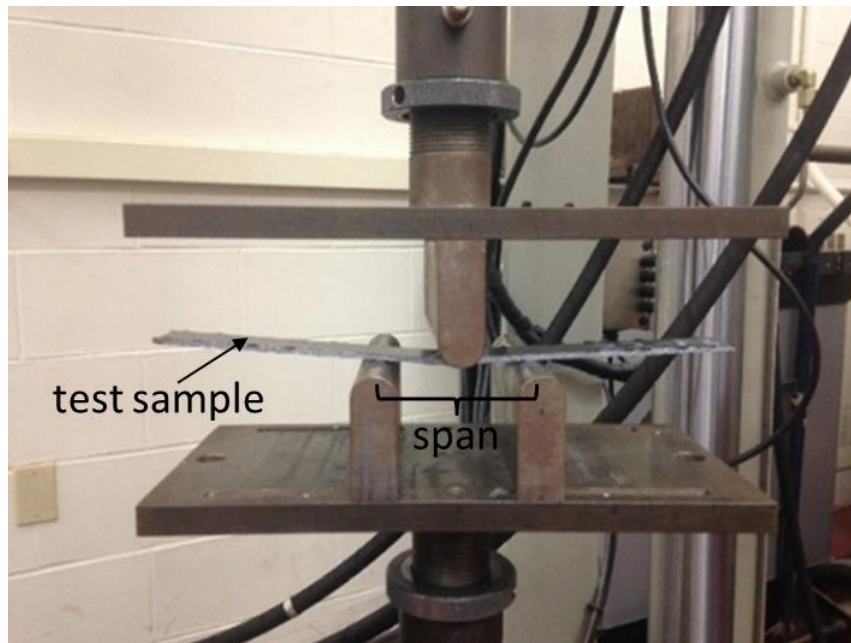


Figure 3-16 3-point bending test apparatus.

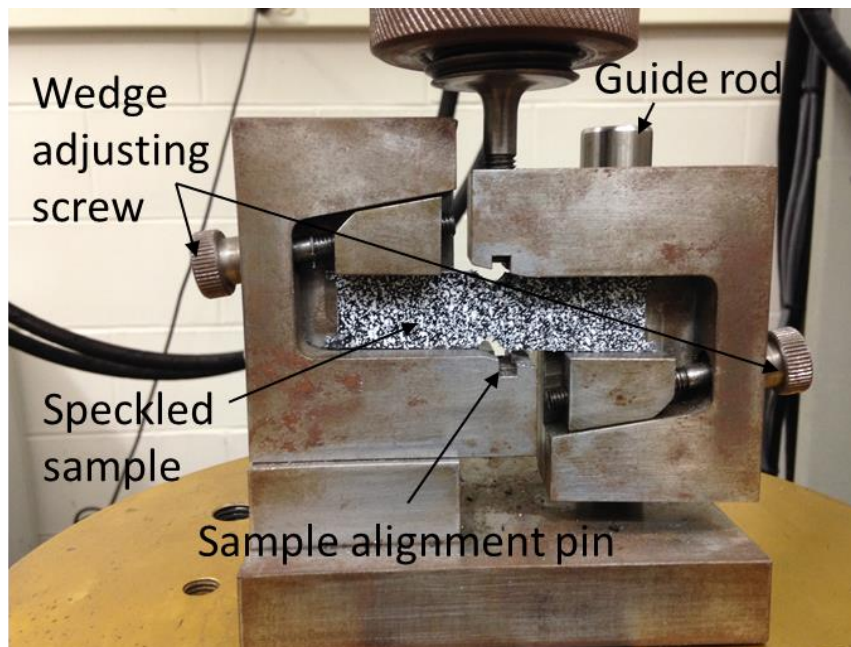


Figure 3-17 A speckled shear specimens fixed in a Iosipescu shear fixture.

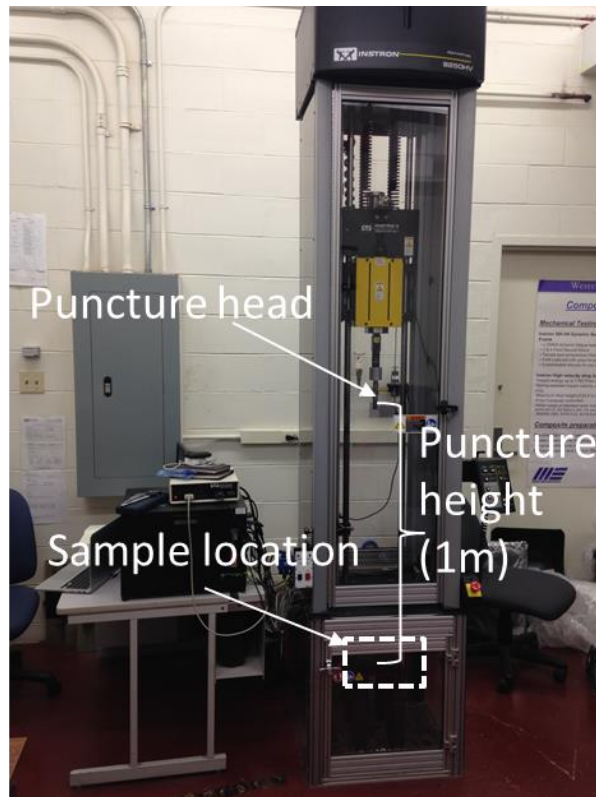


Figure 3-18 Dynatup Instron 9250 HV drop tower.

3.3.1.5 Mechanical test at different temperatures

Tensile and flexural tests at -40°C (with liquid nitrogen), R.T., 85°C and 120°C were performed on an MTS load frame equipped with an environmental chamber as shown in **Figure 3-19**. The temperature range of the chamber is -129°C to 540°C . A video extensometer out of the chamber was set up to track the tensile strain between two grip marks on the specimens through the window. A thermal meter was also used to check the real temperature of the specimens.

3.3.2 Characterization of microstructure

The failure mode analysis of the broken specimens was performed on a Hitachi S-4500 field emission SEM with a Quartz PCI XOne SSD X-ray analyzer. It has the capacity of 2nm spatial resolution at higher electron beam voltages of 15kv and over $100\text{k} \times$ magnification. The specimens were mounted in epoxy. The cross sections of interest

were ground and polished to be observed with a Nikon Eclipse L150 optical microscope. The analysis on the cross sections can be related to the fiber concentration, fiber orientation and voids.

3.3.3 Measurement of fiber volume fraction

The specimens were weighed (m_o) and then placed on a piece of iron film. They were inserted into a tube furnace to be heated up to 600°C. The specimens were ignited and the fire went down after around 1 min. The specimens were kept in the furnace for additional 5 min to make sure all the matrix disappeared. Then the specimens were taken out of the furnace and weighed (m_r) after cooling using a balance at 0.001 gram accuracy. The weight fraction w_f was calculated using the equation below:

$$w_f = \frac{m_r}{m_o} \times 100\% \quad (3-1)$$

3.3.4 Measurement of fiber length distribution

The measurement of fiber length distribution was performed by Sebastian Goris at the University of Wisconsin-Madison. Firstly, square samples with a size of 100mm×100mm were cut from different plaques and burned off to eliminate the matrix. More than 2000 fibers of residual samples were dispersed in water and placed on a flat surface. They were scanned and analyzed by a software with a special algorithm to identify the individual fibers and measure the length. From this data, the fiber length distribution can be calculated.

3.3.5 Measurement of fiber orientation distribution

Fiber orientation distribution measurement used in this work included two steps. At first, the scan of GE eXplore SP "MS" Micro-CT, as shown in **Figure 3-21**, with 6-micrometer resolution was performed on the specimens to get 3D images. The parameters used are X-ray voltage potential of 90 kV and X-ray current of 70 uA. The 3D images were viewed slice by slice through the thickness and transmitted as 2D images of the cross section. In the second step, all the 2D images were analyzed quantitatively by a software called Orientation J to get the fiber orientation distributions through the thickness.

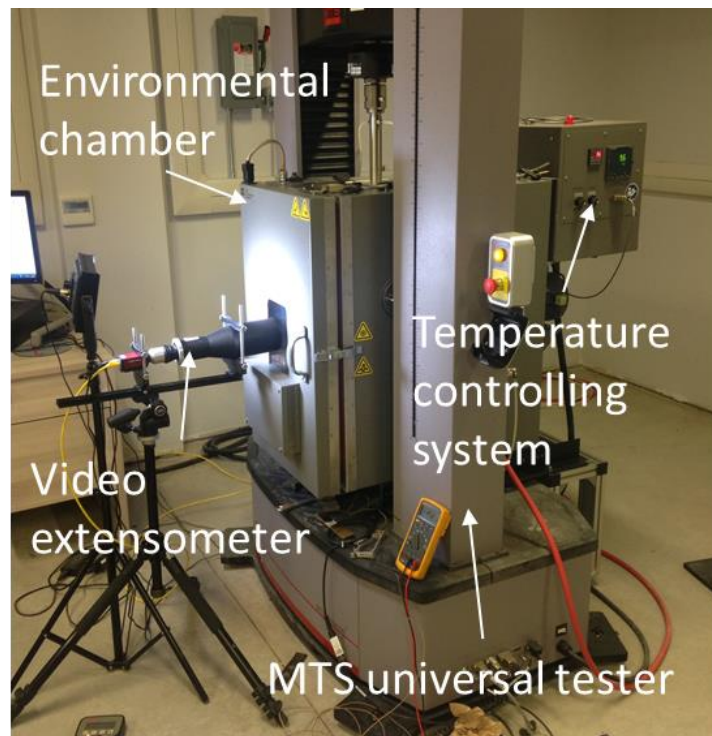


Figure 3-19 MTS load frame equipped with an environmental chamber and a video extensometer.

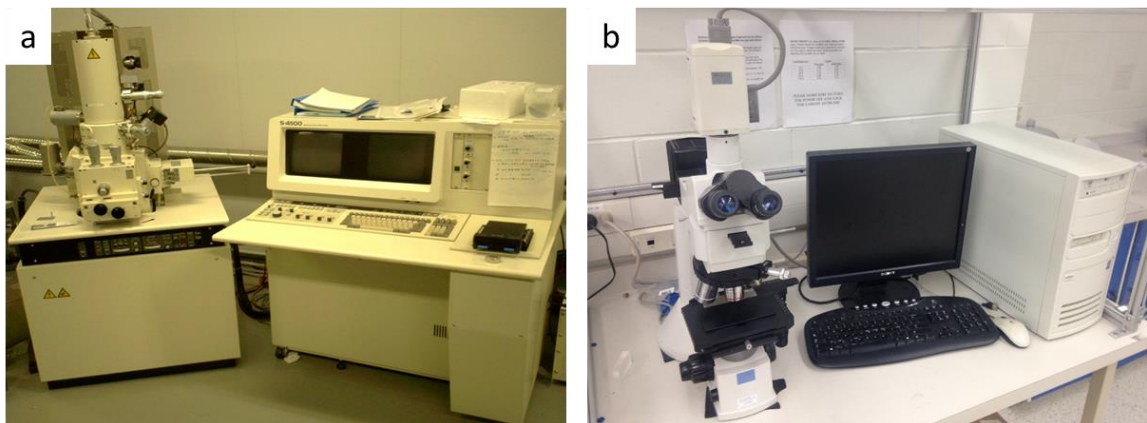


Figure 3-20 a) Hitachi S-4500 field emission SEM and b) Nikon Eclipse L150 microscope.

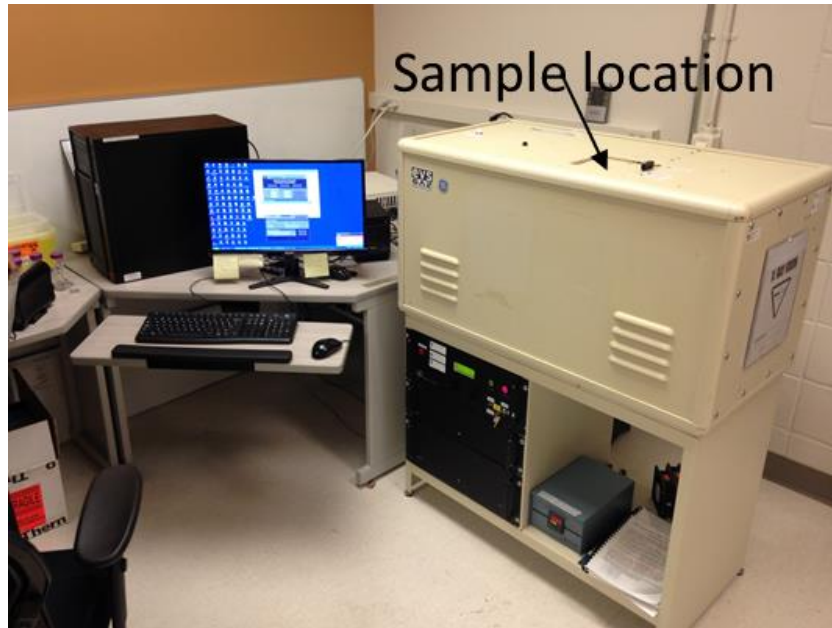


Figure 3-21 GE eXplore SP "MS" micro-CT.

Chapter 4

4 Result and discussion

4.1 Mechanical behavior of D-LFTs with different fiber contents

With the help of FPC@Western, glass fiber/PA6 directly compounded long fiber reinforced thermoplastic (D-LFT) plaques with fiber content of 20, 30, 40, 50, 55 and 60 wt.% were successfully produced. Tensile, flexural, shear and impact tests were all performed on samples cut from those plaques. Firstly, the spatial variation within individual plaque is evaluated to make sure the samples were cut from a relatively homogenous region. Then, the results of mechanical tests are presented and analyzed. With measured fiber length distribution (FLD) and fiber orientation distribution (FOD), the Young's modulus of specimens with 30wt.% fiber is predicted through two existing models and compared with the experimental result. Finally, the verified model is employed to analyze the effect of fiber content on FLD and FOD.

4.1.1 Spatial variations of thickness and fiber content within individual plaque

With the same mold used in this work, all the products were in shape of a flat square plaque with just a little variation of thickness. In this work, samples cut from the same plaque are assumed to have similar properties. Therefore, it was very important to ensure that the samples were cut from a relatively homogeneous region of each plaque. Due to the complex melt flow during compression molding, the fiber distribution within the final D-LFT plaque is expected to be inherently inhomogeneous. Therefore, the spatial variations of thickness and fiber content within individual plaque were evaluated.

Thickness measurements were performed on 81 (9×9) locations within a D-LFT plaque with 30 wt.% fiber. The result is shown in **Figure 4-1**. The thickness is found to decrease both from the charge side to the front side and from right sides to the left side. The difference between the maximum and minimum values is 0.25 mm. With measured cavity size of the mold, the difference of thickness between left and right sides of the

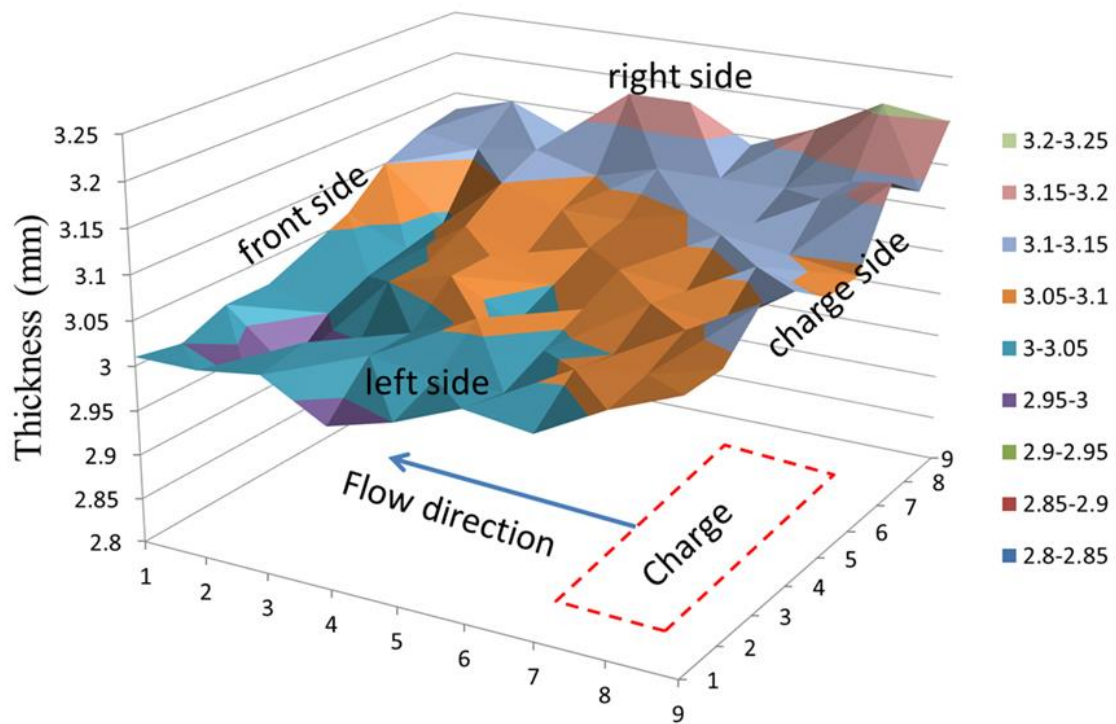


Figure 4-1 Fiber thickness distribution within a D-LFT plaque with 30 wt.% fiber.

plaque can be related to the unbalanced mold size. The cavity of the mold is slightly thinner at charge side than the front side, which might be caused by the inadequate flow during compression molding resulted by the high viscosity of the melt.

Burn-off tests were performed on 25 (5×5) samples cut from the same D-LFT plaque with 30 wt.% fiber. The result of fiber content measurement is shown in **Figure 4-2**. Within the whole plaque, the fiber content is lower around the charge position but higher along the right and left sides. The difference between the maximum and the minimum is 5 wt.%. As even a small variation of fiber content can result in a significant change of mechanical properties, the samples for mechanical tests should be cut away from the charge position and two edges.

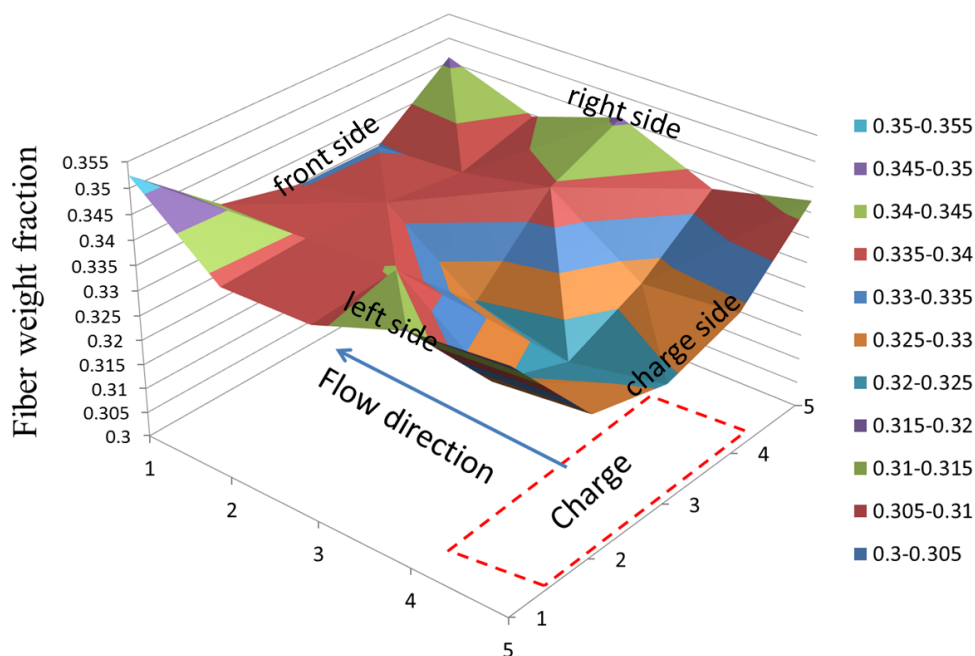


Figure 4-2 Fiber content distribution within a D-LFT plaque with 30 wt.% fiber.

4.1.2 Mechanical testing results

The relationship between moduli and fiber content is summarized in **Figure 4-3**. Both tensile and flexural moduli in 0° -direction and 90° -direction increase as fiber content increases. The increasing rate in 0° -direction is higher than that in 90° -direction. Every 10 wt.% increase of fiber content can raise tensile modulus in 0° -direction by 4-5 GPa and tensile modulus in 90° -direction by 1 GPa. Both tensile and flexural moduli in 0° -direction over the whole range of fiber content are much higher than those in 90° -direction, which indicates the anisotropy of mechanical properties due to the preferred fiber alignment in flow direction. The flexural modulus is found to be lower than the tensile modulus at the same fiber content, which might be related to the inhomogeneous fiber distribution through the thickness.

Tensile and flexural strengths measured on D-LFT specimens with different fiber content are summarized in **Figure 4-4**. Tensile strength in 0° -direction increases from 150 MPa to 250 MPa when fiber content increases from 20 to 50 wt.% and then drops to around

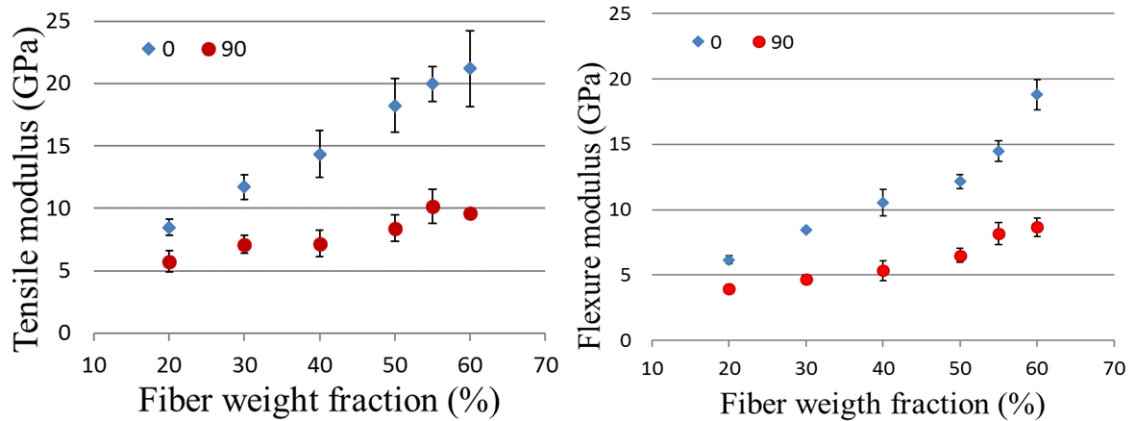


Figure 4-3 Tensile and flexural modulus in both flow and cross-flow directions of glass fiber/PA6 D-LFTs with different fiber contents.

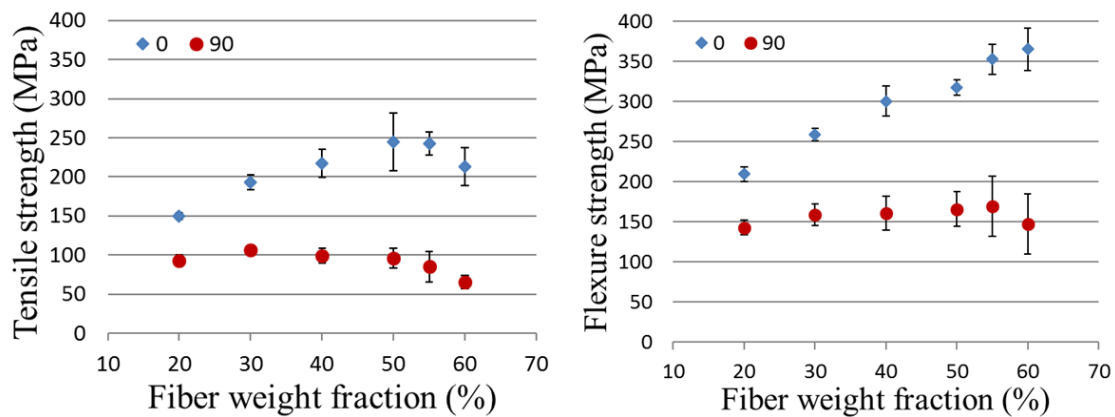


Figure 4-4 Tensile and flexural strength in both flow and cross-flow directions of glass fiber/PA6 D-LFTs with different fiber contents.

210 MPa when fiber content increases further from 50 to 60 wt.%. Tensile strength in 90°-direction increases slightly as fiber content increases from 20 to 30 wt.% and goes down when fiber fraction increase further. However, flexural strength in 0°-direction increases monotonically from 200 MPa to 370 MPa as fiber fraction increases from 20 to 60 wt.% while flexural strength in 90°-direction does not vary a lot over the whole range. Contrary to the finding in moduli, the flexural strength is higher than the tensile strength at the same fiber content.

It is noted that tensile strength decreases with the increase of fiber content when fiber content exceeds 50 wt.%. To derive the cause for that, the tensile failure modes of D-LFT samples with different fiber content were analyzed. As shown in **Figure 4-5**, the fracture surfaces of two tensile D-LFT samples tested in 90°-direction are flat and perpendicular to the load direction which indicates that the preferred fiber alignment in the flow direction makes the crack propagate easily in flow direction. The comparison between two samples tested in 0°-direction with 30 and 50 wt.% fiber shows that the fracture surface of the one with 50 wt.% fiber is more ridged than the one with lower fiber content, which indicates that more delamination occur at higher fiber content.

SEM images taken on the fracture surfaces of tensile D-LFT specimens with 20 and 50 wt.% fiber tested in 0°-direction are shown in **Figure 4-6**. Large amounts of holes in the matrix indicate that the fiber pull out is the major failure mode. The 50 wt.% fiber specimen has much more fiber bundles (wet-out issue) than the 20 wt.% fiber specimen, which might be the cause for the reduction of strength. When the fiber content is very high, there will be more fiber rovings and less matrix in the extruder, making the shear flow hard to disperse all the fibers thoroughly. The fibers that are still twisted together make the inner fibers hard to be impregnated where the voids tend to form and can serve as the crack initiating sites. Lack of fiber impregnation severely degrades the interface and the load transfer between matrix and fiber. The insufficient melt flow caused by high fiber content also tends to reduce the homogeneity of the plaques.

The fracture surface of a tensile D-LFT specimen tested in 90°-direction is shown in **Figure 4-7**. The alignments of most fibers have a large angle with the load direction. Only a few holes appear on the surface, indicating the fiber pull out is not the main failure mode for tensile specimen tested in 90°-direction. Most fiber bundles appear in the core portion of the specimens, which might lead to the different variation trends of tensile strength and flexural strength with increasing fiber content. As being more sensitive to the microstructure of the shell portion, flexure strength can benefit more than tensile strength from the increase of fiber content at high fiber content.

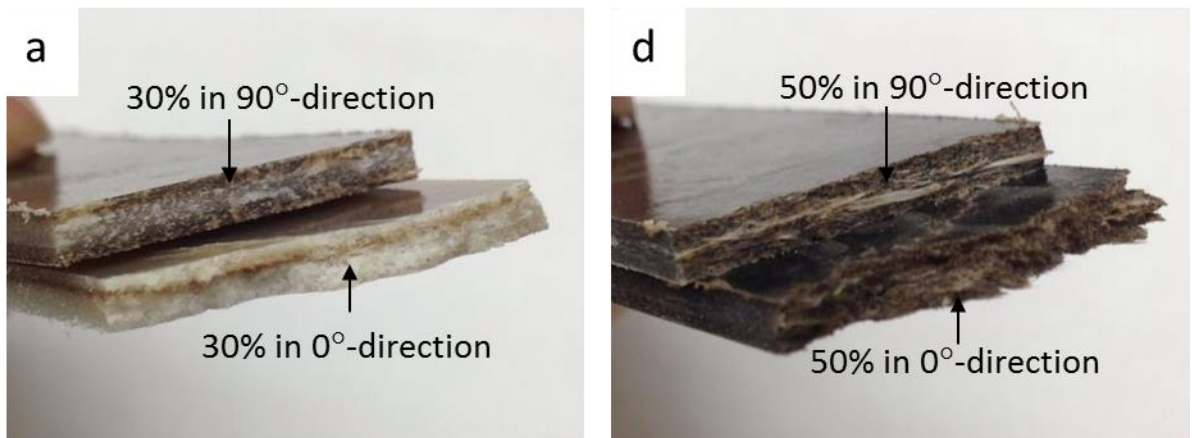


Figure 4-5 Fracture surfaces of tensile specimens tested in 0° and 90° -directions of D-LFT with a) 30 wt.% fiber and b) 50 wt.% fiber.

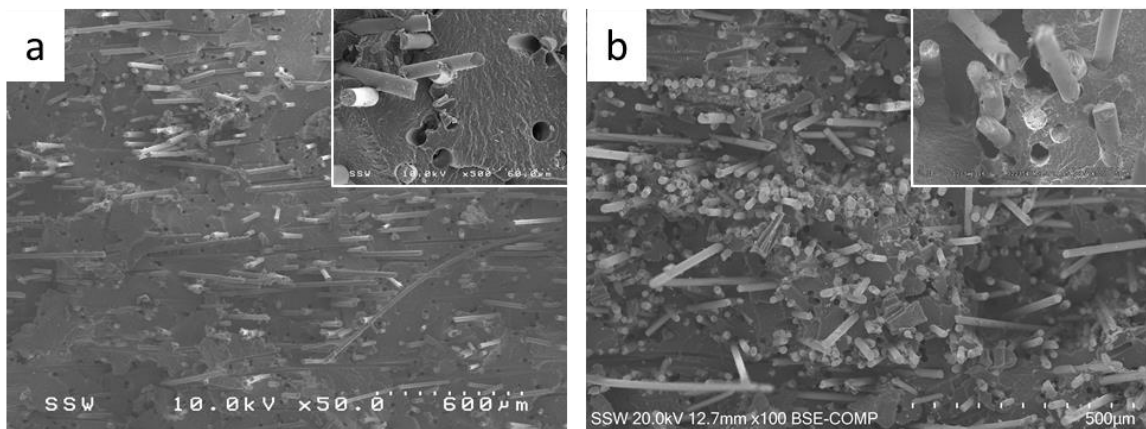


Figure 4-6 SEM images of the fracture surfaces of tensile D-LFT sample with a) 20 wt.% fiber tested in 0° -direction and b) tensile D-LFT sample with 50 wt.% fiber tested in 0° -direction.

The effect of fiber content on strain at failure is summarized in **Figure 4-8**. Tensile strains at failure are around 1-2% while flexural strains at failure range from 2% to 6%. It can be seen the increase of fiber content has negative effect on the flexural strain at failure. In some other related works on LFT [29, 33], the increase of fiber content was also reported to have negative effect on tensile strain at failure. That was related to the increasing amount of fiber ends which can act as the crack initiating sites. But the

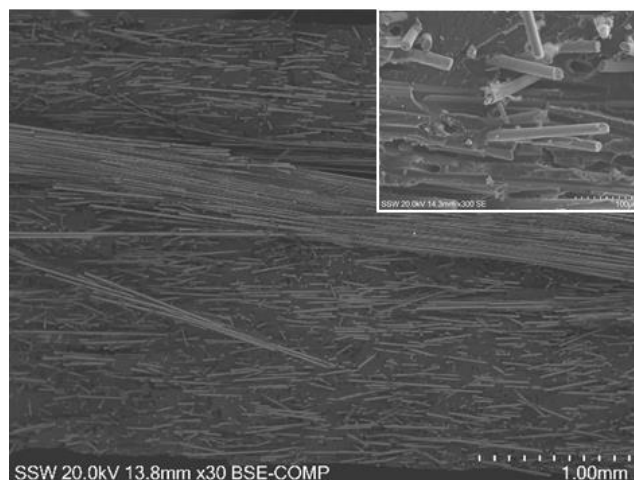


Figure 4-7 SEM image of the fracture surface of a tensile D-LFT specimen with 50 wt.% fiber tested in 90°-direction.

variation trend of tensile strain at failure with increasing fiber content is not obvious due to the big error bar.

The results of shear testing are summarized in **Figure 4-9**. The increase of fiber content improves shear modulus in both 0°-direction and 90°-direction. The shear modulus tested in 0°-direction and 90°-direction are quite close over the whole range of fiber content.

The shear strengths tested in both 0°-direction and 90°-direction build up at the very beginning as fiber fraction increases from 20 to 40 wt.% and then form a plateau as fiber fraction increases further. Poisson's ratios of the D-LFT specimens with different fiber contents were also measured and summarized in **Figure 4-10**. As fiber content increases, the major Poisson's ratio ν_{12} just slightly decreases while ν_{21} is unchanged over the whole range. Based on the rule of mixture (ROM), the major Poisson's ratio of LFT should decrease with the increase of fiber content since the Poisson's ratio of glass fiber (0.17) is smaller than the Poisson's ratio of PA6 (0.45).

As shown in **Figure 4-11**, the impact properties including the peak force, energy to the peak force and total energy increase as the fiber content goes up. But the standard deviation is found to increase for those with higher fiber fraction like 55 wt.% and 60 wt.%.

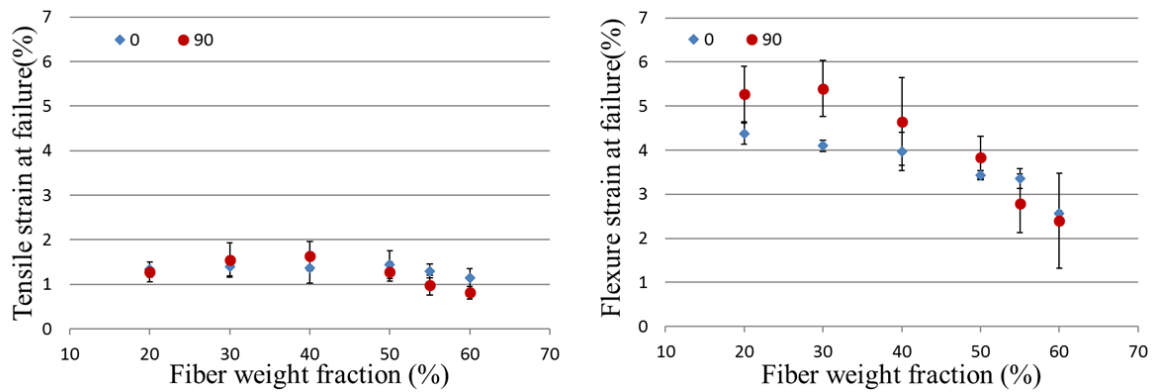


Figure 4-8 Tensile and flexural strain at failure in both flow and cross-flow directions of D-LFTs with different fiber contents.

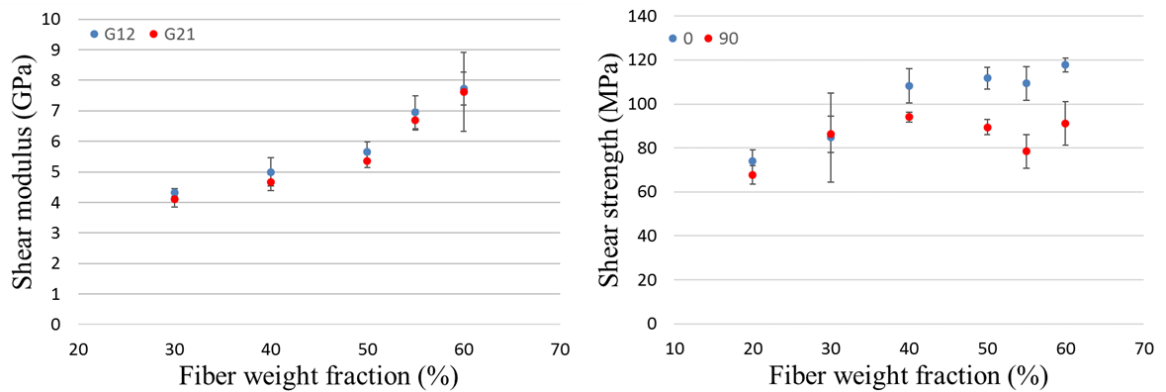


Figure 4-9 Shear modulus and strength in both flow and cross-flow directions of glass fiber/PA6 D-LFTs with different fiber contents.

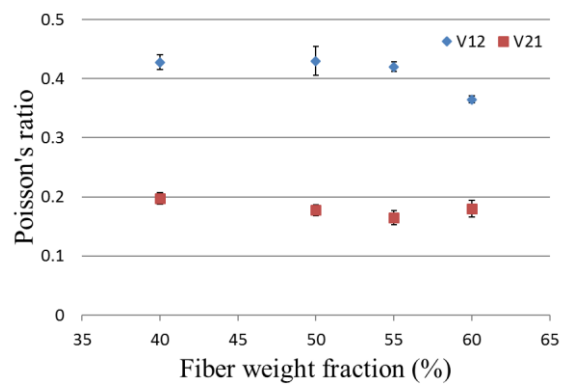


Figure 4-10 Poisson's ratio in both flow and cross-flow directions of glass fiber/PA6 D-LFTs with different fiber contents.

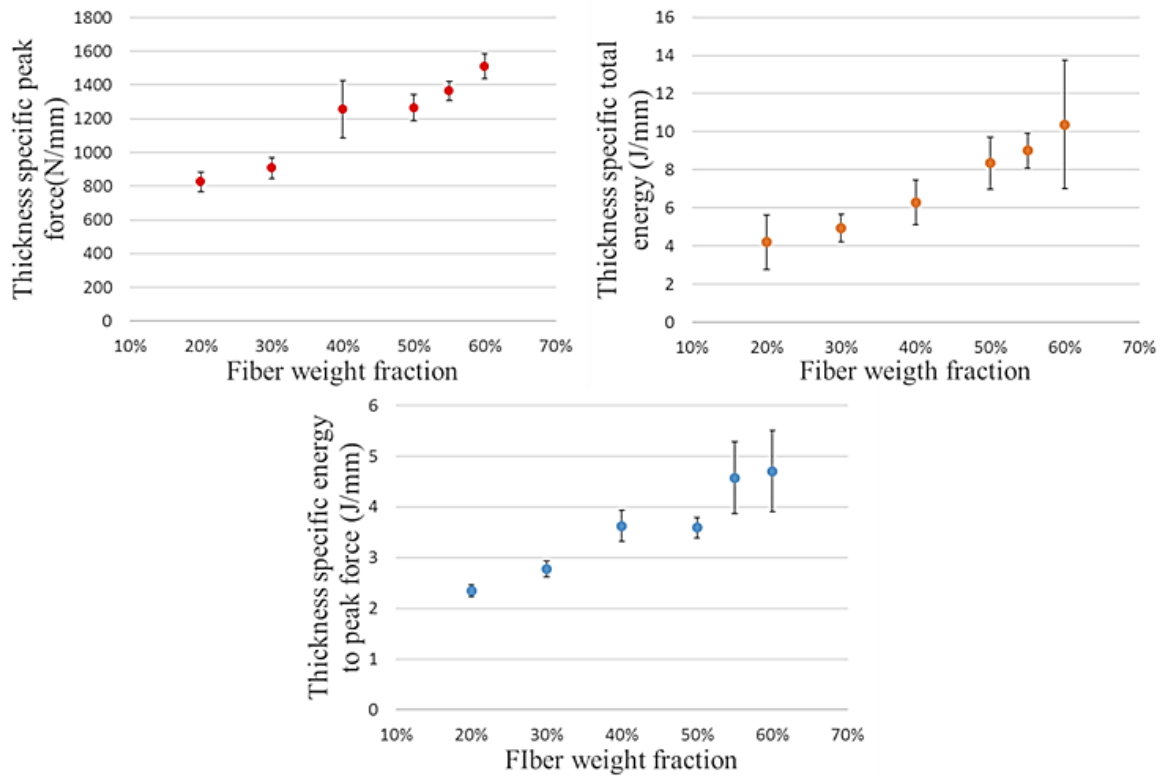


Figure 4-11 Thickness specific impact peak force, impact energy and energy to peak force of D-LFTs with different fiber contents.

The failed impact specimens with different fiber contents are shown in **Figure 4-12**. The size of impact hole of most specimens with 20 wt.% fiber is close to the diameter of the fixture ring instead of the puncture head. Based on ISO 6603 standard, this type of failure usually indicates that the specimens did not yield before the failure. This kind of failure was also observed in failed specimens with 30 and 40 wt.% fiber but not in specimens with 50 wt.% or higher fiber fraction. The impact tests on those with lower fiber fraction tend to break the specimen without yielding followed by an unstable crack growth, while the impact tests on those with higher fiber fraction tend to break the specimen with yielding followed by stable crack growth.

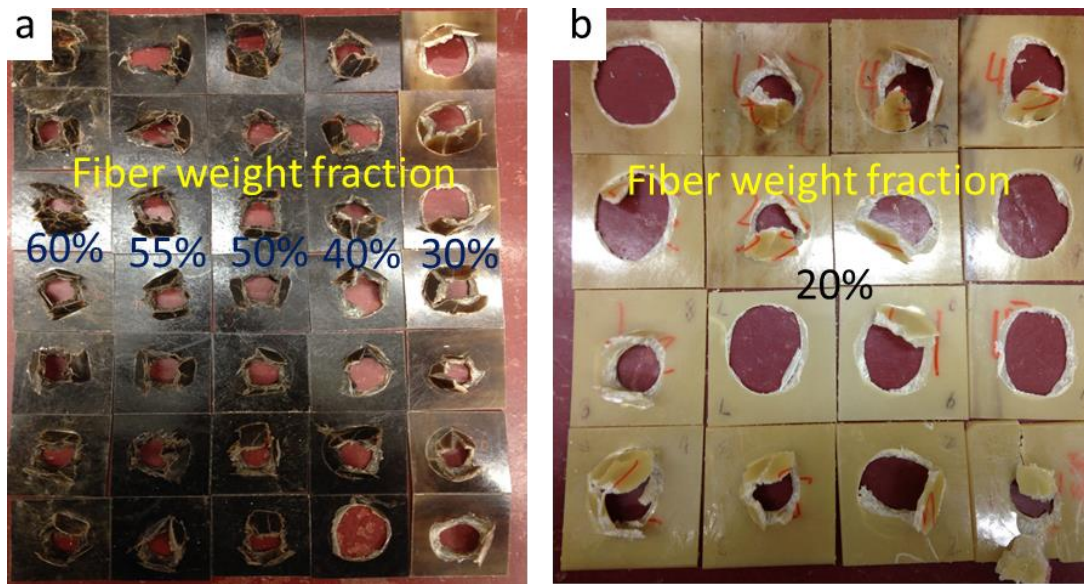


Figure 4-12 Failed impact D-LFT specimens with fiber contents of a) 30-60 wt.% and b) 20 wt.%.

4.1.3 Prediction of Young's modulus of D-LFT

Both the modified rule of mixture (MROM) model and Halpin-Tsai model were employed to predict the Young's modulus in 0° and 90° -directions of D-LFT with 30 wt.% fiber. As mentioned in **Section 2.3**, the prediction of Young's modulus with two models relies on the measurement of fiber length factor k_1 and fiber orientation factor k_2 . The fiber length factors are assumed to be the same for both 0° and 90° -directions, while the fiber orientation factors for two directions should be different.

To measure the fiber orientation factors, a small sample of size $9 \times 3 \times 1 \text{ mm}^3$ was cut from the plaque as show in **Figure 4-13**. The sample was scanned by a micro-CT with a resolution of 6 micrometers. 2D images taken on 9 cross sections of the sample throughout the thickness were extracted from the global 3D image. Images scanned on 9 different layers are shown in **Figure 4-14**, in which white and black regions represent the fibers and the matrix, respectively. Nine images were labeled as #1-#9, respectively, in which #1-3 represent the top shell portion, #4-6 represent the core portion while #7-9 represent the bottom shell portion.

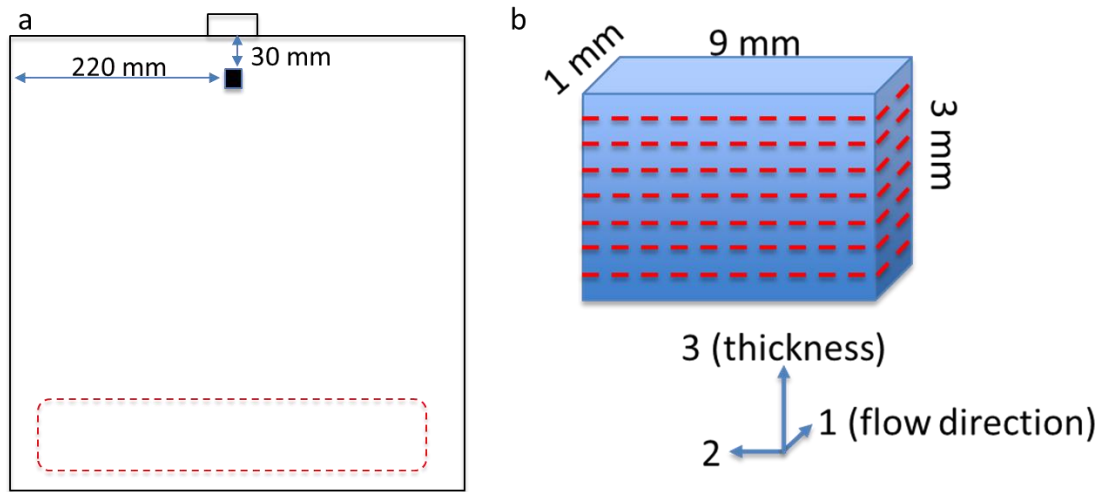


Figure 4-13 a) Position and b) size of the sample cut for micro-CT scan.

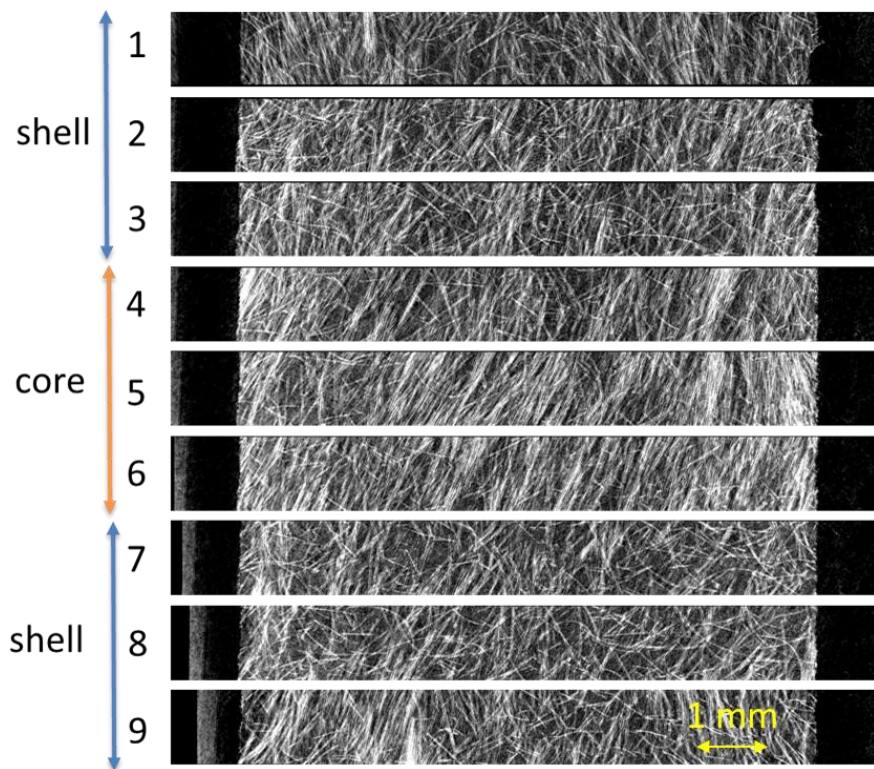


Figure 4-14 Images of cross sections through the thickness of a D-LFT sample by micro-CT scan with resolution of 6 micrometers.

With these 2D images, a software called Orientation J was used to calculate the relevant FOD for each image as shown in **Figure 4-15**. The difference of fiber alignment between shell portion and core portion is not significant. The global FOD function is $a_i = 0.05e^{-0.05\theta_i}$, where a_i is the portion of fibers aligned in θ_i degree. Based on the equation below

$$k_2 = \sum_i a_i \cos^4 \theta_i \quad (4-1)$$

The global fiber orientation factor k_2 was calculated to be 0.754 in 0°-direction and 0.076 in 90°-direction.

The FLD measurement is performed on a 10×10 mm² square sample cut from the same plaque with 30 wt.% fiber. The result is shown in **Figure 4-16**. Based on the expressions shown below

$$L_n = \frac{\sum nl}{\sum n} \quad (4-2)$$

$$L_l = \frac{\sum nl^2}{\sum nl} \quad (4-3)$$

where n represents the number of fibers with a length of l . The numeric average fiber length (L_n) and length weighted average fiber length (L_l) were calculated to be 3.93 mm and 8.77 mm, respectively. Both are much lower than the reported typical value (20-40 mm) for this process with a large amount of short fibers (<300 micrometers) existing. That can be related to the operation of fiber dispersion during the measurement of FLD which is based on the previous work on injection molded LFTs that have shorter fibers than D-LFTs. The serious fiber entanglement existing in D-LFT samples after burn-off tests make it difficult to disperse the fibers without damage. Based on the following equations and L_l of 8.77 mm, the fiber length factor k_1 was calculated to be 0.99.

$$k_1 = \left[1 - \frac{\tanh\left(\frac{\beta L}{2}\right)}{\frac{\beta L}{2}} \right] \quad (4-4)$$

$$\beta = \frac{2}{d} \left[\frac{2G_m}{E_f \ln \sqrt{\frac{\pi}{X_i V_f}}} \right]^{1/2} \quad (4-5)$$

With the measured k_1 of 0.99 and k_1 of 0.754 in 0° -direction and 0.075 in 90° -direction, the Young's modulus in 0° -direction and 90° -direction were predicted by two models and compared with experimental result which are based on at least 5 tests for each. The results are shown in **Figure 4-17**. The predicted E_{11} of 11.04 GPa and 11.43 GPa by two models were only 5% and 9% higher than the experimental E_{11} of 10.50 GPa, respectively. The predicted E_{22} of 3.13 GPa and 4.86 GPa by two models are 46% and 21% lower than the experimental E_{22} of 5.8 GPa, respectively. That means the two models work very well for the prediction of E_{11} whereas underestimate E_{22} . The modified rule of mixture (MROM) is based on the iso-strain model in which the strains of fiber and matrix are assumed to be identical. But that is not the case for D-LFT samples tested in 90° -direction with most fibers aligned perpendicular to the load direction. Considering the enhanced fiber load bearing, the empirical Halpin-Tsai model performs better than MROM model in prediction of E_{22} .

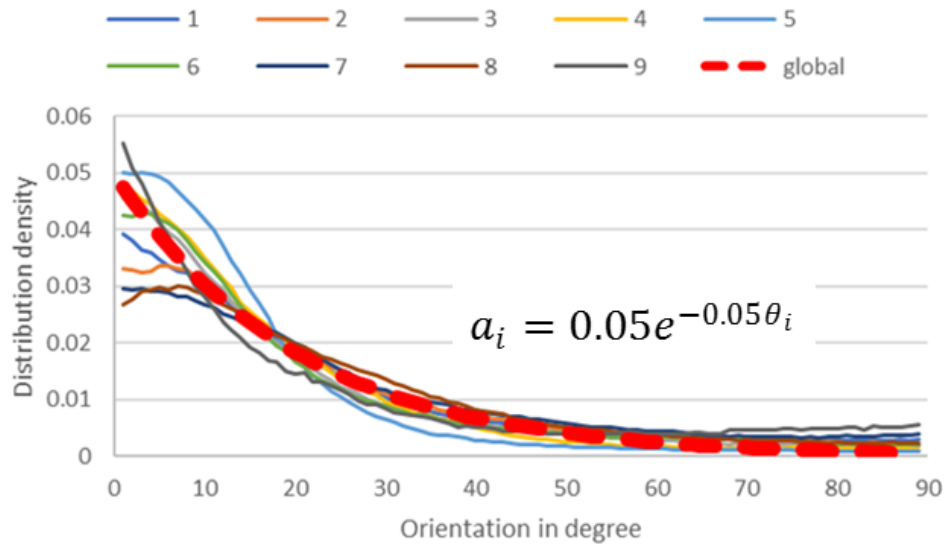


Figure 4-15 Fiber orientation distribution (FOD) measured on 9 layers of a D-LFT sample as shown in **Figure 4-14**.

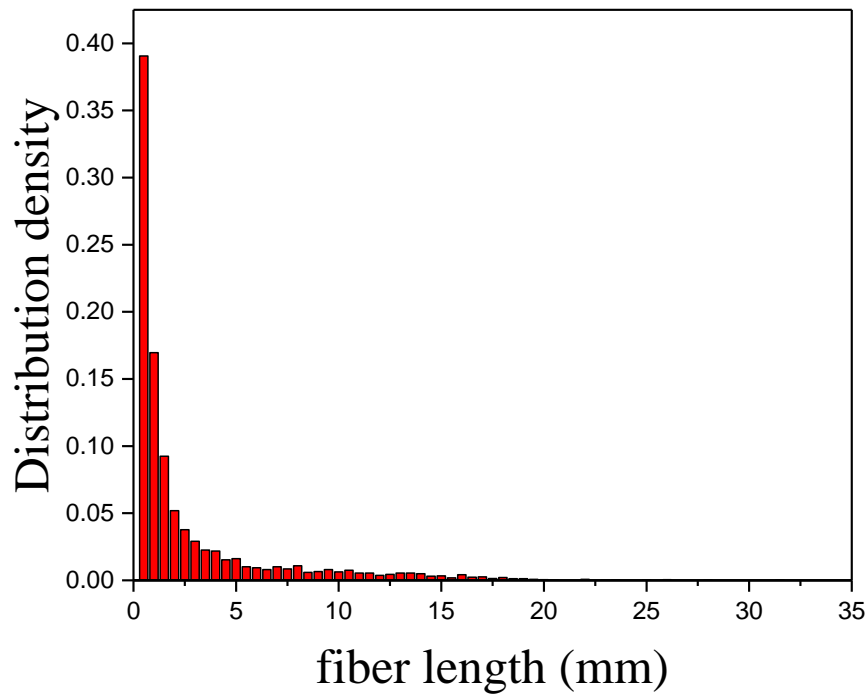


Figure 4-16 Measured fiber length distribution (FLD) of D-LFT with 30 wt.% fiber.

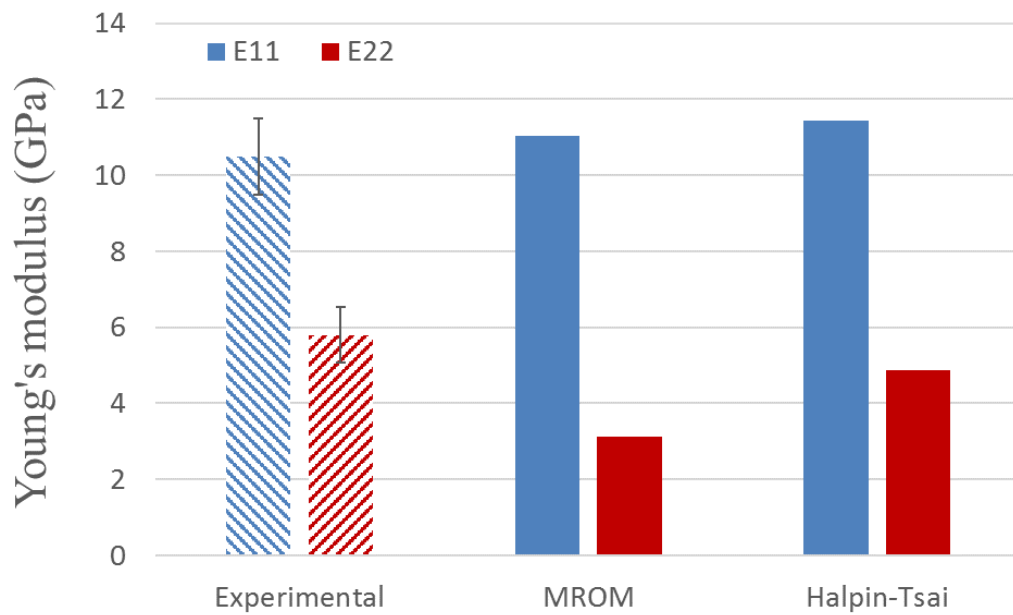


Figure 4-17 Young's moduli in 0° and 90°-directions of D-LFT with 30 wt.% fiber predicted by MROM and Halpin-Tsai models and determined by tensile tests.

4.1.4 Effect of fiber content on fiber length distribution and fiber orientation distribution

Since the MROM model works well for the prediction of E_{11} of D-LFT, it was employed to analyze the effect of fiber content on FLD and FOD. With the tested E_{11} of D-LFTs over the whole range of fiber content and the properties of fiber and matrix materials shown in **Table 3-1**. The value of k_1k_2 for each fiber content is calculated and shown in **Figure 4-18**. The value is found to decrease as fiber content increases, which indicates the increase of fiber content might have negative effect on fiber length and fiber alignment.

The effect of fiber length on Young's modulus was examined at first. The relationship between the fiber length factor k_1 of glass fiber/PA6 D-LFT and fiber length is shown in **Figure 4-19**. The increase of fiber length can improve Young's modulus with the improvement more efficient when the fibers are shorter than 1mm. When fiber length is higher than 1mm, the increase of fiber length contributes less to the Young's modulus. With the measured average fiber length of 8.77 mm, the fiber length factor k_1 was calculated to be 0.99. Considering the potential damage caused by fiber dispersion during the measurement of fiber length and the typical fiber length of at least 10 mm of D-LFTs produced in this line, the real average fiber length can be expected to be much higher than 8.77 mm. Therefore, as shown in **Figure 4-19**, the variation of fiber length in this range will not have significant effect on fiber length factor. The variation of k_1k_2 is more likely due to the decrease of k_2 , which indicates there are few fibers aligned in the flow direction as fiber content increases. The reason might be that more fiber-fiber interactions or higher viscosity of the melt at higher fiber content restrict the fibers to be aligned along the melt flow.

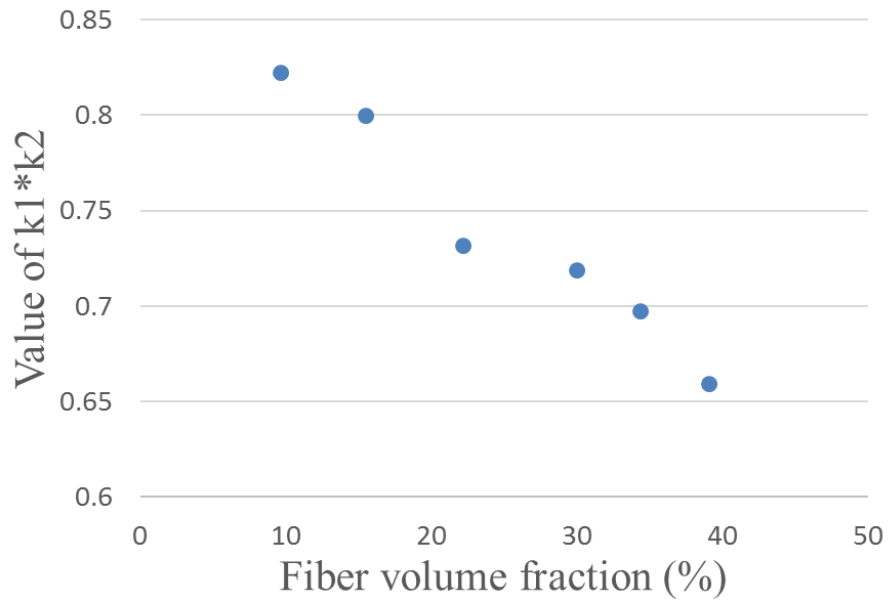


Figure 4-18 Relationship between value of $k_1 k_2$ and different fiber content which is measured with tested E_{11} , known material properties and fiber volume fraction through MROM model.

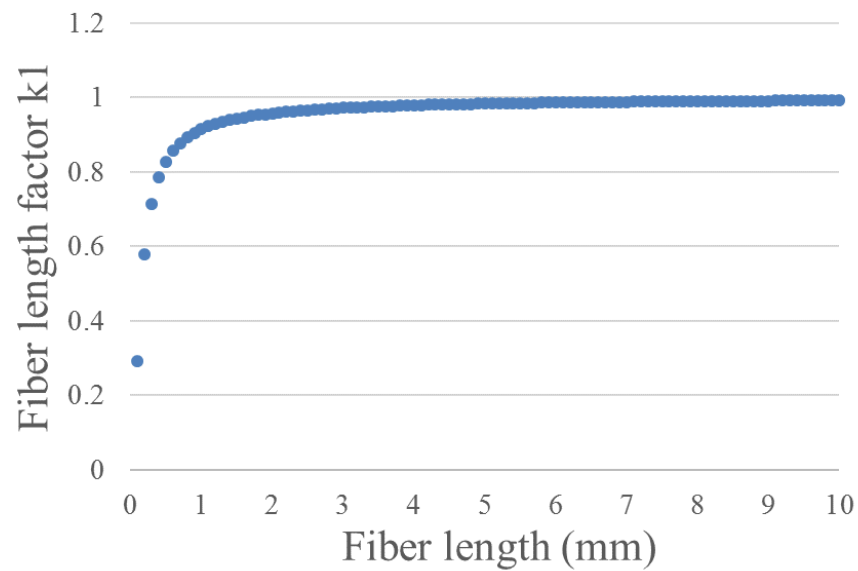


Figure 4-19 Fiber length factor k_1 calculated with different fiber length based on shear lag model.

4.2 Effect of the processing parameters on the mechanical properties of glass fiber/PA6 D-LFTs

In this section, glass fiber/PA6 D-LFT plaques with 30 wt.% fiber were prepared with 8 different conditions to evaluate the effect of melt temperature (T2 & T3), screw speed (T4 & T5), filling level (T6 & T7) and fiber preheating (T8) on the resulting mechanical properties. Around 15 plaques were produced for each condition, in which the first 5 plaques were excluded to avoid the fluctuation right after the adjustment of parameters. Tensile, flexural and impact properties of the plaques were compared and analyzed. Fiber length and fiber content of the plaques were also measured to build the relationship between the variation of mechanical properties and different processing parameters.

4.2.1 Tested mechanical properties

Tensile modulus and strength of D-LFTs prepared with different processing parameters are shown in **Figure 4-20**. Filling level (T4 and T5) is found to influence the Young's modulus both in 0°-direction and 90°-direction. Young's modulus in 0°-direction (E_{11}) is around 10 GPa for T4 with the highest filling level of 65 cm³/rev, 11 GPa for T1 with standard filling level of 30 cm³/rev and 12 GPa for T5 with the lowest filling level of 10 cm³/rev. Even the mean value of E_{11} of T7 with the highest melting temperature of 290°C is higher than that of T6 with the lowest melting temperature of 270°C, the large error bars make it difficult to derive a strong correlation between Young's modulus and melting temperature. It is also noticed that fiber preheating has a negative effect on both Young's modulus and tensile strength of the final products. All the other factors have very limited influences on the tensile strength.

The tested flexural modulus and strength are shown in **Figure 4-21**. The variation trend of flexural modulus is similar with that of tensile modulus. Filling level and fiber preheating are the only two factors that have notable effects on the mechanical properties. Increasing filling level from 10 cm³/rev to 60 cm³/rev leads to a 1.5 GPa reduction of flexural modulus while the fiber preheating also reduces the flexural modulus by around 0.5 GPa.

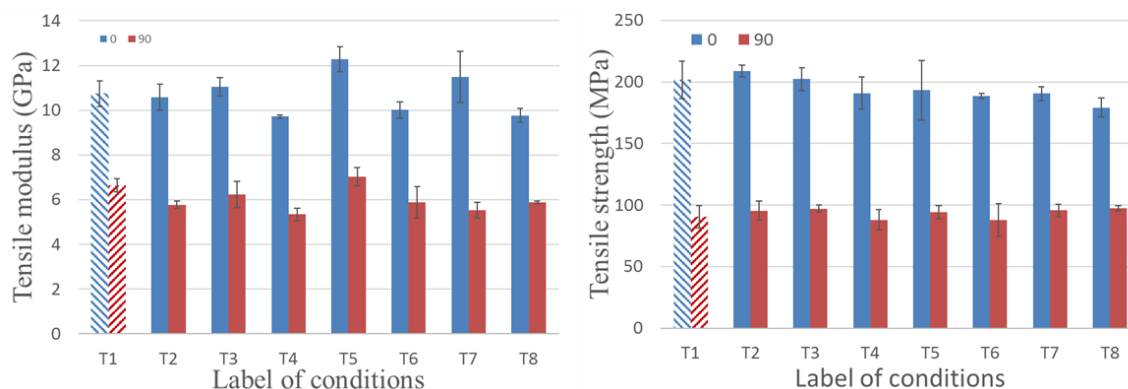


Figure 4-20 Tensile modulus and strength in both 0°-direction and 90°-direction of glass fiber/PA6 D-LFTs specimens prepared in different processing parameters (T1: standard condition; T2&T3: lower and higher screw speed; T4&T5: higher and lower filling level; T6&T7: lower and higher melt temperature; T8: fiber preheating).

The effects of all processing factors on flexure strength are very limited, which is similar as the case of tensile strength.

The tested result of impact strength is summarized in **Figure 4-22**. The mean values of impact strength of T3 and T8 are slightly higher than the rest in 0°-direction and slightly lower than the rest in 90°-direction. That might be because the anisotropy of T3 and T8 are higher than the rest. The variation of screw speed and fiber preheating might influence the final fiber orientation distribution. Due to the big standard deviation and overlap, it is hard to derive strong correlations between the impact properties and any of the examined processing parameters.

Initially, all these processing factors were expected to influence the mechanical properties to some extent, since the compounding process dominated by these factors is the key to determining the fiber length and mixing quality. Based on tested result shown above, Young's modulus and flexural modulus were found to be affected by filling level and fiber preheating, while the tensile strength, flexural strength, and impact properties were not sensitive to the variation of examined parameters.

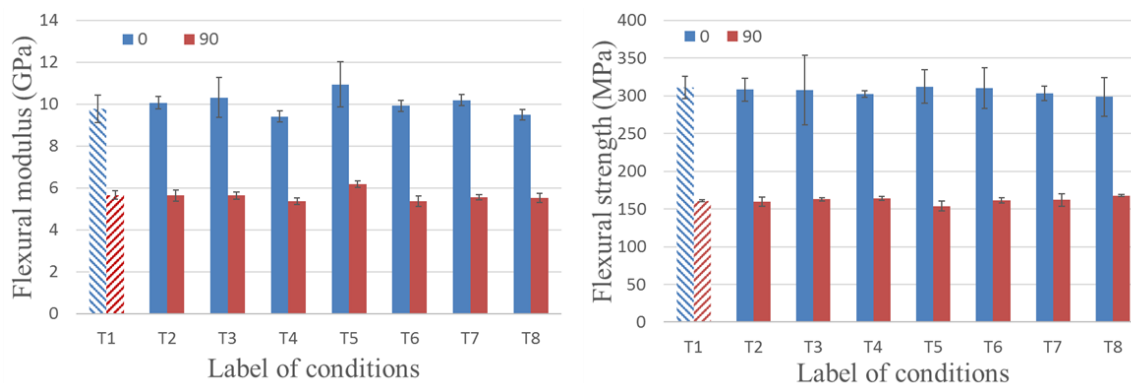


Figure 4-21 Flexural modulus and strength in both 0°-direction and 90°-direction of glass fiber/PA6 D-LFTs specimens prepared with different processing parameters (T1: standard condition; T2&T3: lower and higher screw speed; T4&T5: higher and lower filling level; T6&T7: lower and higher melt temperature; T8: fiber preheating).

4.2.2 Variation of fiber length

To investigate the correlation between Young's modulus and fiber content, the FLD of T4 and T5 were measured. Both the numerical average fiber length (L_n) and length weighted average fiber length (L_l) are summarized in **Figure 4-23**. L_n and L_l are 2.5 mm and 8.4 mm for T4 while are 1.5 mm and 5.8 mm for T5, respectively. The noticeable difference of L_n compared to L_l might be attributed to that a large amount of short fibers (shorter than 0.5 mm) exist in the samples, which may be caused by the fiber dispersing process during the FLD measurement. The large amount of fiber entanglements existing in the residual samples after burn-off made it difficult to disperse the fibers without damage. L_l is more widely used than L_n to perform the quantitative analysis.

The result of FLD shows that T4 with higher filling level has longer fibers than T5 with lower filling level. That is because the higher filling level often result in lower shear effect in the extruder. However, T4 with longer fibers is expected to have higher Young's modulus, which is contrary to the experimental result. Based on the equations (4-2) and (4-3), the fiber length factors k_2 for average fiber length of 8.4mm and 5.8 mm are calculated to be 0.99 and 0.98, respectively, which indicates the fibers for both high

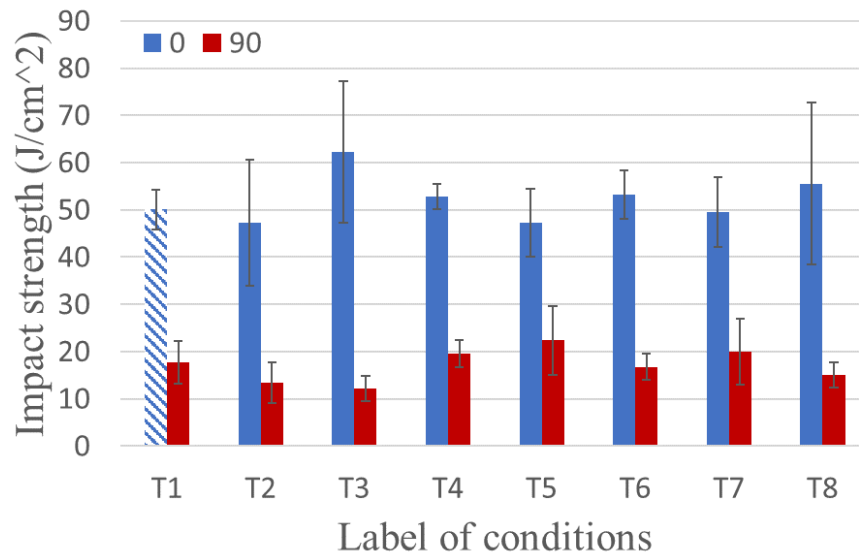


Figure 4-22 Unnotched impact properties in both 0°-direction and 90°-direction of D-LFTs prepared in different processing parameters (T1: standard condition; T2&T3: lower and higher screw speed; T4&T5: higher and lower filling level; T6&T7: lower and higher melt temperature; T8: fiber preheating).

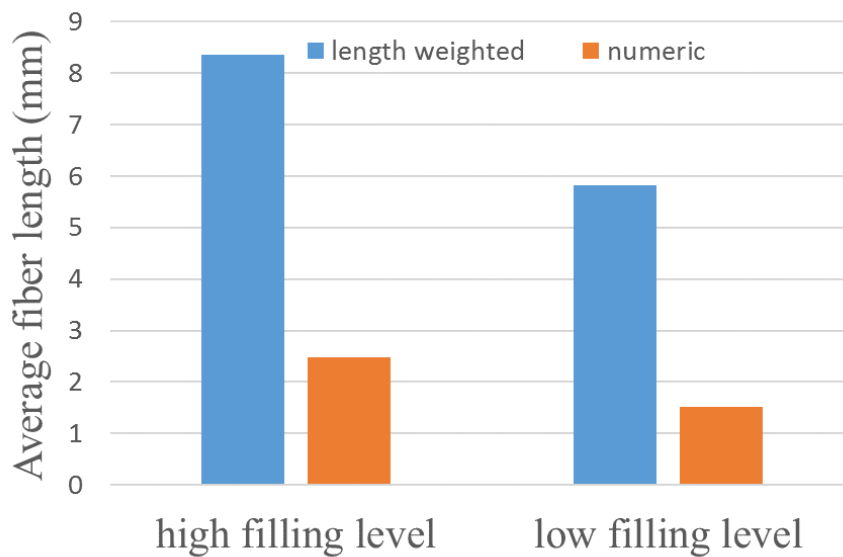


Figure 4-23 Length weighted and numerical average fiber length measured on T4 (the highest filling level) and T5 (the lowest filling level) plaques.

filling level and low filling level are long enough for maximum E_{11} . As shown in **Figure 4-24**, the variation of fiber length at this high level will not affect E_{11} much and cannot be used as a sufficient reason to explain the change of Young's modulus.

4.2.3 Variation of fiber content

The result of fiber content measurement on D-LFT plaques manufactured with different processing parameters is shown in **Figure 4-25**. T4, T5, and T8 have the fiber content of 29, 37 and 29 wt.% respectively, which are different from the rest of around 32 wt.%. The variation trend of the fiber content is similar with that of Young's modulus. Since the plaque tested is the second plaque out of 10 produced in the same condition, it might be possible for the early produced ones to have some fluctuation right after the adjustment of the parameters. To eliminate this possible effect, a double check of fiber fraction was performed on the 9th one out of 10 plaques in T1, T4, and T5. The result is shown in **Figure 4-26**. No difference is found between two tests for T1 which are both close to 32 wt.%. The fiber content of T4 and T5 drops by around 1% and 2%, respectively. But T5 still has higher fiber content than T4.

Based on the analysis, the variation of Young's modulus with different filling level and fiber preheating can be caused by the unexpected variation of fiber content. The fiber content was set to be 30 wt.% for all 8 conditions. The variation may be related to the improper adjustment of filling level during which both feeding rate of matrix and number of fiber rovings need to be accurately adjusted to keep the fiber content stable.

The varied filling level was found to affect the fiber length, which, however, has very limited effect on the mechanical properties. The reason for that may be the fibers in D-LFT are long enough (>10mm) to fully take the mechanical potential of fibers. The mechanical properties of D-LFT are not sensitive to the fiber length variation at this high level. Therefore, once the consistent fiber content is maintained, the mechanical properties of D-LFT plaques are unaffected by the examined processing parameters including melt temperature, screw speed, filling level and fiber preheating.

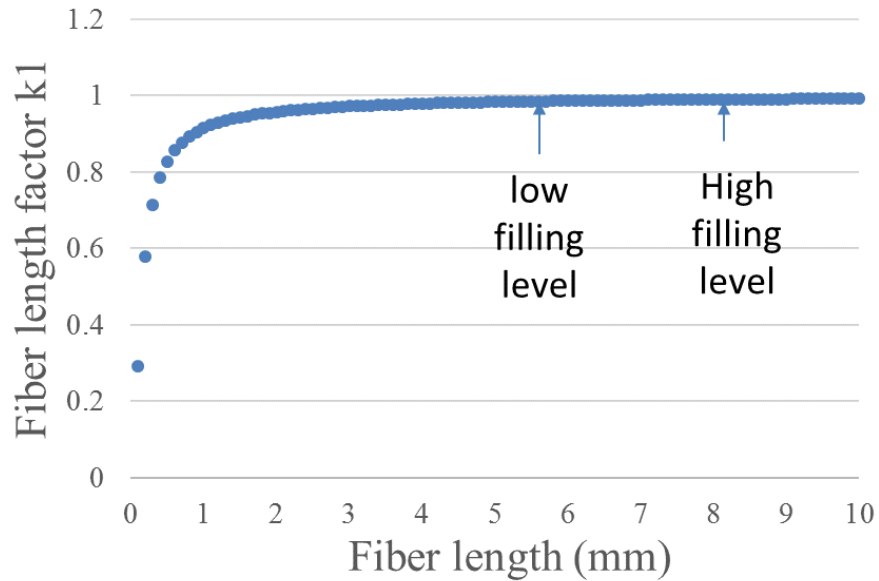


Figure 4-24 Fiber length factor k_1 calculated with different average fiber length based on shear lag model.

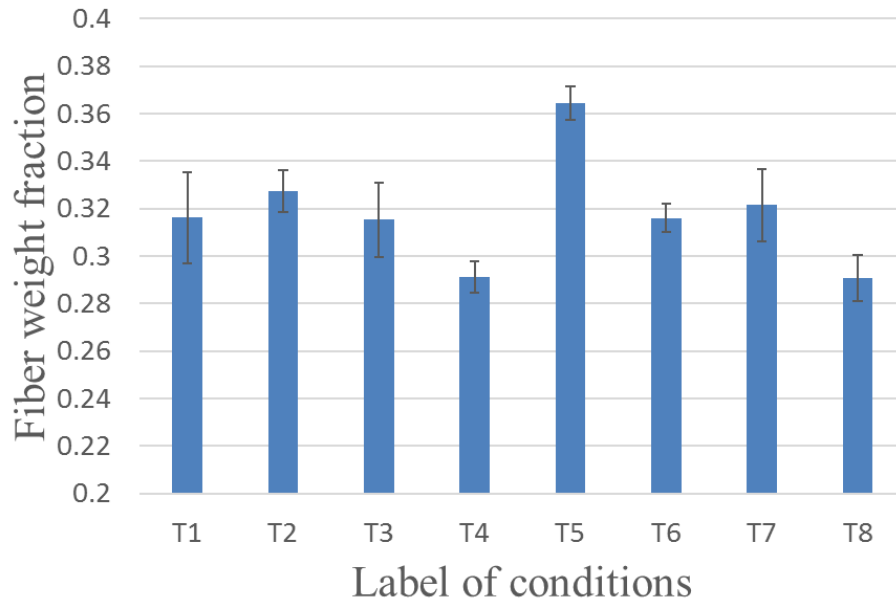


Figure 4-25 Fiber contents measured on D-LFTs prepared in different conditions (T1: standard condition; T2&T3: lower and higher screw speed; T4&T5: higher and lower filling level; T6&T7: lower and higher melt temperature; T8: fiber preheating).

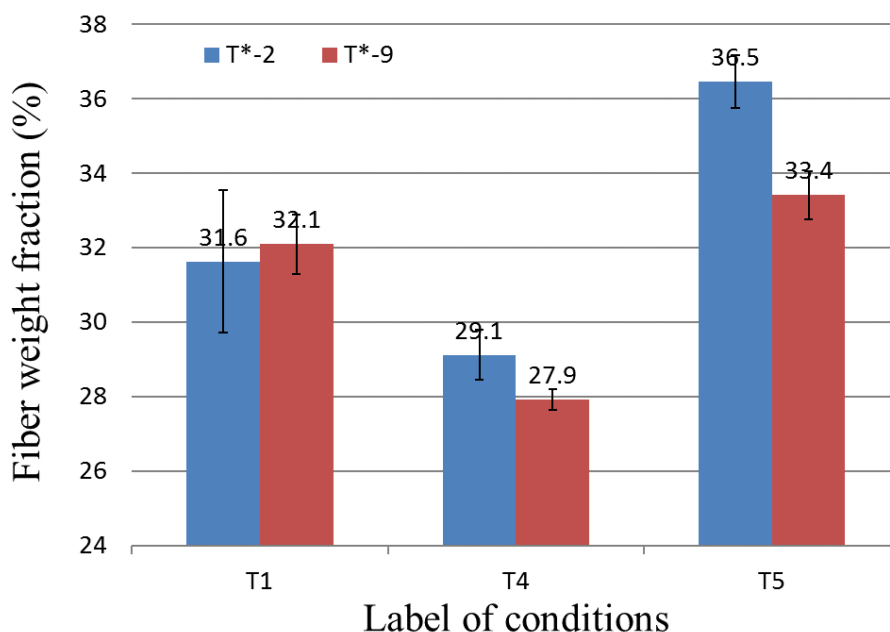


Figure 4-26 Fiber content measured on both the 2nd and the 9th out of 10 D-LFT plaques for T1, T4 and T5.

4.3 Mechanical behavior of glass fiber/PA6 D-LFT at different temperatures

Since the components made with this new material are expected to experience a range of temperature during their service lifetime, the aim of the work described in this section is to characterize the influence of temperature on the mechanical properties of this new material. In this section, tensile and flexural tests at -40°C , R.T., 85°C and 120°C were performed on glass fiber/PA6 D-LFT plaques with 20, 30 and 40 wt.% fibers. The mechanical properties were summarized and analyzed. The failure mode of all the testing samples is also investigated through SEM observation.

4.3.1 Tested mechanical properties

The tensile and flexural stress-strain curves for glass fiber/PA6 D-LFTs with different fiber contents at 4 different temperatures are shown in **Figure 4-27**. At lower temperatures (-40°C and R.T.), both tensile and flexural samples undergo only elastic deformation and have brittle failures. But at higher temperatures (85°C and 120°C), the

tensile stress starts to flatten after elastic deformation and then fails in a brittle way while flexural specimens undergo a large plastic deformation after the peak load. That indicates the tensile failure changes from a brittle type at low temperature to a mixture of brittle and ductile at high temperature while the flexural failure changes from a brittle type at low temperature to a ductile type at high temperature. This tendency is similar for the specimens with different fiber content.

The tensile and flexural moduli are summarized in **Figure 4-28**. Both tensile and flexural modulus decrease as temperature increases. If compared with the properties at R.T., tensile and flexure modulus increase by 14-25% and 8-12% at -40°C , decrease by 30-40% and 31-34% at 85°C , and decrease by 31-45% and 39-42% at 120°C , respectively.

The tensile and flexural strengths are summarized in **Figure 4-29**. Both tensile and flexural strength decrease as temperature increases. If compared with the properties at R.T., tensile and flexure strength increase by 8-22% and 5-13% at -40°C , decrease by 33-40% and 33-38% at 85°C , and decrease by 42-51% and 43-47% at 120°C , respectively.

The tensile and flexural strains at failure are summarized in **Figure 4-30**. Both tensile and flexural strain at failure are just found to increase slightly when temperature increases from R.T. to 85°C . No strong correlation can be derived between the strain at failure and temperature.

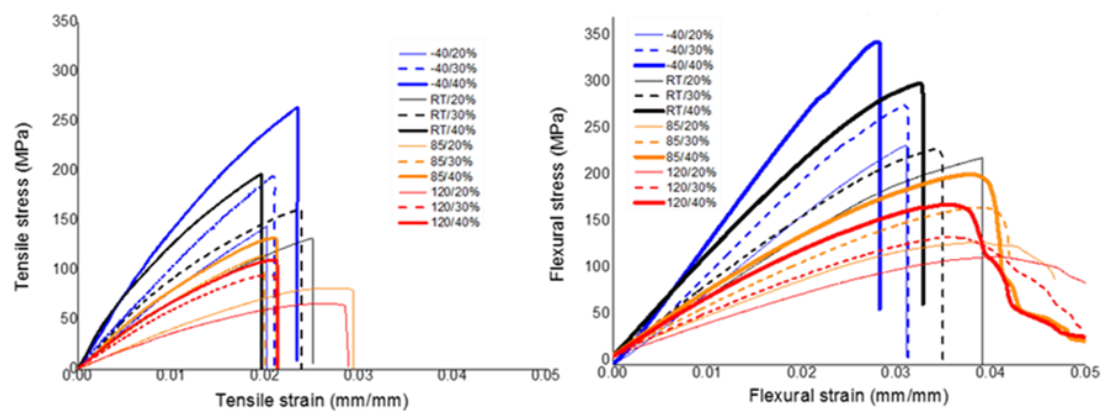


Figure 4-27 Tensile and flexural stress-strain curves at -40°C , R.T., 85°C and 120°C for the D-LFTs with fiber contents of 20, 30 and 40 wt.%.

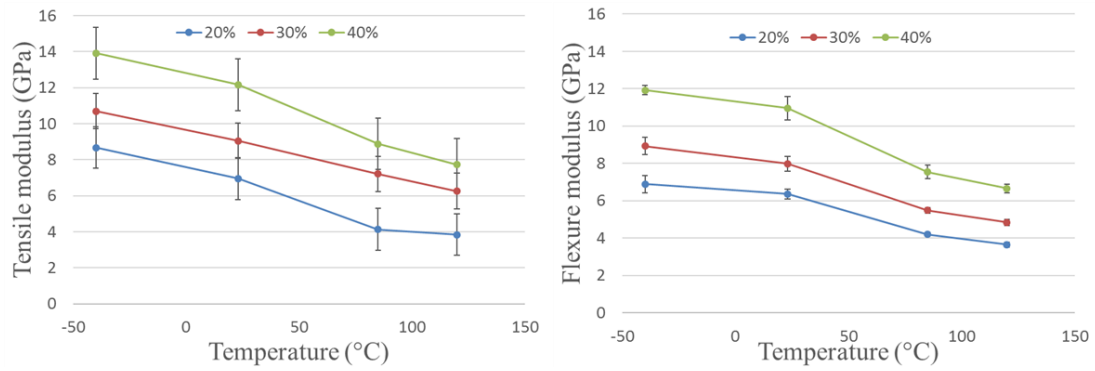


Figure 4-28 Tensile and flexural moduli tested at -40°C, R.T., 85°C and 120°C of D-LFTs with fiber contents of 20, 30 and 40 wt.%.

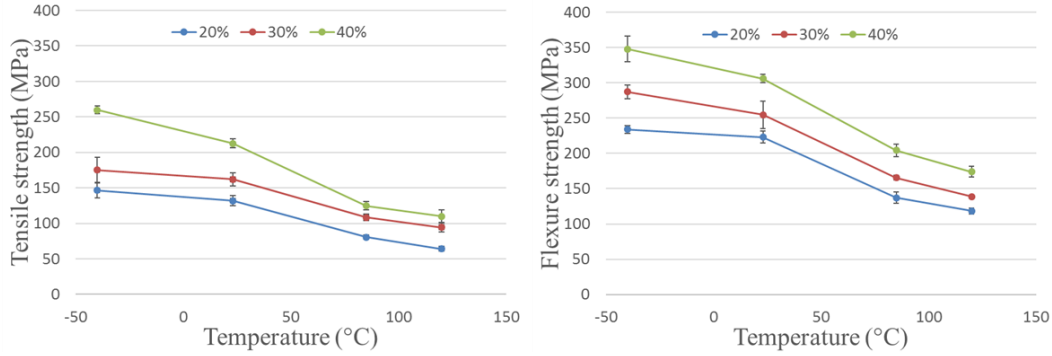


Figure 4-29 Tensile and flexural strengths tested at -40°C, R.T., 85°C and 120°C of D-LFTs with fiber contents of 20, 30 and 40 wt.%.

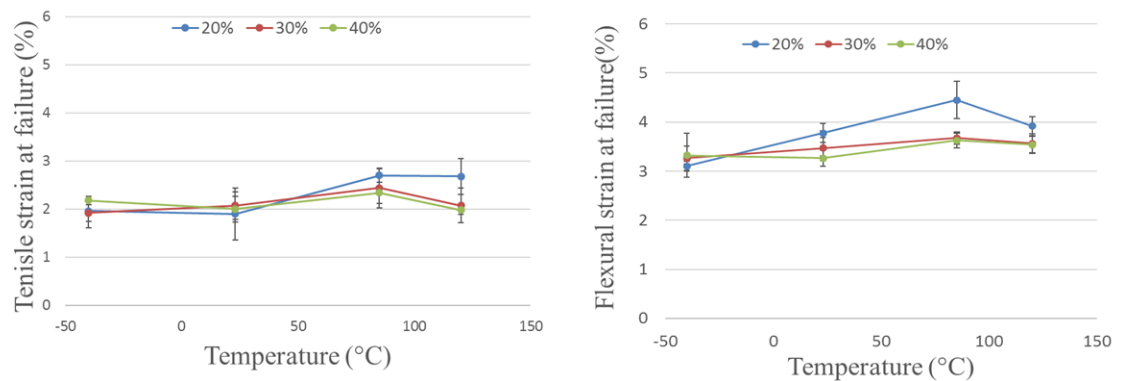


Figure 4-30 Tensile and flexural strain at failure tested at -40°C, R.T., 85°C and 120°C of D-LFTs with fiber contents of 20, 30 and 40 wt.%.

4.3.2 Analysis of failure mode

Figure 4-31 shows the failed tensile specimens with fracture surface on the top. Comparing those with 40 wt.% fiber tested at different temperature, many secondary cracks off the main fracture surface appear on the one tested at -40°C but disappear on the one tested at 120°C . The amount of these secondary cracks decreases with increasing temperature. This means that when temperature increases from -40°C to 120°C the failure mode transitions gradually from a mixture of one main crack propagation with many secondary cracks off the main fracture surface, to a single main crack propagation. And if comparing those with different fiber fraction, it is found that the amount of secondary crack at the same temperature decreases with decreasing fiber fraction. The reason might be the higher fiber fraction improves the longitudinal strength but has little effect on interface strength, which leads to more secondary crack propagation.

The fracture surfaces of the failed tensile samples were observed by a SEM to analyze the failure mode. The fracture surface of tensile samples with 20 wt.% fiber tested at -40°C are shown in **Figure 4-32**. The matrix holes indicate that the dominating tensile failure mode at -40°C is fiber pull out. The fibers aligned parallel to the load direction broke in a tensile manner while those aligned off the load direction fractured by bending. The smooth matrix surface indicates that the failure is very brittle at -40°C , which is consistent with the stress-strain curves. There are also many fiber bundles in the core portion.

The fracture surface of tensile samples with 20 wt.% fiber tested at R.T. are shown in **Figure 4-33**. Fiber pull out is also found to be the main failure mode at this temperature. Compared with the case at -40°C , the matrix surface gets rougher at R.T., indicating that the matrix undergoes more plastic deformation.

The fracture surface of tensile samples with 20 wt.% fiber tested at 85°C are shown in **Figure 4-34**. The fracture surface consists of a major smooth region and a small dimple-type region. The smooth region is similar to the observations at lower temperatures with fiber pull out and matrix rupture evident on the surface. In the core portion with many

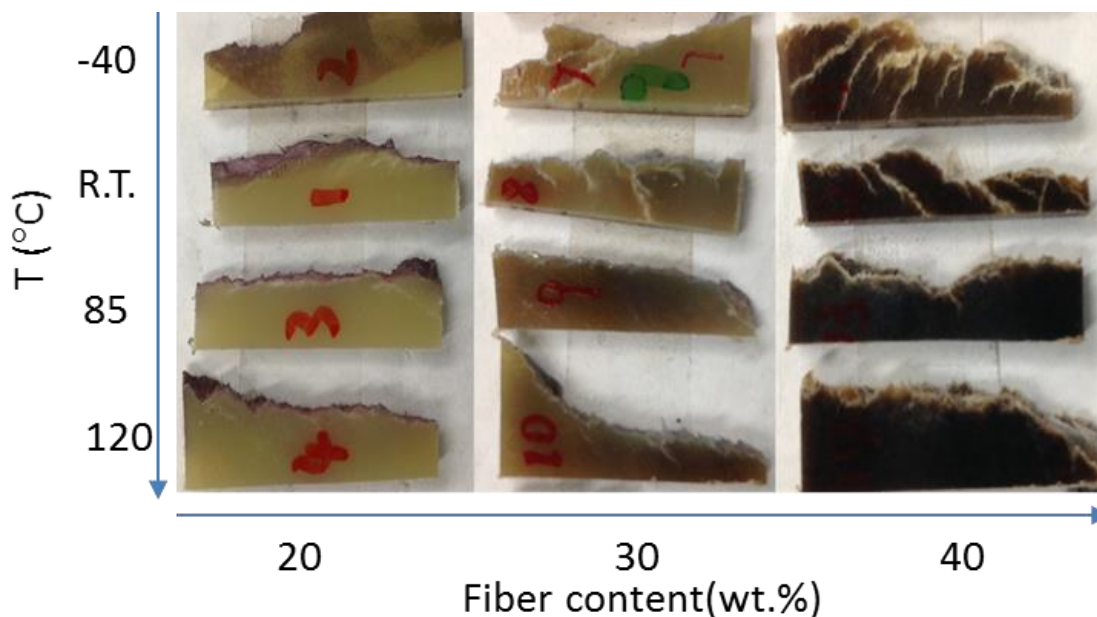


Figure 4-31 Failed tensile specimens tested at -40°C , R.T., 85°C and 120°C of D-LFTs with fiber contents of 20, 30 and 40 wt.%.

fiber bundle, some small pieces of matrix debris demonstrate the brittle failure. The matrix surface is somewhat rougher than those tested at R.T. For the dimple-type part, the matrix stretches out entirely with significant plastic deformation, indicating ductile failure. The fibers are completely detached from the matrix. The transition region between two parts is very hard to distinguish. The mixed fracture surface shows that the failure starts with a ductile matrix plastic deformation and abruptly transform to a brittle rupture. And this phenomenon is consistent with the tested stress-strain curves.

The fracture surface of tensile samples with 20 wt.% fiber tested at 120°C are shown in **Figure 4-35**. As was the case at 85°C , the fracture surface consists of a brittle part and a ductile part. The matrix surface in brittle part becomes much rougher than the previous ones while the matrix in ductile part undergoes more plastic deformation. Both observations indicate that the matrix gets softer at higher temperature.

Figure 4-36 shows the details of interface region between fiber and matrix at different temperatures. At -40°C , the fiber is completely covered by a layer of polymer. The sharp wrinkles of the matrix surface show that the matrix is brittle at -40°C . When it goes up to

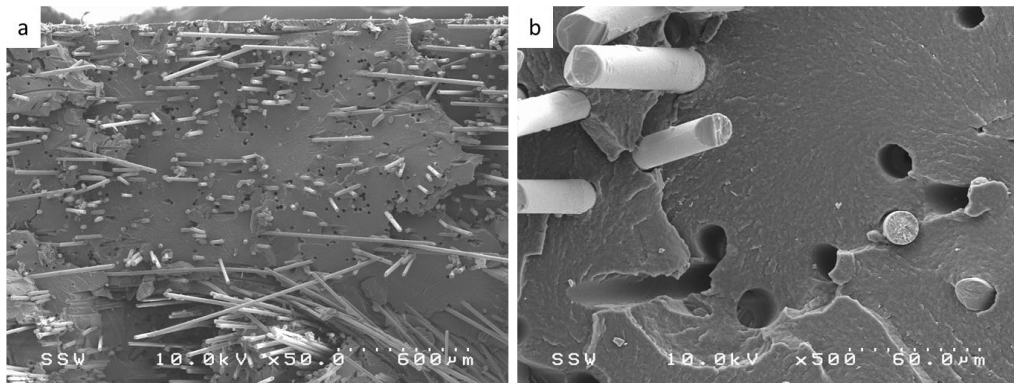


Figure 4-32 SEM images of fracture surfaces of tensile D-LFT specimens with 20 wt.% fiber tested at -40°C .

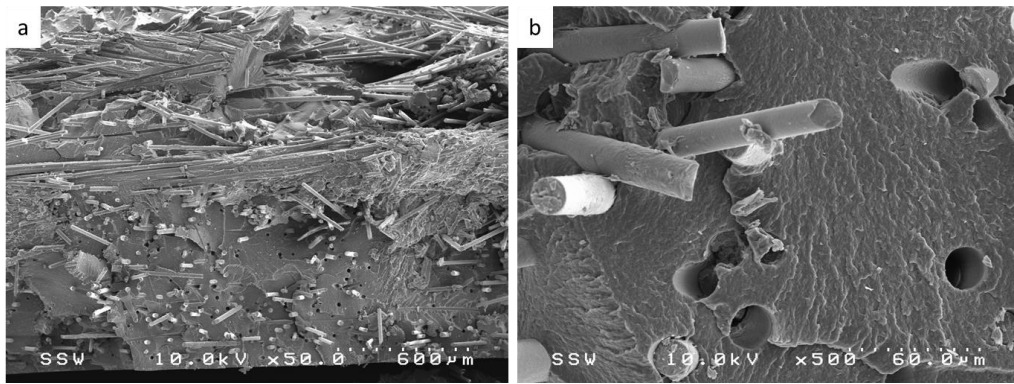


Figure 4-33 SEM images of fracture surfaces of tensile D-LFT specimens with 20 wt.% fiber tested at R.T.

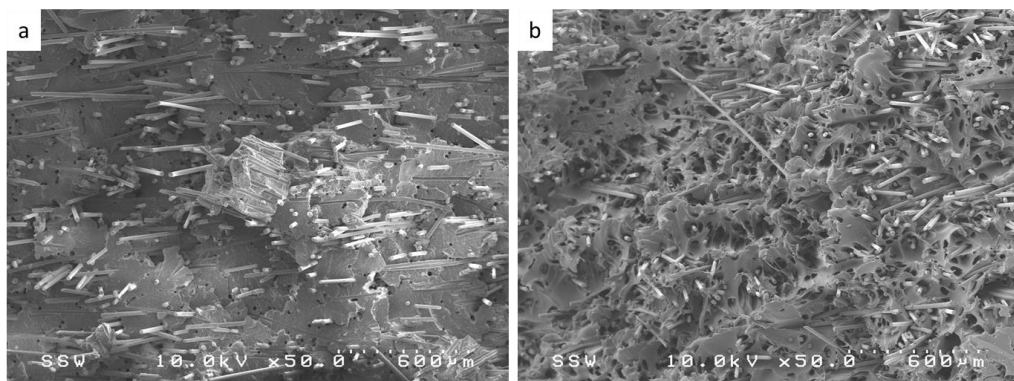


Figure 4-34 SEM images of fracture surface of tensile D-LFT specimens with 20 wt.% fiber tested at 85°C .

RT, the dark ring around the fiber still indicates the debonding between fiber and matrix exists. The more polymer linking mark and more gentle wrinkles on the matrix surface indicates that the polymer became more ductile. When the temperature goes up to 85°C or 120°C, no dark ring can be found. The fibers are entirely covered by matrix which undergoes a large deformation. The wrinkles on the matrix surface become blurrier. The phenomenon suggests that the increasing temperature softens the matrix and reduce the capacity of the matrix to transfer load to the fibers. For specimens with 30 wt.% and 40 wt.% fiber as shown in **Figure 4-37**, the tendency is the same. The only difference found is for those with 40 wt.% fiber tested at R.T. and -40°C, there are many secondary cracks propagating perpendicular to the main fracture surface, around which there are always some fiber concentration. This matches well with our previous macrographs of the failed specimens.

4.4 Characterization of the mechanical behavior of UD tape reinforced D-LFT with different stacking sequence

Glass fiber/PA6 UD tapes with 60 wt.% fiber were employed to co-mold with glass fiber/PA6 D-LFT material with 30 wt.% fiber. The three types of stacking sequence are UD $[0]_8$, orthotropic $[(0/90)_2]_s$ and quasi-isotropic $[0/90/+45/-45]_s$. Three types of symmetric co-molded plaques (comouldings) and relevant consolidated UD laminates without D-LFT material (layups) were successfully prepared. Tensile, flexural, shear and impact tests were performed on three types of comouldings, three types of layups and pure D-LFT plaque with 30 wt.% fiber which is the core materials for all the comouldings. The mechanical properties and failure modes of different samples were summarized. The reinforcement efficiency of different stacking sequence was analyzed. The theoretical and experimental in-plane elastic properties of comouldings and layups were compared and correlated with the microstructure.

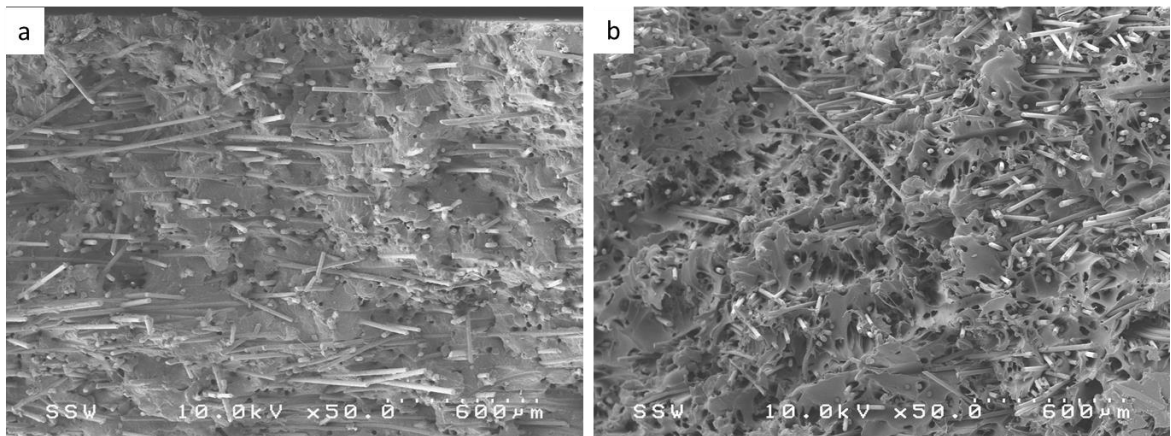


Figure 4-35 SEM images of fracture surface of tensile D-LFT specimens with 20 wt.% fiber tested at 120°C.

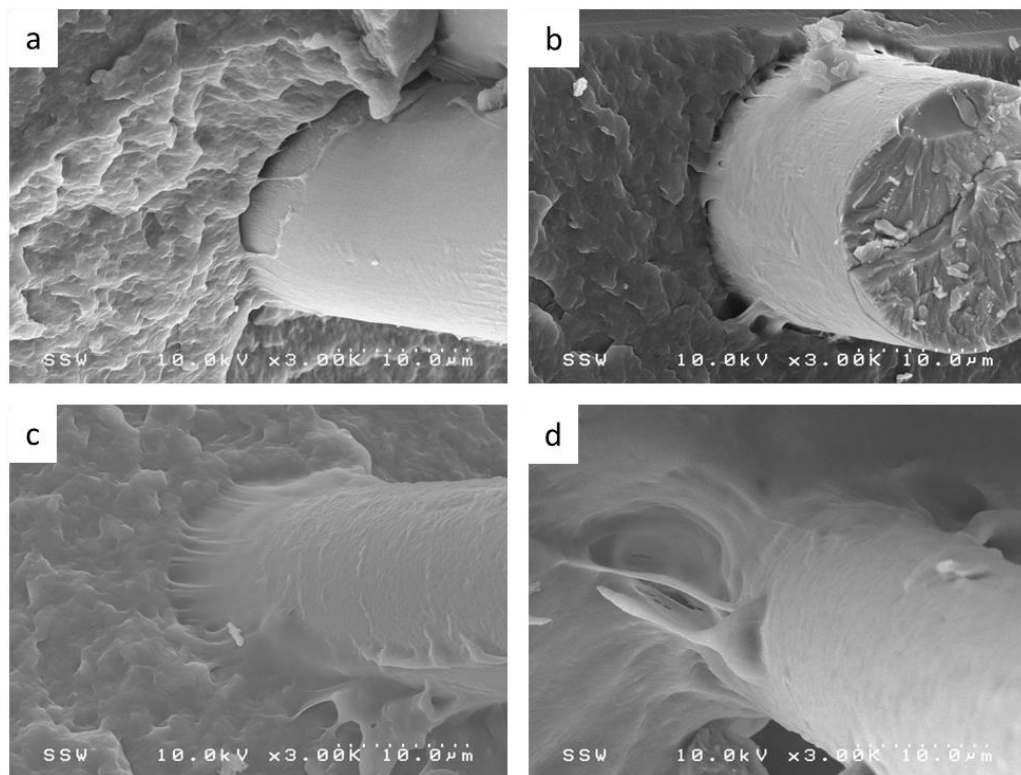


Figure 4-36 SEM images of fracture surfaces of tensile D-LFT specimens with 20 wt.% fiber tested a: -40°C, b: R.T., c: 85°C and d: 120°C.

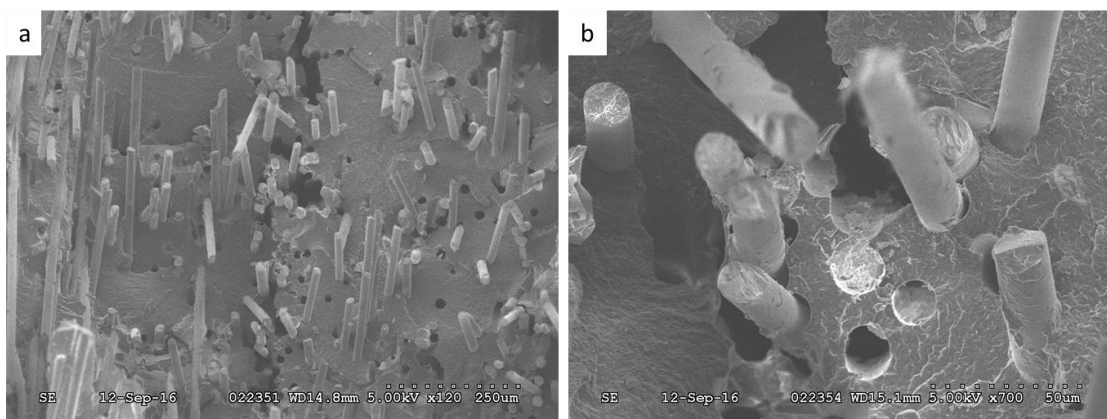


Figure 4-37 SEM images of fracture surface of tensile D-LFT specimens with 40 wt.% fiber tested at R.T.

4.4.1 Tested mechanical properties

4.4.1.1 Impact properties

Thickness specific impact energy and peak load of the comouldings, the layups and pure D-LFT are shown in **Figure 4-38**. The layups and comoldings have much higher impact properties than the pure D-LFT. As comouldings have large amount of highly aligned continuous fibers and higher fiber content than pure D-LFT, the UD tape reinforcement can significantly improve the impact properties of D-LFT material. Among the three types of layups, #1L has the lowest properties while the other two are close. That might be due to the highly anisotropy of UD laminates which tend to split apart during the impact tests. However, among three types of comouldings, #1C has almost the highest impact properties while #2C is slightly lower than #3C.

The different failed puncture specimens are shown in **Figure 4-39**. The D-LFT specimens failed in a brittle manner. For three types of layups, the top split #1L, penetrated #2L in a biaxial way and penetrated #3L in an irregular shape, which is related to the different anisotropy. With the highest anisotropy, #1L is quite weak in 90°-direction such that the sample was just split apart without any fiber breakage, which result in the quite low impact properties. However, the failed #1C samples with more plastic deformation and more fiber breakage looks more isotropic. That might be caused

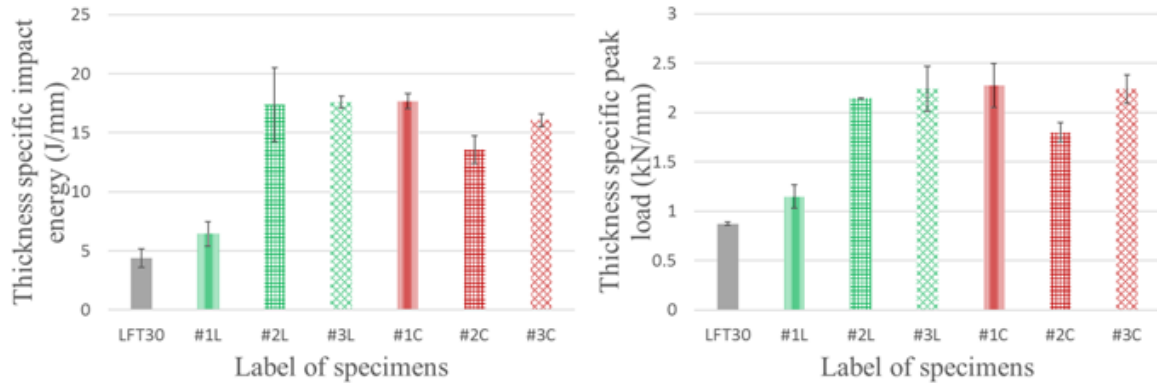


Figure 4-38 Thickness specific impact energy and thickness specific peak load tested on pure D-LFT with 30 wt.% fiber, layups and comouldings with 3 types of stacking sequence ($[0]_s$, $[0/90]_s$ and $[0/90/+45/-45]_s$).

by the incorporation of D-LFT layer and two additional laminae in 90° -direction which bond the fibers together and improve the impact properties. It is also found that the failures of #3L and #3C are more isotropic than those of #2L and #2C.

Generally, the pure D-LFT material has much lower impact properties than the layups. But if they were co-molded together, the resulting comoulding material will possess almost the same impact properties with the relevant layup, which indicates the more isotropic D-LFT layer which bonds the UD laminates together also contribute to the impact properties of the comouldings.

4.4.1.2 Tensile properties

The tensile stress-strain curves for different samples are shown in **Figure 4-40**. Most of the specimens show brittle failures after peak load without any yielding, while only #1L show a step-by-step failure. The smooth stress-strain curves indicate that the bonding between different layers is strong enough to make all the layers deform together until the failure under the tensile load condition.

The derived tensile properties are summarized in **Figure 4-41**. For the layups, Young's modulus of #1L is higher than 30 GPa in 0° -direction but lower than 5 GPa in 90° -

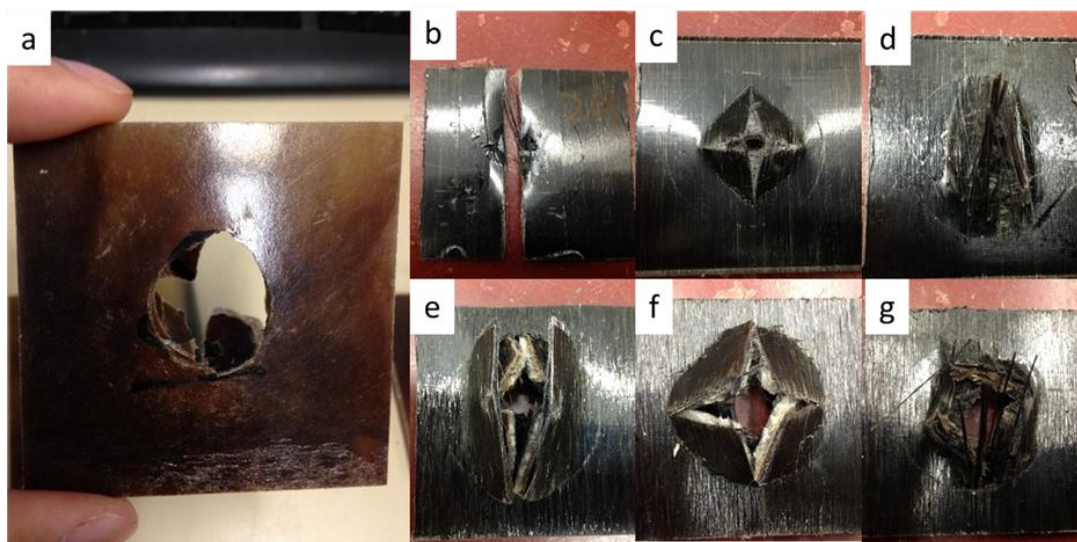


Figure 4-39 Failed puncture specimens: a) D-LFT, b) #1L, c) #2L, d) #3L, e) #1C, f) #2C and g) #3C.

direction, while those of #2L and #3L are 17 GPa and 14GPa, respectively. Compared with the relevant layups, the anisotropy of comouldings is reduced for first type but increased for the other two types. Compared with the properties of pure D-LFT, #1C is reinforced in 0° -direction only while the other two are reinforced in multiple directions. The anisotropies of #2C and #3C are derived from D-LFT layer which has more fibers aligned in 0° -direction. The variation trend of the strength is similar to that of the Young's modulus.

The failed tensile specimens are shown in **Figure 4-42**. From the failed #1L sample, it is observed that the failure is a mixture of fiber breakage and shear failure. That is due to the high anisotropy of #1L which makes the shear strength so low that the fiber breakage is followed by shear failure. Different from the failure of #1L, most fibers of #1C are broken. The significant difference of maximum elongation between #1L and D-LFT layer in 0° -direction leads to the delamination observed in failed tensile #1 specimen tested in 0° -direction, while no delamination was found in failed tensile #1 specimen tested in 90° -direction.

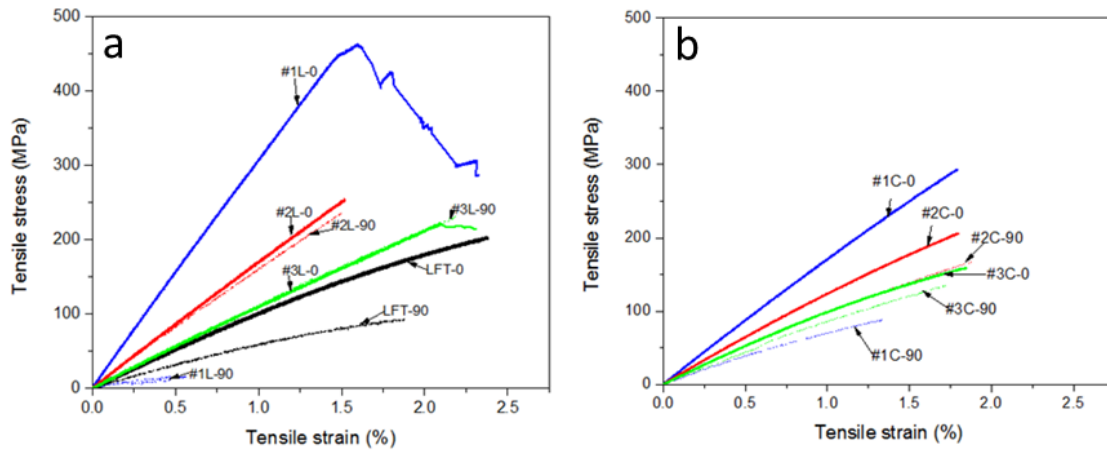


Figure 4-40 Tensile stress-strain curves in 0 and 90°-directions for a) D-LFT and layups with 3 stacking sequences and b) comoldings with 3 stacking sequences.

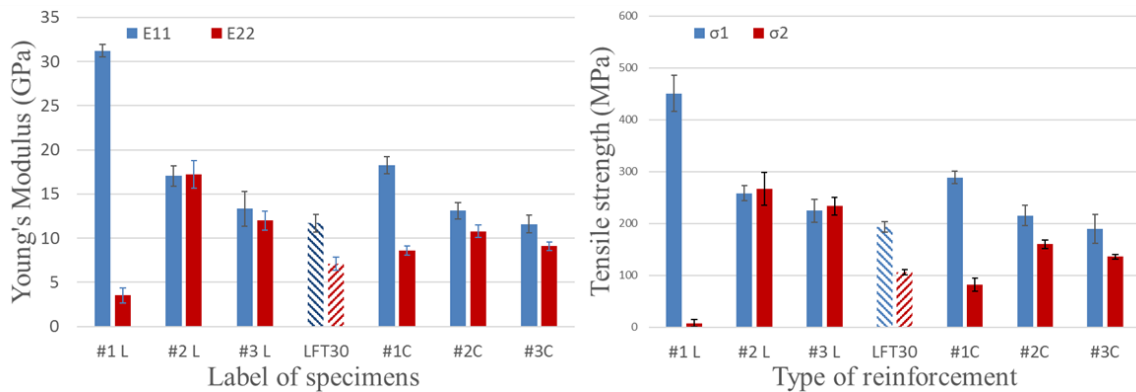


Figure 4-41 Tensile moduli and strengths in 0 and 90°-directions for a) D-LFT and layups with 3 stacking sequences and b) comoldings with 3 stacking sequences.

4.4.1.3 Flexural properties

The flexural stress-strain curves for different samples are shown in **Figure 4-43**. The flexural failures of D-LFT samples are one-step and brittle while those of most layups and comolding are progressive. The progressive failure of co-molded samples might be caused by the difference of elongation and strength between different layers. As flexural properties are more sensitive to the properties of outer layers, the flexural properties in 0°-direction and 90°-direction are not identical for the stacking sequence of $[(0/90)_2]_s$ and $[0/90/+45/-45]_s$.

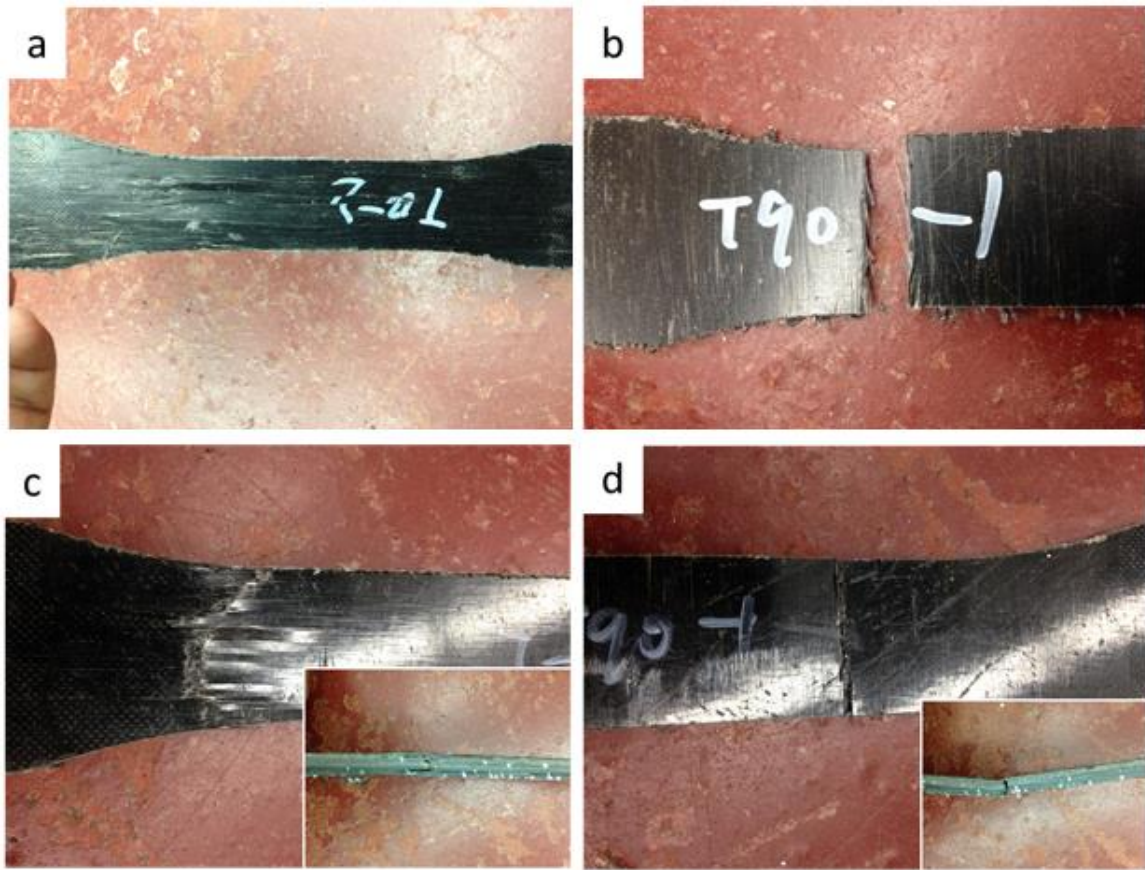


Figure 4-42 Failed tensile samples with stacking sequence of UD [0]₈: a) #1L tested in 0°-direction, b) #1L tested in 90°-direction, c) #1C tested in 0°-direction and d) #1C tested in 90°-direction.

The flexural properties are summarized in **Figure 4-44**. Due to the continuous fiber, higher fiber content and consistent fiber alignment, all layups show much higher flexural modulus and strength than D-LFT. Due to the constructed sandwich structure with stronger and stiffer UD laminates outside, all comouldings also have much higher flexural properties than pure D-LFT. Both layups and comouldings with stacking sequence of [(0/90)₂]_s have higher flexural properties than those with stacking sequence of [0/90/+45/-45]_s.

The failed flexural specimens tested in 90°-direction are shown in **Figure 4-45**. Among the layups with different stacking sequence, the failure of #1L tested in 90°-direction occurs through the whole thickness while that of #2L tested in 90°-direction go through

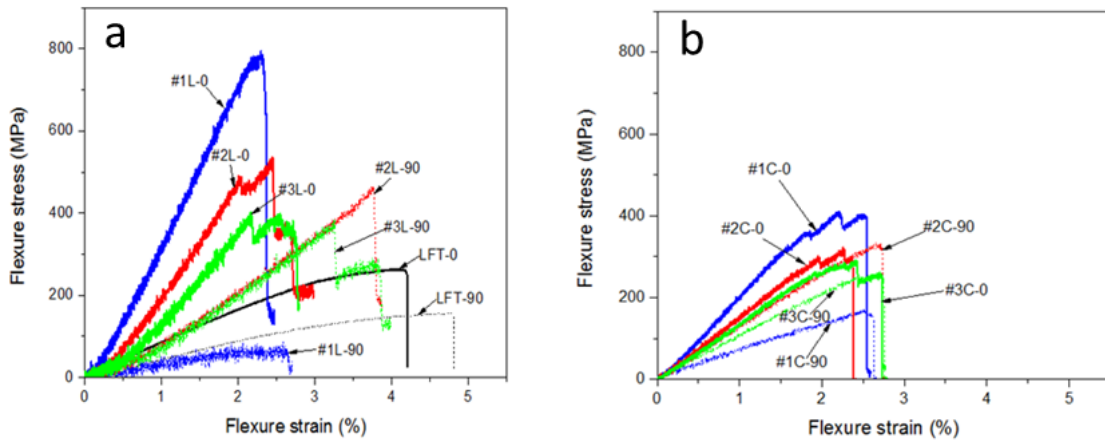


Figure 4-43 Flexural stress-strain curves in both 0° and 90° -directions for a) D-LFT and layups with 3 types of stacking sequence and b) comoldings with 3 types of stacking sequence.

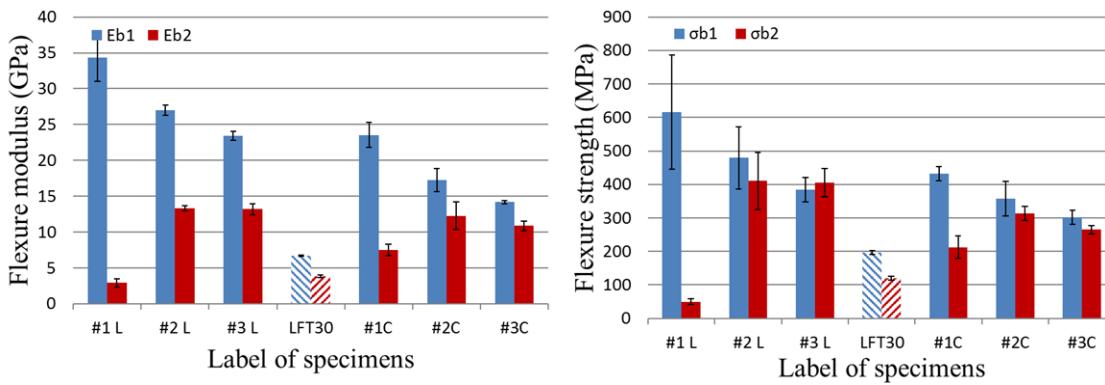


Figure 4-44 Flexural modulus and strength in 0° -direction and 90° -direction for pure D-LFT with 30 wt.% fiber, layups with 3 types of stacking sequence and comoldings with 3 types of stacking sequence.

half the thickness on the tensile side and that of #3L tested in 90° -direction occurs on the compressive side. For the flexural comoulding specimens, the crack of those tested in 0° -direction propagates through half the thickness and stops with delamination at the middle portion of D-LFT layer while the crack of those tested in 90° -direction completely penetrate the whole specimen. This might be caused by the anisotropy of D-LFT layer which is much weaker in 90° -direction than in 0° -direction.

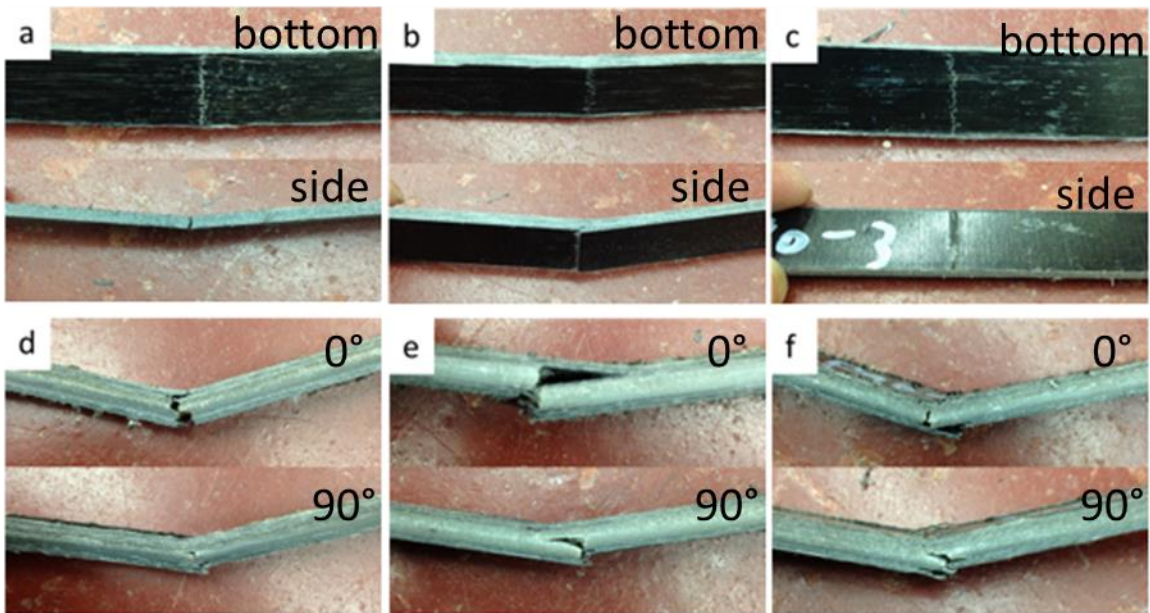


Figure 4-45 Failed flexural specimens tested in 0° -direction of layups and comouldings with three types of stacking sequence: a) #1L tested in 90° -direction viewed from bottom and side, b) #2L tested in 90° -direction viewed from bottom and side, c) #3L tested in 90° -direction viewed from bottom and side, d) #1C tested in 0° and 90° -direction, e) #2C tested in 0° and 90° -direction and f) #3C tested in 0° and 90° -direction.

4.4.1.4 Shear properties

The shear moduli of different specimens are summarized in **Figure 4-46**. Compared with pure D-LFT with 30 wt.% fiber, the shear modulus was only found to be significantly improved by co-molding the layups with stacking sequence of $[0/90/+45/-45]_s$. This can be attributed to the unique $\pm 45^\circ$ layers, which reinforce the shear properties greatly. Since the stress was still increasing when the notched region of specimen already touched the fixture, the shear strength was not achievable by Iosipescu fixture used by this test.

4.4.2 Prediction of in-plane elastic properties

To verify the applicability of this technique, the in-plane elastic properties of layups and comouldings were predicted and compared with the experimental result. Generally, since layups consist of UD laminae which can be treated as transversely isotropic materials, the

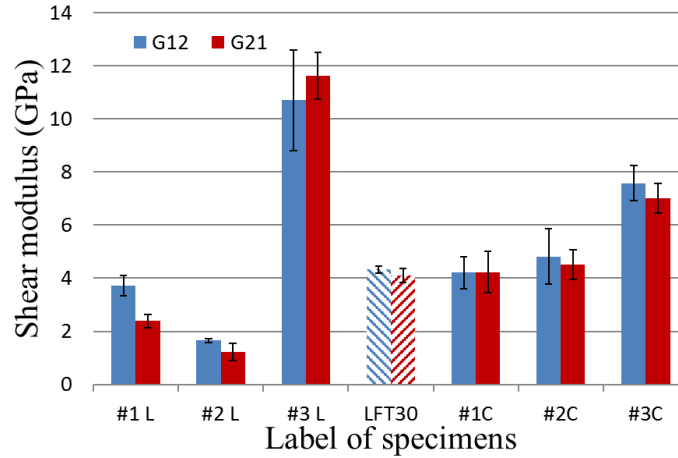


Figure 4-46 Shear modulus in both 0° and 90°-directions for pure D-LFT with 30 wt.% fiber, layups with 3 types of stacking sequence and comoldings with 3 types of stacking sequence.

path for predicting the elastic properties of UD laminates is widely accepted, in which ROM and Halpin-Tsai are employed to predict the elastic properties of one UD lamina and then Classic Laminate Theory (CLT) is used to combine the laminae in different directions together to derive the global elastic properties.

In this work, ROM and Halpin-Tsai were used to predict the elastic properties of a single UD lamina. The elastic properties of D-LFT layer was based on the previous testing results. Finally, the CLT approach was employed based on the layer thickness (0.3 mm for a single UD lamina and 3 mm for one D-LFT layer).

With expression shown below, ROM was employed to predict E_{11} and ν_{12} .

$$E_{11} = V_f \cdot E_f + V_m \cdot E_m \quad (4-6)$$

$$\nu_{12} = V_f \cdot \nu_f + V_m \cdot \nu_m \quad (4-7)$$

Where, E_{11} is longitudinal young's modulus, V is volume fraction, ν is Poisson's ratio, f and m represent fiber and matrix, respectively. Halpin-Tsai model was employed to predict E_{22} and G_{12} with expression as follows

$$E_{22} = E_m \left(\frac{1 + \zeta \eta V_f}{1 - \eta V_f} \right) \quad (4-8)$$

$$G_{12} = G_m \left(\frac{1+\zeta\eta V_f}{1-\eta V_f} \right) \quad (4-9)$$

$$\text{With } \eta = \left(\frac{\frac{M_f}{M_m} - 1}{\frac{M_f}{M_m} + \zeta} \right) \quad (4-10)$$

in which E_{22} is transversal young's modulus, G_{12} is longitudinal shear modulus, ζ is 1 or 2 and $M=E$ or G for E_{22} and G_{12} , respectively. Based on the mechanical testing result, the elastic properties of the 30 wt.% glass fiber/PA6 D-LFT layer are 10.5 GPa of E_{11} , 5.8 GPa of E_{22} , 0.4 of ν_{12} and 4.1 GPa of G_{12} , respectively.

The reduced stiffness matrix of UD lamina can be determined by

$$Q_{ij} = \begin{pmatrix} Q_{11} & Q_{12} & 0 \\ Q_{12} & Q_{22} & 0 \\ 0 & 0 & Q_{66} \end{pmatrix} \quad (4-11)$$

Where

$$Q_{11} = \frac{E_{11}^2}{E_{11} - \nu_{12} \cdot E_{22}} \quad (4-12)$$

$$Q_{12} = \frac{\nu_{12} E_{11} E_{22}}{E_{11} - \nu_{12}^2 \cdot E_{22}} \quad (4-13)$$

$$Q_{22} = \frac{E_{11} E_{22}}{E_{11} - \nu_{12}^2 \cdot E_{22}} \quad (4-14)$$

$$Q_{66} = G_{12} \quad (4-15)$$

With the angles θ and stiffness matrix Q_{ij} , the transformed reduced stiffness matrix \overline{Q}_{ij} for laminae in 0° , 45° , -45° and 90° -directions were calculated based on the expressions as follows

$$\overline{Q}_{11} = Q_{11} \cos(\theta)^4 + 2(Q_{12} + 2Q_{66}) \cos(\theta)^2 \cdot \sin(\theta)^2 + Q_{22} \sin(\theta)^4 \quad (4-16)$$

$$\overline{Q}_{12} = \overline{Q}_{21} = Q_{12}(\cos(\theta)^4 + \sin(\theta)^4) + (Q_{11} + Q_{22} - 4Q_{66}) \cos(\theta)^2 \cdot \sin(\theta)^2 \quad (4-17)$$

$$\overline{Q_{16}} = \overline{Q_{61}} = (Q_{11} - Q_{12} - 2Q_{66})\cos(\theta)^3 \cdot \sin \theta - (Q_{22} - Q_{12} - 2Q_{66}) \cos \theta \cdot \sin(\theta)^3 \quad (4-18)$$

$$\overline{Q_{22}} = Q_{11} \sin(\theta)^4 + 2(Q_{12} + 2Q_{66}) \cos(\theta)^2 \cdot \sin(\theta)^2 + Q_{22} \cos(\theta)^4 \quad (4-19)$$

$$\overline{Q_{26}} = \overline{Q_{62}} = (Q_{11} - Q_{12} - 2Q_{66})\sin(\theta)^3 \cdot \cos \theta - (Q_{22} - Q_{12} - 2Q_{66}) \sin \theta \cdot \cos(\theta)^3 \quad (4-20)$$

$$\overline{Q_{66}} = (Q_{11} + Q_{22} - 2Q_{12} - 2Q_{66}) \cos(\theta)^2 \cdot \sin(\theta)^2 + Q_{66}(\cos(\theta)^4 + \sin(\theta)^4) \quad (4-21)$$

With expressions below, Classical Laminate Theory (CLT) was used to combine different layer together to generate the global stiffness matrix and the elastic properties.

$$Q_{ijg} = \frac{\sum_{k=1}^n (Q_{ijk} t_k)}{\sum_{k=1}^n (t_k)} \quad (4-22)$$

in which Q_{ijg} is the global stiffness matrix, Q_{ijk} is the stiffness matrix for the k layer, t is the thickness of the k layer,

As shown in **Figure 4-47**, even though the tested E_{11} and E_{22} are slightly lower than prediction, they still have a good agreement. The difference in G_{12} and ν_{12} is larger, which might be caused by the non-ideal speckling pattern when using DIC system and insufficient capability of Iosipescu fixture. Even so, the relevant trend still matches well.

4.4.3 Microstructure

From the SEM micrographs taken on the polished cross section of #3C shown in **Figure 4-48**, different UD laminae and D-LFT layer can be easily identified. The structure of the layers is identical to the initial configuration, which indicates both UD laminae and D-LFT material stay at the initial position during the molding without any significant shift. No defects are found along the interface between layups and D-LFT layer which demonstrates the interfacial bonding between two materials is strong enough. However, some differences were noticeable between the top and bottom portions of the specimens, which are based on their relative positions in the mold. In the top portion, some voids and

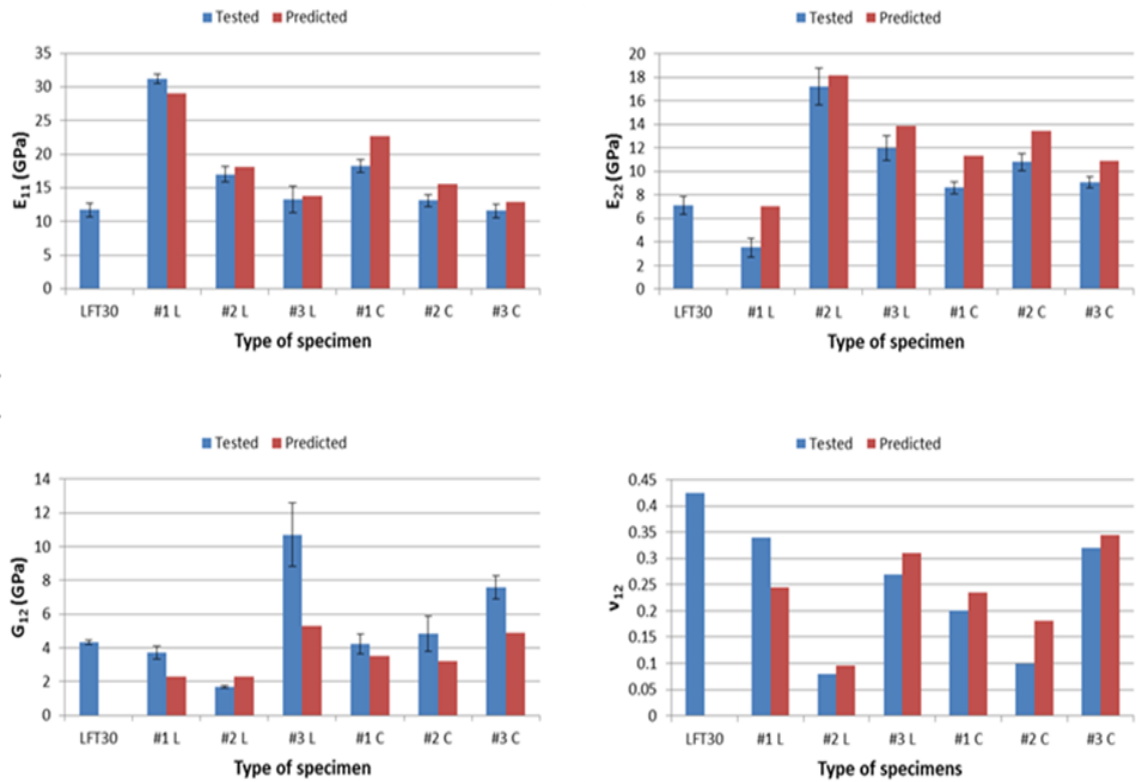


Figure 4-47 Comparison between predicted and experimental elastic properties of layups and relevant comoldings with different stacking sequence.

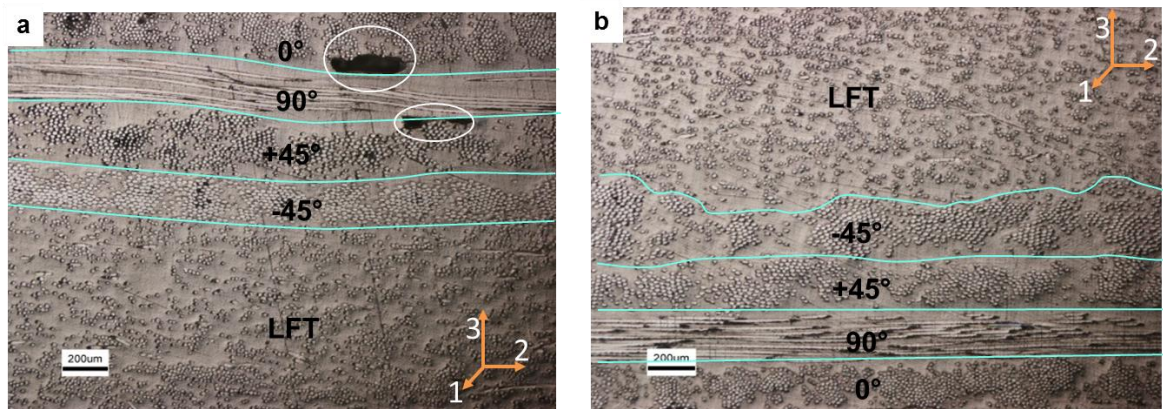


Figure 4-48 Micrographs of a) top portion and b) bottom portion of the cross section of a comoulding product with stacking sequence of $[0/90/+45/-45]_s$.

winding laminae are found whereas, in the bottom portion, some parts of the -45° lamina extend to the D-LFT layer which results in the jagged interface. The difference might be caused by the operation of the charge loading, in which the preheated bottom layup was put in the tool at first, followed by the loading of D-LFT charge and then the preheated top layup. As exposed in the air at room temperature longer than the bottom layup, the top one tends to cool down faster so that some air between different layers might not be able to get out during the molding process. The relatively higher temperature might make the inner layer of bottom layups affected by the flow of D-LFT charge during the molding process. Finally, these defects in the microstructure might have negative effects on the mechanical properties of the co-molded plaques and interpret the difference between the tested and predicted results.

Chapter 5

5 Conclusion

Mechanical tests and observations of the microstructure performed on this new material have furthered our knowledge of the relationship between the mechanical properties and some fundamental factors including fiber content, processing parameters, service temperature and tailored reinforcement. The scope of mechanical test data is sufficient to establish finite element simulation capacity.

5.1 Summary

Glass fiber/PA6 composite plaques with 20-60 wt.% fiber were successfully produced on the Dieffenbacher direct long fiber thermoplastic in-line compounding (D-LFT-ILC) line. Tensile, flexural, shear and impact tests were performed on samples cut from relatively homogeneous regions of the D-LFT plaques. The result of mechanical tests shows that the tensile, flexural and shear moduli increase with the increase of fiber content over the whole range. The strengths are improved by the increase of fiber content from 20 wt.% to around 40 wt.%. With further increase of fiber content above 40 wt.%, tensile strength drops and shear strength forms a plateau while only flexural strength continues to go up. The different responses are related to the possible wet-out issue and inhomogeneous fiber distribution. With fiber length distribution (FLD) and fiber orientation distribution (FOD) measured on D-LFT specimen with 30 wt.% fiber, Young's modulus in both 0°-direction and 90°-direction were predicted by Halpin-Tsai (H-T) and modified rule of mixture (MROM) models of which both were found to work well on E_{11} with a less than 10% overestimation, but underestimate E_{22} by more than 20%.

Under different processing parameters including melt temperature, screw speed, filling level and fiber preheating, 8 types of D-LFT plaques with 30% fiber content were successfully produced. Tensile and flexural testing results indicate that these processing parameters have limited effect on the mechanical properties of D-LFT plaques. Filling level is the only factor that was shown to affect the stiffness of the D-LFT specimens. Even though higher filling level is found to retain longer fiber in the final D-LFT plaques,

the variation of Young's modulus with different filling level is mainly caused by the unexpected variation of fiber content.

Tensile and flexural tests at -40-120°C were performed on D-LFT specimens with 20-40 wt.% fiber. The result shows that the increase of temperature degrades both moduli and strength significantly. That is attributed to the softened matrix and weakened interface bonding. The failure becomes more ductile at elevated temperature. The dominated failure mode changes from fiber breaking/fiber pull out at lower temperatures to fiber pull out/matrix plasticity at higher temperatures.

Unidirectional (UD) tapes with stacking sequence of UD $[0]_8$, orthotropic $[(0/90)_2]_s$ and quasi-isotropic $[0/90/+45/-45]_s$ are found to successfully reinforce D-LFT in different ways. The microstructure of co-molded plaques with different fiber alignments matches well with initial configuration. The global in-plane elastic properties predicted using Classical Laminate Theory (CLT) match well with the experimental results. Tailored reinforcement with UD tapes is shown to be a feasible and predictable method to locally adjust the mechanical properties of a D-LFT material.

5.2 Future work

More measurement of fiber length distribution and fiber orientation distribution will be performed to evaluate the effect of fiber content on the fiber length and fiber orientation of D-LFT material.

To gain a knowledge of how the fibers are aligned during the compression molding, the effect of processing parameters, which are related to the compression molding process such as mold temperature, speed profile of the crosshead, compressive pressure and charge placement, on the mechanical properties of D-LFT material need to be evaluated.

Since PA6 is more hydrophilic than many other polymers, the effect of moisture content on the mechanical properties of glass fiber/PA6 D-LFT need to be investigated. More effort can be made to the powder coating which might be a good way to reduce the moisture absorption of the materials.

6 References

1. Hull, D., & Clyne, T. W. (1996). *An introduction to composite materials*. Cambridge university press.
2. Campbell, F. C. (2010). *Structural composite materials*. ASM international.
3. Brosius, D. (2015, July 1). Thermosets vs. thermoplastics: Is the battle over?. Retrieved from: <http://www.compositesworld.com/articles/thermosets-vs-thermoplastics-is-the-battle-over>.
4. Schemme, M. (2008). LFT–development status and perspectives. *Reinforced Plastics*, 52(1), 32-39.
5. Bowland, C., & vd Woude, J. A formulation study of long fiber thermoplastic polypropylene (part 4): the effect of molding changes on mechanical properties of pp LFT parts.
6. Penn, L., & Larsen, F. (1979). Physicochemical properties of kevlar 49 fiber. *Journal of Applied Polymer Science*, 23(1), 59-73.
7. Polyamides. (2013, May 7). Retrieved from: <http://www.essentialchemicalindustry.org/polymers/polyamides.html>
8. Bennett, S. C., & Johnson, D. J. (1978). Structural heterogeneity in carbon fibers. In *Proceedings of the Fifth London International Carbon and Graphite Conference* (p. 377).
9. Cox, H. L. (1952). The elasticity and strength of paper and other fibrous materials. *British journal of applied physics*, 3(3), 72.
10. Thomason, J. L. (2009). The influence of fibre length, diameter and concentration on the impact performance of long glass-fibre reinforced polyamide 6, 6. *Composites Part A: Applied Science and Manufacturing*, 40(2), 114-124.
11. Thomason, J. L. (2002). The influence of fibre length and concentration on the properties of glass fibre reinforced polypropylene: 5. Injection moulded long and short fibre PP. *Composites Part A: Applied Science and Manufacturing*, 33(12), 1641-1652.
12. Rooney, C. (2011). Long fiber composites. Retrieved from: <https://www.sintef.no/globalassets/project/ffs/dokumenter/seminar-april2011/long-fiber-composites-april2011.pdf>.
13. Henning, F., Ernst, H., & Brüssel, R. (2005). LFTs for automotive applications. *Reinforced plastics*, 49(2), 24-33.
14. Long glass fiber thermoplastics: material classification and characterization. (2001). Retrieved from: http://eatc-online.org/media/schemme-material_classification.pdf.
15. Malnati, P. (2007, January 1). Reinforced thermoplastics: LFRT vs. GMT. Retrieved from: <http://www.compositesworld.com/articles/reinforced-thermoplastics-lfirt-vs-gmt>.

16. Malnati, P. (2013, January 4). Evolution of tailored D-LFT. Retrieved from: <http://www.compositesworld.com/articles/evolution-of-tailored-d-lft>.
17. Ernst, H., Henning, F., & Robbins, J. R. (2009). Long Fiber Reinforced Thermoplastic LFT-D and Thermosetting D-SMC Processes for Lightweight Parts Production-Trends and Recent Applications. In *Prof. of 9th ACCE Conference*.
18. Brümmer, M., & Henning, F. (2006). Press Technology for LFT-D Part Production. *SPE ACCE*.
19. Henning, F., & Geiger, O. (2005). New Long Rayon Fiber Reinforced Thermoplastics Utilizing the LFT-D Process. *SPE ACCE*.
20. Emerson, D., Grauer, D., Hangs, B., Reif, M., Henning, F., Martsman, A., ... & Jespersen, S. T. (2012). Using unidirectional glass tapes to improve impact performance of thermoplastic composites in automotive applications. *Proceedings SPE ACCE, 12*, 11-13.
21. Henning, F., Ernst, H., & Brüssel, R. (2003). Innovative process technology LFT-D-NF offers new possibilities for emission reduced long-natural fiber-reinforced thermoplastic components. *SPE ACCE*.
22. Krause, W., Henning, F., Tröster, S., Geiger, O., & Eyerer, P. (2003). LFT-D—a process technology for large scale production of fiber reinforced thermoplastic components. *Journal of Thermoplastic Composite Materials, 16*(4), 289-302.
23. Lee, N. J., & Jang, J. (1999). The effect of fibre content on the mechanical properties of glass fibre mat/polypropylene composites. *Composites Part A: Applied Science and Manufacturing, 30*(6), 815-822.
24. Thomason, J. L., & Vlug, M. A. (1996). Influence of fibre length and concentration on the properties of glass fibre-reinforced polypropylene: 1. Tensile and flexural modulus. *Composites Part A: Applied science and manufacturing, 27*(6), 477-484.
25. Fu, S. Y., Lauke, B., Mäder, E., Yue, C. Y., & Hu, X. (2000). Tensile properties of short-glass-fiber-and short-carbon-fiber-reinforced polypropylene composites. *Composites Part A: Applied Science and Manufacturing, 31*(10), 1117-1125.
26. Thomason, J. L., Vlug, M. A., Schipper, G., & Krikor, H. G. L. T. (1996). Influence of fibre length and concentration on the properties of glass fibre-reinforced polypropylene: Part 3. Strength and strain at failure. *Composites Part A: Applied Science and Manufacturing, 27*(11), 1075-1084.
27. Thomason, J. L., & Groenewoud, W. M. (1996). The influence of fibre length and concentration on the properties of glass fibre reinforced polypropylene: 2. Thermal properties. *Composites Part A: Applied Science and Manufacturing, 27*(7), 555-565.
28. Thomason, J. L., & Vlug, M. A. (1997). Influence of fibre length and concentration on the properties of glass fibre-reinforced polypropylene: 4. Impact

- properties. *Composites Part A: Applied Science and Manufacturing*, 28(3), 277-288.
29. Thomason, J. L. (2005). The influence of fibre length and concentration on the properties of glass fibre reinforced polypropylene. 6. The properties of injection moulded long fibre PP at high fibre content. *Composites Part A: Applied Science and Manufacturing*, 36(7), 995-1003.
 30. Thomason, J. L. (2007). The influence of fibre length and concentration on the properties of glass fibre reinforced polypropylene: 7. Interface strength and fibre strain in injection moulded long fibre PP at high fibre content. *Composites Part A: applied science and manufacturing*, 38(1), 210-216.
 31. Thomason, J. L. (2008). The influence of fibre length, diameter and concentration on the strength and strain to failure of glass fibre-reinforced polyamide 6,6. *Composites Part A: applied science and manufacturing*, 39(10), 1618-1624.
 32. Bowland, C. (2008). A formulation study of long fiber thermoplastic polypropylene (Part 1): the effects of coupling agent, glass content & resin properties on the mechanical properties. In *SPE Automotive and Composites Division: 8th Annual Automotive Composites Conference and Exhibition* (pp. 197-207).
 33. Bowland, C., Busche, B., & Woude, J. V. (2011). A formulation study of long fiber thermoplastic polypropylene (part 3): mechanical properties of pp DLFT composites. *PowerPoint Presentation at Automotive Composites Conference and Exhibition*.
 34. Han, K. Q., Liu, Z. J., & Yu, M. H. (2005). Preparation and mechanical properties of long glass fiber reinforced PA6 composites prepared by a novel process. *Macromolecular Materials and Engineering*, 290(7), 688-694.
 35. Ozkoc, G., Bayram, G., & Bayramli, E. (2005). Short glass fiber reinforced ABS and ABS/PA6 composites: processing and characterization. *Polymer composites*, 26(6), 745-755.
 36. Varga, C., & Bartha, L. (2014). A novel route for injection moulding of long carbon fibre-reinforced LLDPE. *Journal of Reinforced Plastics and Composites*, 33(20), 1902-1910.
 37. Paul, S. A., Boudenne, A., Ibos, L., Candau, Y., Joseph, K., & Thomas, S. (2008). Effect of fiber loading and chemical treatments on thermophysical properties of banana fiber/polypropylene commingled composite materials. *Composites Part A: Applied Science and Manufacturing*, 39(9), 1582-1588.
 38. Cordruwisch, J. (2014). Effects of mixing parameters on material properties of a carbon-fiber polyamide composite produced with the LFT-D-ILC process. (Master dissertation, Karlsruhe Institute of Technology).
 39. Fisa, B. (1985). Mechanical degradation of glass fibers during compounding with polypropylene. *Polymer composites*, 6(4), 232-241.

40. Czarnecki, L., & White, J. L. (1980). Shear flow rheological properties, fiber damage, and mastication characteristics of aramid-, glass-, and cellulose-fiber-reinforced polystyrene melts. *Journal of Applied Polymer Science*, 25(6), 1217-1244.
41. Shimizu, Y., Arai, S., Itoyama, T., & Kawamoto, H. (1997). Experimental analysis of the kneading disk region in a co-rotating twin screw extruder: Part 2. glass-fiber degradation during compounding. *Advances in Polymer Technology*, 16(1), 25-32.
42. He, B., Liu, H., Leng, J., Yang, B., Chen, X., Fu, J., & Fu, Q. (2011). Mechanical properties of long glass fiber-reinforced polypropylene composites and their influence factors. *Journal of Reinforced Plastics and Composites*, 30(3), 222-228.
43. Rohan, K., McDonough, T. J., Ugresic, V., Potyra, E., & Henning, F. (2015, June). Mechanical Study of Direct Long Fiber Thermoplastic Carbon/Polyamide 6 and its Relations to Processing Parameters. In *Proc. 14th-Annual SPE Automotive Composites Conference & Exhibition*.
44. Huembert, S. (2016). Influence of the screw configuration on the LFT-D processing of glass fiber reinforced PA6. (Master dissertation, Karlsruhe Institute of Technology).
45. Yilmazer, U., & Cansever, M. (2002). Effects of processing conditions on the fiber length distribution and mechanical properties of glass fiber reinforced nylon-6. *Polymer composites*, 23(1), 61-71.
46. Priebe, M., & Schledjewski, R. (2011). Processing and properties of glass/polypropylene in long fibre compounding extrusion. *Plastics, Rubber and Composites*, 40(6-7), 374-379.
47. Inoue, A., Morita, K., Tanaka, T., Arao, Y., & Sawada, Y. (2015). Effect of screw design on fiber breakage and dispersion in injection-molded long glass-fiber-reinforced polypropylene. *Journal of Composite Materials*, 49(1), 75-84.
48. Teixeira, D., Giovanela, M., Gonella, L. B., & Crespo, J. S. (2015). Influence of injection molding on the flexural strength and surface quality of long glass fiber-reinforced polyamide 6.6 composites. *Materials & Design*, 85, 695-706.
49. Bouwhuis, B. A., Tang, S. K., & Hibbard, G. D. (2008). Process–microstructure–property relationships in AA3003 expanded metal periodic cellular truss cores. *Composites Part A: Applied Science and Manufacturing*, 39(9), 1556-1564.
50. Folgar, F., & Tucker III, C. L. (1984). Orientation behavior of fibers in concentrated suspensions. *Journal of reinforced plastics and composites*, 3(2), 98-119.
51. Phelps, J. H., & Tucker, C. L. (2009). An anisotropic rotary diffusion model for fiber orientation in short-and long-fiber thermoplastics. *Journal of Non-Newtonian Fluid Mechanics*, 156(3), 165-176.

52. Nghiep Nguyen, B. A., Bapanapalli, S. K., Kunc, V., Phelps, J. H., & Tucker III, C. L. (2009). Prediction of the Elastic—Plastic Stress/Strain Response for Injection-Molded Long-Fiber Thermoplastics. *Journal of composite materials*, 43(3), 217-246.
53. Baran, I., Cinar, K., Ersoy, N., Akkerman, R., & Hattel, J. H. (2016). A review on the mechanical modeling of composite manufacturing processes. *Archives of computational methods in engineering*, 1-31.
54. Thomasset, J., Carreau, P. J., Sanschagrin, B., & Ausias, G. (2005). Rheological properties of long glass fiber filled polypropylene. *Journal of non-newtonian fluid mechanics*, 125(1), 25-34.
55. Shetty, M. R. (2001). Design and study of an extrusion-compression processing method capable of molding long-glass-fiber-reinforced polypropylene. (Master dissertation, University of Massachusetts Lowell).
56. Buck, F., Brylka, B., Müller, V., Mueller, T., Weidenmann, K. A., Hrymak, A. N., Henning, F. & Böhlke, T. (2015). Two-scale structural mechanical modeling of long fiber reinforced thermoplastics. *Composites Science and Technology*, 117, 159-167.
57. Hopmann, C., Weber, M., van Haag, J., & Schöngart, M. (2015, May). A validation of the fibre orientation and fibre length attrition prediction for long fibre-reinforced thermoplastics. In S. C. Jana (Ed.), *AIP Conference Proceedings* (Vol. 1664, No. 1, p. 050008). AIP Publishing.
58. Jeffery, G. B. (1922, November). The motion of ellipsoidal particles immersed in a viscous fluid. In *Proceedings of the Royal Society of London A: Mathematical, Physical and Engineering Sciences* (Vol. 102, No. 715, pp. 161-179). The Royal Society.
59. Stade, K. (1977). Techniques for compounding glass fiber-reinforced thermoplastics. *Polymer Engineering & Science*, 17(1), 50-57.
60. Weitsman, Y. (1991). Moisture in composites: sorption and damage. *Fatigue of composite materials*, 385-429.
61. Liao, K., Schultheisz, C. R., Hunston, D. L., & Brinson, L. C. (1998). Long-term durability of fiber-reinforced polymer-matrix composite materials for infrastructure applications: a review. *Journal of advanced materials*, 30(4), 3-40.
62. Karbhari, V. M., Kaiser, H., Navada, R., Ghosh, K., & Lee, L. (2005). *Methods for detecting defects in composite rehabilitated concrete structures* (No. FHWA-OR-RD-05-09).
63. Karbhari, V. M., Engineer, M., & ECKEL II, D. A. (1997). On the durability of composite rehabilitation schemes for concrete: use of a peel test. *Journal of Materials Science*, 32(1), 147-156.
64. Schutte, C. L. (1994). Environmental durability of glass-fiber composites. *Materials Science and Engineering: R: Reports*, 13(7), 265-323.

65. Marom, G. A. D., & Broutman, L. J. (1981). Moisture penetration into composites under external stress. *Polymer Composites*, 2(3), 132-136.
66. Jones, F. R. (1999). Durability of reinforced plastics in liquid environments. *Reinforced Plastics Durability*, 70-110.
67. Belarbi, A., Myers, J. J., Chandarshekhara, K., Watkins, S. E., & Bae, S. W. (2004). *Structural integrity of RC columns wrapped with FRP sheet subjected to various environmental conditions including corrosion* (No. RDT 04-021).
68. Xian, G., Wang, C., & Li, H. (2010, March). In-situ monitoring of curing and ageing effects in FRP plates using embedded FBG sensors. In *SPIE Smart Structures and Materials+ Nondestructive Evaluation and Health Monitoring* (pp. 764909-764909). International Society for Optics and Photonics.
69. Karbhari, V. M., & Engineer, M. (1996). Effect of environmental exposure on the external strengthening of concrete with composites-short term bond durability. *Journal of reinforced plastics and composites*, 15(12), 1194-1216.
70. Anstice, P. D., & Beaumont, P. W. R. (1982). Hygrothermal ageing of fibrous composites. *Progress in Science and Engineering of Composites*, 2, 1001-1008.
71. Weitsman, Y. J. (1995). *Effects of Fluids on Polymeric Composites-A Review* (No. MAES-95-1.0). TENNESSEE UNIV KNOXVILLE DEPT OF MECHANICAL AND AEROSPACE ENGINEERING.
72. Beg, M. D. H., & Pickering, K. L. (2008). Reprocessing of wood fibre reinforced polypropylene composites. Part II: Hygrothermal ageing and its effects. *Composites Part A: Applied science and manufacturing*, 39(9), 1565-1571.
73. Valentin, D., Paray, F., & Guetta, B. (1987). The hygrothermal behaviour of glass fibre reinforced PA66 composites: a study of the effect of water absorption on their mechanical properties. *Journal of materials science*, 22(1), 46-56.
74. Robert, M., & Benmokrane, B. (2009). Behavior of GFRP reinforcing bars subjected to extreme temperatures. *Journal of Composites for Construction*, 14(4), 353-360.
75. Ray, B. C. (2006). Effects of changing environment and loading speed on mechanical behavior of FRP composites. *Journal of reinforced plastics and composites*, 25(12), 1227-1240.
76. Xue, Y., Veazie, D. R., Glinsey, C., Horstemeyer, M. F., & Rowell, R. M. (2007). Environmental effects on the mechanical and thermomechanical properties of aspen fiber-polypropylene composites. *Composites Part B: Engineering*, 38(2), 152-158.
77. Sethi, S., & Ray, B. C. (2015). Environmental effects on fibre reinforced polymeric composites: Evolving reasons and remarks on interfacial strength and stability. *Advances in colloid and interface science*, 217, 43-67.

78. Thomason, J. L., & Yang, L. (2011). Temperature dependence of the interfacial shear strength in glass–fibre polypropylene composites. *Composites Science and Technology*, *71*(13), 1600-1605.
79. Kim, M. G., Kang, S. G., Kim, C. G., & Kong, C. W. (2007). Tensile response of graphite/epoxy composites at low temperatures. *Composite structures*, *79*(1), 84-89.
80. Elanchezhian, C., Ramnath, B. V., & Hemalatha, J. (2014). Mechanical behaviour of glass and carbon fibre reinforced composites at varying strain rates and temperatures. *Procedia Materials Science*, *6*, 1405-1418.
81. Correia, J. R., Gomes, M. M., Pires, J. M., & Branco, F. A. (2013). Mechanical behaviour of pultruded glass fibre reinforced polymer composites at elevated temperature: experiments and model assessment. *Composite Structures*, *98*, 303-313.
82. Bai, Y., Keller, T., & Vallée, T. (2008). Modeling of stiffness of FRP composites under elevated and high temperatures. *Composites Science and Technology*, *68*(15), 3099-3106.
83. Gibson, A. G., Torres, M. O., Browne, T. N. A., Feih, S., & Mouritz, A. P. (2010). High temperature and fire behaviour of continuous glass fibre/polypropylene laminates. *Composites Part A: Applied Science and Manufacturing*, *41*(9), 1219-1231.
84. Whitley, K. S., & Gates, T. S. (2002). Thermal/Mechanical response and damage growth in polymeric composites at cryogenic temperatures.
85. Wang, Q. (2012). Mechanical properties of long carbon fiber reinforced thermoplastic (LFT) at elevated temperature. (Master dissertation, The University of Alabama at Birmingham).
86. Lampman, S. (2003). *Characterization and failure analysis of plastics*. ASM International.
87. Reis, J. M. L., Coelho, J. L. V., Monteiro, A. H., & da Costa Mattos, H. S. (2012). Tensile behavior of glass/epoxy laminates at varying strain rates and temperatures. *Composites Part B: Engineering*, *43*(4), 2041-2046.
88. Mivehchi, H., & Varvani-Farahani, A. (2010). The effect of temperature on fatigue strength and cumulative fatigue damage of FRP composites. *Procedia Engineering*, *2*(1), 2011-2020.
89. Prabhakaran, R. D., & Toftegaard, H. (2014). Environmental effect on the mechanical properties of commingled-yarn-based carbon fibre/polyamide 6 composites. *Journal of composite materials*, *48*(21), 2551-2565.
90. Shen, C. H., & Springer, G. S. (1977). Effects of moisture and temperature on the tensile strength of composite materials. *Journal of Composite Materials*, *11*(1), 2-16.

91. Halpin, J. C. (1969). *Effects of Environmental Factors on Composite Materials* (No. AFML-TR-67-423). AIR FORCE MATERIALS LAB WRIGHT-PATTERSON AFB OH.
92. Thomason, J. L. (2010). Dependence of interfacial strength on the anisotropic fiber properties of jute reinforced composites. *Polymer Composites*, 31(9), 1525-1534.
93. Thomason, J. L. (2002). Interfacial strength in thermoplastic composites-At last an industry friendly measurement method?. *Composites Part A: Applied Science and Manufacturing*, 33(10), 1283-1288.
94. Wagner, H. D., & Nairn, J. A. (1997). Residual thermal stresses in three concentric transversely isotropic cylinders: application to thermoplastic-matrix composites containing a transcrystalline interphase. *Composites Science and Technology*, 57(9-10), 1289-1302.
95. Nairn, J. A. (1985). Thermoelastic analysis of residual stresses in unidirectional, high-performance composites. *Polymer Composites*, 6(2), 123-130.
96. Raghava, R. S. (1988). Thermal expansion of organic and inorganic matrix composites: A review of theoretical and experimental studies. *Polymer Composites*, 9(1), 1-11.
97. Di Landro, L., & Pegoraro, M. (1996). Evaluation of residual stresses and adhesion in polymer composites. *Composites Part A: Applied Science and Manufacturing*, 27(9), 847-853.
98. RÜEGG, A., STÖTZNER, N., JAGGI, D., & ZIEGLER, S. (2004). A new mass production process for lightweight structural parts and their application-field. In *ANTEC... conference proceedings* (Vol. 3, pp. 3504-3508). Society of Plastics Engineers.
99. Strait, L. H., Karasek, M. L., & Amateau, M. F. (1992). Effects of stacking sequence on the impact resistance of carbon fiber reinforced thermoplastic toughened epoxy laminates. *Journal of Composite Materials*, 26(12), 1725-1740.
100. Grauer, D., Hangs, B., Reif, M., Martsman, A., & Jespersen, S. T. (2012). Improving Mechanical Performance of Automotive Underbody Shield with Unidirectional Tapes in Compression-Molded Direct-Long Fiber Thermoplastics(D-LFT). *Sampe Journal*, 48(3), 7-15.
101. Emerson, D., Grauer, D., Hangs, B., Reif, M., Henning, F., Martsman, A., ... & Jespersen, S. T. (2012). Using unidirectional glass tapes to improve impact performance of thermoplastic composites in automotive applications. *Proceedings SPE ACCE*, 12, 11-13.
102. Hangs, B., Esch, C., Reif, M., Huber, T., & Henning, F. (2011). Integration of Features into Parts Made from Thermoplastic, Unidirectional Tape—Overview and Case Study. *SPE ACCE*.

103. Lutz, V. Improving processability and mechanical performance with the use of unidirectional thermoplastic tapes in compression molding for automotive structural applications.
104. Fang, X., Shen, C., & Dai, G. (2016). Mechanical properties of unidirectional continuous fiber tapes reinforced long fiber thermoplastics and their manufacturing. *Journal of Reinforced Plastics and Composites*, 35(5), 408-420.
105. Brümmer, M., Henning, F., & Krause, W. (2005). Long-Fiber Reinforced Thermoplastics Tailored for Structural Performance. *SPE ACCE*.
106. Thattai parthasarathy, K. B., Pillay, S., Bansal, D., Ning, H., & Vaidya, U. K. (2013). Processing and Characterization of Continuous Fibre Tapes Co-Moulded With Long Fibre Reinforced Thermoplastics. *Polymers & Polymer Composites*, 21(8), 483.
107. Thattai parthasarathy, K. B., Vaidya, U. K., & Pillay, S. Damage tolerance enhancement using continuous fiber reinforcements co-molded with long fiber reinforced thermoplastics.
108. Rion, J., Leterrier, Y., & Månson, J. A. E. (2008). Prediction of the adhesive fillet size for skin to honeycomb core bonding in ultra-light sandwich structures. *Composites Part A: Applied Science and Manufacturing*, 39(9), 1547-1555.
109. Voigt, W. (1889). Ueber die Beziehung zwischen den beiden Elasticitätsconstanten isotroper Körper. *Annalen der Physik*, 274(12), 573-587.
110. Reuss, A. (1929). Berechnung der fließgrenze von mischkristallen auf grund der plastizitätsbedingung für einkristalle. *ZAMM-Journal of Applied Mathematics and Mechanics/Zeitschrift für Angewandte Mathematik und Mechanik*, 9(1), 49-58.
111. Affdl, J. C., & Kardos, J. L. (1976). The Halpin-Tsai equations: a review. *Polymer Engineering & Science*, 16(5), 344-352.
112. Chamis, C. C. (1989). Mechanics of composite materials: past, present, and future. *Journal of Composites, Technology and Research*, 11(1), 3-14.
113. ROSEN, B. W. (1964). ZVI HASHIN2.
114. Mori, T., & Tanaka, K. (1973). Average stress in matrix and average elastic energy of materials with misfitting inclusions. *Acta metallurgica*, 21(5), 571-574.
115. Huang, Z. M. (2001). Micromechanical prediction of ultimate strength of transversely isotropic fibrous composites. *International journal of solids and structures*, 38(22), 4147-4172.
116. Huang, Z. M. (2001). Simulation of the mechanical properties of fibrous composites by the bridging micromechanics model. *Composites Part A: applied science and manufacturing*, 32(2), 143-172.
117. Cox, H. L. (1952). The elasticity and strength of paper and other fibrous materials. *British journal of applied physics*, 3(3), 72.
118. Reinforcement, H. K. F. (1964). Akademisk Forlag. *Copenhagen, Denmark*.

119. Fu, S. Y., & Lauke, B. (1998). The elastic modulus of misaligned short-fiber-reinforced polymers. *Composites science and technology*, 58(3-4), 389-400.
120. Fu, S. Y., & Lauke, B. (1996). Effects of fiber length and fiber orientation distributions on the tensile strength of short-fiber-reinforced polymers. *Composites Science and Technology*, 56(10), 1179-1190.
121. ASTM International. (2014). ASTM D638-14 Standard Test Method for Tensile Properties of Plastics. Retrieved from <https://doi.org/10.1520/D0638-14>.
122. ASTM International. (2015). ASTM D790-15e2 Standard Test Methods for Flexural Properties of Unreinforced and Reinforced Plastics and Electrical Insulating Materials. Retrieved from <https://doi.org/10.1520/D0790-15E02>.
123. ASTM International. (2012). ASTM D5379/D5379M-12 Standard Test Method for Shear Properties of Composite Materials by the V-Notched Beam Method. Retrieved from https://doi.org/10.1520/D5379_D5379M-12.
124. ISO, E. (2000). 6603-2: 2000, "Determination of puncture impact behaviour of rigid plastics", *ISO Norm*.

Curriculum Vitae

Name: Yuchao Liu

**Post-secondary
Education and
Degrees:** China University of Mining and Technology
Xuzhou, Jiangsu, China
2006-2010 B.E.

General Research Institute for Nonferrous Metal
Beijing, China
2011-2014 M.E.Sc.

**Related Work
Experience** Internship
Fraunhofer Project Center for Composite Research
2015

Summer school
Karlsruhe Institute of Technology
2016

Publications:

Fan, Y., Liu, Y. C., Whitfield, T., Kuboki, T., Wood, J. T., & Ugresic, V. EFFECTS OF PROCESSING PARAMETERS ON THE THERMAL AND MECHANICAL PROPERTIES OF LFT-D-ECM GLASS FIBER/POLYAMIDE 6 COMPOSITES.

Yuchao, L., Fan, Y. Wood, J. T. Adjusting the mechanical properties of PA6 based D-LFT composites with UD tapes. (in preparation)